Quantum many-body dynamics of ultra-cold gases in cavity mediated optical potentials

Dissertation
zur Erlangung des akademischen Grades
Doctor of Philosophy

von

Elvia Colella

eingereicht an der
Fakultät für Mathematik, Informatik und Physik
der Leopold-Franzens-Universität Innsbruck

Betreuung der Dissertation:
Univ.-Prof. Dr. Helmut Ritsch,
Institut für Theoretische Physik,
Universität Innsbruck

Innsbruck, 29 November 2021

universität innsbruck

Phd Thesis

Quantum many-body dynamics of ultra-cold gases in cavity mediated optical potentials

Elvia Colella
Supervisor: Univ.-Prof. Dr. Helmut Ritsch
Co-Supervisor: Farokh Mivehvar, PhD

29 November 2021

Zusammenfassung

Experimente in der Atom-, Molekül- und optischen Physik nutzen die kontrollierte Licht-Teilchen-Wechselwirkung, um den inneren und den Bewegungszustand der Teilchen zu kontrollieren und zu manipulieren. Die Streuung von Photonen an Teilchen induziert dissipative und reaktive Kräfte, die die Schwerpunkts Bewegung der Atome effizient kühlen und die Teilchen in optischen Potentialen, die durch die elektromagnetischen Lichtfelder erzeugt werden, einfangen. Schließt man Licht und Teilchen in einem optischen Resonator ein, wird das von den Lichtfeldern erzeugte optische Potential nichtlinear an die Dichteverteilung des Gases gekoppelt. Für ausreichend starke Laserbeleuchtung induziert die kollektive Streuung des Lichts durch die Teilchen oft einen Phasenübergang in einen Zustand mit kristalliner Ordnung. Diese Anordnung maximiert das in die Kavität gestreute Licht. In solchen Anordnungen induzieren Photonen über Mehrfachstreuung an verschiedenen Teilchen Korrelationen und weit reichende Zweikörperwechselwirkungen, was wiederum die Entstehung selbstorganisierter Strukturen begünstigt.

Diese Arbeit leistet einen zentralen Beitrag zu einer erweiterten Klasse von Modellsystemen, die sich auf die dynamische Selbstordnung von ultrakalten Gasen aus mehreren Komponenten in optischen Resonatoren konzentrieren. Während sich frühe Versuchsaufbauten und viele theoretische Modelle auf bosonische und Spin polarisierte Quantengase beschränken, werden wir uns in dieser Arbeit mit Effekten beschäftigen, die aus der Kopplung zwischen den inneren und äußeren atomaren Freiheitsgraden durch die Wechselwirkungen mit Hohlraumphotonen resultieren.

Zuerst untersuchen wir die Selbstorganisation der Spin Freiheitsgrade in fermionischen Spinorgasen in optischen Ringresonatoren. In Analogie zu Spin polarisierten Fermi-Gasen treibt die Erhöhung der Pumpstärke über einen kritischen Schwellenwert das System in einen superradianten Zustand. Dadurch brechen antiferromagnetische Spin- und Dichtewellen spontan die kontinuierliche Translationssymmetrie des Hamilton-Operators, die eng mit der Resonator Geometrie verbunden ist. Die Rolle der Quantenstatistik in diesem System wird durch das Verhalten der Zweikörper-Impulskorrelationsfunktionen enthüllt. Im Konkreten induziert das Pauli-Prinzip eine unvermeidliche Antikorrelation der Impulse zwischen Atomen im gleichen Zustand. Die Photonen im Resonatorfeld induzieren mittels Ramanübergängen dann Korrelationen zwischen den äußeren und den inneren atomaren Freiheitsgraden. In Summe sind dann verschiedene Teilchen mit gleichen Spin- und Impulszuständen maximal antikorreliert, während positive Korrelationen zwischen Atomen mit entgegengesetzten Spins auftreten. Solche Korrelationen übertragen sich durch den Impulsübertrag bei der Streuung eines Photons dann zu höheren Impulsen.

In einem weiteren Kapitel zeigen wir dann, wie bestehende Schemata zur Simulation künstlicher Eichtheorien erweitert und verbessert werden können, indem die dynamis-

che Kopplung zwischen Atomen und Hohlraumlichtfeldern genutzt wird. Letztendlich werden die zugehörigen Eichfelder dadurch vollständig dynamisch. Der erste Schritt in diese Richtung besteht in der Realisierung des Hohlraum-vermitteltem Nächsten-Nachbar-Tunnelns durch gezielte Resonanz-Zweiphotonen-Raman-Übergänge zwischen verschiedenen Plätzen eines extern vorgeschriebenen Gitters. Dazu betrachten wir ein zweidimensionales spinloses Fermi-Gas, das von zwei unabhängigen transversalen Laserstrahlen gepumpt wird und mit einer Einzelmode eines linearen Resonators wechselwirkt. Die räumliche Verteilung des Pumplaserlichts prägt der atomaren Wellenfunktion hier eine Aharonov-Bohm-Phase auf. Somit simuliert das System die physikalischen Eigenschaften von Elektronen in einem periodischen Potential und einem externen Magnetfeld. Dies reproduziert die Quanten-Hall-Physik. Die dynamische Kopplung zwischen den fermionischen Atomen und den Hohlraumphotonen unterscheidet dieses System von seinem Festkörper-Gegenstück und Realisierungen mit statischen optischen Gittern und Laserfeldern. Das Eichfeld entsteht hier spontan nur in der superradianten Phase. Dies induziert eine Verzerrung des Energiespektrums, die von der nichtlinearen Kopplung zwischen der Amplitude des Hohlraumlichtfeldes und der kinetischen Energie des atomaren Gases herrührt.

Die Realisierung der vollen Dynamik eines effektiven Eichfeldes erfordert hier eine weitere Erhöhung der Komplexität des betrachteten Systems. Das Isolieren einer Seite des zweidimensionalen Gitters und mittels Implementation von Spin aufgelösten gerichteten Tunneln lässt sich damit ein vollständig dynamisches Eichpotential realisieren. Zwei unterschiedliche Hohlraummoden, die an jeweils einen eigenen Hyperfeinzustand ankoppeln vermitteln dadurch das atomare Tunneln in entgegengesetzte Richtungen. Die Phase der Hohlraummoden wird der Wellenfunktion wie eine dynamische Arahonov-Bohm-Phase eingeprägt, die dabei intrinsisch an den atomaren Zustand koppelt. Diese Kopplung induziert indirekt eine Dichte- und Stromabhängigkeit des entstehenden Eichfelds, da die Dichte des atomaren Gases auf die Hohlraumresonanz zurückwirkt. Mittels dispersiver Kopplung sich mit der Dichte die Frequenz jeder Mode proportional der Besetzung im entsprechenden Hyperfeinzustand. Im stationären Bereich korreliert die Entstehung eines solchen Eichfeldes mit der dynamischen Stabilisierung persistenter Teilchenströme. Hingegen führen periodische zeitabhängige Ströme zu Eichpotentialen die einem zeitabhängigen synthetischen magnetischen Fluss entsprechen. Dies induziert wiederum eine elektromotorische Kraft in Analogie zum Faraday'schen Induktionsgesetz.

Abstract

Experiments in atom, molecular and optical physics routinely exploit light-matter interaction to control and manipulate the state of the particles. Scattering events with photons induce dissipative and reactive forces that efficiently cool the center of mass motion of the atoms, and trap the particles into the potential landscape created by the electromagnetic light fields. By placing the particles to an optical resonator, the trapping potential generated by the light fields is non-linearly coupled to the density distribution of the gas. The collective scattering of the emitters induces a phase transition to a state with crystalline order for sufficient strong pumping, thus maximizing the light scattered into the cavity. In such set-ups photons indirectly induce correlations and long-range two-body interactions, favouring the emergence of self-organized structures.

This Thesis aims to contribute to a new class of studies that focus on the dynamical self-ordering of multi-component ultra-cold gases coupled to light fields in optical resonators. While early experimental set-ups and theoretical models restricted themselves to bosonic and spin-polarized quantum gases, in this Thesis we will deal with effects arising from the coupling between the internal and external atomic degrees of freedom induced by the interactions with cavity photons.

First, we investigate spin self-organization phenomena in spinor fermionic gases coupled to ring resonators. In analogy to spin-polarized Fermi gases, increasing the pump strength above a critical threshold drives the system into a superradiant state. Alongside, antiferromagnetic spin and density waves spontaneously break the continuous translational symmetry of the Hamiltonian that is intimately related to the cavity geometry. In this system the role of quantum statistics is exposed by the two-body momentum correlations. In fact the Pauli principle induces an inevitable anticorrelation among atoms in the same state. Cavity photons correlate the external and the internal atomic degrees of freedom through the Raman scattering from the pump to the cavity. As a result, particles occupying the same spin and momentum states are maximally anticorrelated, while positive correlations arise among atoms with opposite spins. Such correlations are then propagated at higher momenta when an atom experiences a momentum kick by scattering a photon.

Next, we show how to improve existing schemes for simulating artificial gauge theories by taking advantage of the dynamical coupling between atoms and cavity light fields. Ultimately, this will render the gauge field completely dynamic. The first step in this direction consists of realizing cavity-mediated nearest-neighboured tunneling by tuning to resonance two-photon Raman transitions between different sites of an externally prescribed lattice. To this extent, we will consider a two-dimensional spinless Fermi gas pumped by two independent transversal laser beams and interacting with a single-mode

of a linear cavity. The profile of the pumping lasers imprints an Aharonov-Bohm phase on the atomic wavefunction. Hence, the system simulates the physics of electrons in a periodic potential and an external magnetic field, reproducing the quantum Hall physics. The dynamical coupling between the fermionic atoms and the cavity photons distinguishes this system from its solid-state counterpart and realizations with static optical lattices and laser fields. The gauge field spontaneously arises in the superradiant phase leading to a distortion of the energy spectrum, which stems from the non-linear coupling between the cavity-mode amplitude and the kinetic energy of the atomic gas.

The realization of a fully dynamical gauge field requires increasing a step further the system complexity. Isolating one leg of the two-dimensional lattice and implementing spin-resolved directional tunnelings, realizes a completely dynamical gauge potential. Two distinct cavity modes, addressing their own hyperfine state, mediate the atomic tunneling in opposite directions. The phase of the cavity modes is imprinted on the wave function like a dynamic Arahonov-Bohm phase that intrinsically couples to the atomic state. This coupling indirectly induces a density dependence in the emerging gauge field as the atomic gas density acts back on the cavity resonance by shifting the frequency of each mode according to the occupation in each hyperfine state. In the stationary regime, the emergence of such a gauge field stems from the stabilization of persistent particle currents. Periodic time-dependent gauge potentials result in a time-dependent synthetic magnetic flux and induce an electromotive force in analogy to Faraday's law of induction.

Acknowledgments

This Thesis would not have found its completion without a few people that with their help and support have accompanied me in this journey.

First of all I would like to thank my supervisor Helmut Ritsch for giving me the opportunity to work in his group. I've never found a person with more enthusiasm and passion for physics, physical insight and compassion.

Next, I am grateful to Farokh Mivehvar for all the knowledge that he shared with me, for the valuable advice in times of struggle, and for being a friend.

I would like to thank all the collaborators of the past years, Stefan Ostermann, Wolfgang Niedenzu, Francesco Piazza and Arkadiusz Kosior, and all the group members, Anna Bychek, Julian Cremer, Martin Fasser, Raphael Holzinger, Daniela Holzmann, Christoph Hotter, Laurin Ostermann, David Plankensteiner, B. Prasanna Venkatesh, Verena Scheil, Matthias Sonnleitner, Elias Starchl and Valentin Torggler. Special thanks go to Natalia Masalaeva that spread liveliness and positivity in the office, to Maria Moreno-Cardoner for her kindness and amiability, and to Arkadiusy Kosior for the vivid and enlightening discussions about physics and about life. Thanks to Jean-Philippe Brantut and his group for the warm welcome in Lausanne, as I could not have have spent a better time and felt more welcome.

Finally, I am grateful to all the people that indirectly contributed by brightening my days during the past five years. Thanks to Cosetta, Claudia, Deborah, Elisa, Gabriele, Lorenzo and Silvia. Thanks to LLuis for the adventures we went through together and the many more to come.

Contents

1 Introduction

In the midst of the first quantum revolution in the early 20th century, "the coldest place on Earth" was located in Leiden in the physics laboratory of Onnes. Experiments reaching temperatures of a few Kelvins lead to the liquefaction of Helium in 1908 [1.1]. Later-on the measurement of a vanishing electrical conductivity in a solid Mercury wire set the discovery of superconductivity in 1911 [1.2]. Meanwhile Einstein complemented the pioneering work of Bose and introduced to the world the phenomenon of Bose-Einstein Condensation in 1925 [1.3]. A year later, in 1926, Fermi [1.4] and Dirac [1.5] independently derived the statistical distribution of identical particles obeying to the Pauli exclusion principle, henceforth named as fermions. In 1933, the lambda point of the superfluid transition in Helium was observed for the first time [1.6]. Following the experiments of Kapitza in 1938 [1.7], London proposed that the superfluid nature of liquid Helium could be traced back into the phenomenon of Bose-Einstein Condensation (BEC) [1.8]. The relationship between the two phenomena remained rather elusive, since the estimated critical temperature for Bose-Einstein Condensation $T_c \sim$ mK at standard densities was well below the temperature at which superfluidity was observed in Helium. In addition Bose-Einstein Condensation was predicted for an ideal non-interacting gas, while Helium was a strongly correlated liquid. Nonetheless, it was apparent that the behavior of matter at low temperatures exhibited extraordinary new features. These phenomena are a manifestation of the quantum nature of matter which becomes manifest, when indistinguishability effects between identical particles require all atomic degrees of freedom to be treated quantum mechanically.

For a quantum gas to be degenerate, the thermal de Broglie wavelength must larger than the inter-particle spacing and the range of the inter-atomic interactions. It is not surprising that it was only after the newfound awareness that atoms can stay in the gaseous phase even at very low temperatures [1.9], that an intense experimental activity starting with hydrogen and progressing to alkali atoms lead to the observation of degeneracy in dilute quantum gases. The diluteness of the gas was a crucial to prevent three body losses and ensure low energy two-body scattering processes. The quest to quantum degeneracy required an intense technological progress with the further development of suitable cooling and trapping techniques, which ultimately lead to the first experimental realization of a Bose-Einstein Condensate in 1995 for Rubidium atoms [1.10, 1.11]. Shortly after, in 1999, a Fermi gas of Potassium-40 was cooled toward degeneracy [1.12].

Since the groundbreaking experiments in Fermi and Bose gases, atom optics developed as an interesting and fertile environment for engineering and quantum simulating systems of very different nature [1.13–1.15]. The idea of simulating one system by using another was first brought forward by Feynman in his 1982 lecture [1.16]. Solving quantum models which are computationally too challenging for a classical computer requires to build

a quantum device able to simulate its physics. The success of quantum simulating platforms came with an increasing technological progress that allowed to fully control the atomic state. The realization of Feshbach resonances [1.17, 1.18] allowed to control the strength of the interatomic interaction and set the beginning of an era, where typical models from many-body theory could be experimentally tested. Remarkable examples are the realization of the Mott insulator phase [1.19], which constitutes one of the first experimental realization of the Bose-Hubbard model, or the exploration of the BCS-BEC crossover [1.20, 1.21], which confirmed the fermionic superfluidity in cold atoms [1.22]. The realization of optical lattices enabled to generate perfect crystals of light serving as flawless periodic potentials for atoms [1.23]. With these achievements atom optics established itself as a perfect platform for quantum simulation effectively realizing Feynman's proposal.

1.1 Ultra-cold atoms in cavity QED

The incredible achievement of atom optics has been driven by the astonishing accuracy and precision in the manipulation of the atomic properties at the single atom level. In this perspective, light-matter interaction proved to be one of the most powerful tools for the modification and control of the atomic quantum states [1.24]. Quantum simulation set-ups extensively use laser light in a variety of applications ranging from the generation of optical lattices and trapping potentials to state manipulation and cooling. When the externally prescribed laser fields are replaced by the dynamical electric field of a quantized mode in an optical resonator, interaction effects are strongly enhanced due to the augmented scattering probability between an atom and a photons [1.25]. In a cavity the interaction between light and matter becomes dynamical. That is, the back-action of the radiation emitted by atom on itself needs to be taken into account [1.26]. As a result, the atomic motion becomes dynamically coupled to the electromagnetic field radiated into the cavity and intricate new non-linear effects arise [1.27].

Fascinating collective effects can be observed, when an ensemble of N atoms collectively interacts with a single mode of an optical resonator, showing e.g. Dicke superradiance [1.28]. The first realization of such a model goes back to the ETH experiment in 2010 [1.29–1.31], in which one observed the self-organization of the atomic gas density in a one component transversally driven BEC coupled to the vacuum mode of a single mode linear cavity. Above a critical pump strength, the system undergoes a phase transition from an homogeneous superfluid to a periodic modulated density. At the onset of the phase transition atoms occupy odd or even sites of the self-generated optical potential such that the emitted radiation pattern constructively interferes and the field scattered into the cavity is maximized. In analogy to one component BEC systems, it was shown that a spinless Fermi gas in a linear cavity self-organizes in a periodic lattice in the superradiant state [1.32]. The most striking difference with the bosonic case is the predicted suppression of the critical self-organization threshold at half-filling for a one-dimensonal system [1.33, 1.34]. In fact, the commensurability between the Fermi momentum k_F and the momentum acquired by an atom through the scattering with

a cavity photon k_c, induces resonant processes such that a fermion can jump from one side of the Fermi surface to the other without any energy cost, a phenomenon known as Peierls instability [1.35].

1.2 New Perspectives in Many-body cQED

The realization of superradiant self-organization of a bosonic quantum gas set a milestone after which quantum gas based cavity QED saw a rapid growth of experimental realizations and theoretical studies with an increasing level of complexity. Using different cavity geometries allowed to explore the concept of symmetry breaking and its consequences in a more general fashion. A remarkable example is the observation of a superfluid-supersolid phase transition for a BEC loaded in a crossed cavity setup [1.36]. This experiment is one of the first demonstrations of supersolidity in Nature, and was quickly followed by the direct experimental observation of Higgs and Goldstone excitation modes [1.37].

While the continuous symmetry, which leads to the appearance of such Goldstone mode in this experiment is only approximate [1.38], it was later shown that ring cavities exhibit a perfect U(1) symmetry enabling the stabilization of a real supersolid [1.39]. Shortly after supersolidity was observed for a BEC loaded in a ring cavity [1.40].

In this already rich framework, a novel and interesting direction is constituted by the study of spinor quantum gases in optical cavities. The introduction of additional internal degrees of freedom of the particles makes these hybrid systems even more appealing for the study of magnetic phases and spin dynamics. Ground-breaking experiments at ETH [1.41] and Stanford University [1.42] designed spin-dependent cavity coupling and realized superradiant magnetic phases. In the ETH experiment a tranversally pumped single mode linear cavity was dispersively coupled to the $F = 1$ manifold of a Rb^{87} BEC. The experiment makes use of the vectorial component of the atomic polarizability tensor, which distinctly couples the different magnetic sublevels m_F. Therefore spin-dependent coupling can be realized, giving rise to a phase with non vanishing magnetizaton and uniform density. By contrast, the Stanford experiment focuses on the realization of spin-dependent coupling using a multi-level structure of a BEC of Rb^{87} transversally pumped, as proposed in Ref. [1.43]. This experiment constitutes the first realization of dynamical spin-orbit coupling in a cavity [1.44, 1.45]: superradiance sets in above a critical pump strength after the self-organization of the atoms in a crystalline structure and spin waves appear. By means of spin resolved time of flight images, the experiment reconstructed the momentum distribution of the two spin states. Above threshold a significant population of the other spin state was observed, demonstrating that cavity photons indeed mediates spin-dependent interactions.

As a result of such long-range interaction, a novel class of theoretical studies proposed that superconducting phases can be stabilized via spin-dependent cavity-mediated interaction in fermionic quantum gases addressed via cavity-mediated Raman transitions [1.46–1.49]. These questions posed by recent theoretical work remain so far unanswered, as only in the last couple of years cavity QED experiments were able to work with fermionic isotopes. As a result, only recently fermionic superradiance was

experimentally observed in Ref. [1.50]. Alongside pioneering experiments at EPFL have opened a completely new direction, demonstrating the existence of strong two-body correlation arising into a Lithium 6 gas coupled to a far detuned molecular state though a cavity-mediated photon-association transition [1.51–1.53].

1.3 Outline of the Thesis

This Thesis extends the theoretical modeling of the physics of ultra-cold gases in optical cavities beyond the state of the art of *many-body cavity QED*. Recent studies have introduced a plethora of new cavity configurations which make use of multi-component quantum gases and different cavity geometries for manipulating the dynamical symmetries of the Hamiltonian. As a result fundamental differences in the behaviour of the system arise and a variety of intriguing many-body phenomena can be investigated. In particular this Thesis deals with two major research questions: the study of superradiance and quantum phase transitions in spinor Fermi gases dispersively coupled to light fields in an optical resonator, and the search of alternative cavity-based platforms for the realization of artificial dynamical gauge fields.

Chapters 2-4 of this Thesis contain the necessary theoretical background and literature review which will allow to understand more complex self-organization phenomena in cavity QED. Chapters 5-7 feature novel results which are collected in two publications and one pre-print.

In Chapter 2 we include some preliminary concepts and the theoretical tools that constitute the foundation of the publications included in this Thesis. The emblematic features of light-matter interaction in a cavity will be introduced, along with the concept of superradiance and self-ordering phase transition for a dispersively coupled quantum gas. We will then dig with more accuracy into two specific applications.

In Chapter 3 we will briefly sketch the physics of multi-component gases coupled to optical resonators and cavity-induced spin-spin interactions.

In Chapter 4 we will introduce the general set-up for generating artificial gauge field for neutral atoms. We will then highlight the advantages of cavity-mediated schemes, and the possibility to render the synthetic gauge fields fully dynamical.

In the publication in Chapter 6 we will explore the density and spin self-ordering of a spinor Fermi gases coupled to a transversally pumped two-mode mode ring cavity. Above a critical pump strength, the atomic gas self-organizes in an antiferromagnetic pattern with spontaneously emerging density and spin waves. Cavity photons mediate strong cooperative effects between the atomic motion and the internal atomic dynamics. Accordingly, we study correlations in momentum space for atoms in the same and opposite spin state. Such correlations can be traced back to the propagation of the Pauli principle to higher momenta through the interaction with the cavity modes.

In Chapter 6 we will study the properties of a spin polarized Fermi gas transversally coupled to a single mode linear cavity on a lattice. The set-up is based on a scheme proposed in Ref. [1.54], which constitute the first proposal of cavity-mediated synthetic magnetic fields. The artificial gauge field spontaneously emerges in the superradiant

regime, when a macroscopic electromagnetic field builds inside the cavity. In this publication we investigated the phase diagram, and carried an extensive study of the fractal energy spectrum of the system, i.e., dynamical Hofstadter butterfly.

In Chapter 7 we investigate the generation of density-dependent dynamical gauge fields due to the coupling of a degenerate gas to two longitudinal modes of a multi-mode cavity. The density dependence stems from the non linear shift of the cavity resonance induced by the presence of the atoms in the cavity and requires strong light-matter interaction. We investigate the self-consistent magnetic flux which spontaneously arise in the steady state of the coupled system: he finite Aranov-Bohm flux piercing the ladder plaquette lead to stabilization of atomic persistent currents. We will finally deal with the periodic dynamical time evolution of the emerging gauge fields, which allows to simulate Faraday induction's law.

Concluding remarks are given in Chapter 8.

2 Self-organization and Superradiance in CQED

This Chapter introduces the essential concepts upon which this Thesis is founded and presents the methods adopted throughout it. Starting from the physics of light in classical electrodynamics, we will look at how dielectrics affect the light in a medium. Next we will introduce superradiance as a collective classical effect appearing in atomic ensembles coupled to optical resonators and see how this concept appears in the theoretical description of quantum phase transitions. Finally we show that the microscopic properties of the system can be encoded in the atomic susceptibility, presenting a generalized theory of light-matter interaction with a field integral theory approach.

2.1 Introduction

Understanding light-matter interaction has always been a problem of significant fundamental interest in physics. Even before Maxwell formulated a comprehensive theory of electromagnetism [2.1], mechanical effects of light were envisioned as the source of the deflection of comets tails. It took almost a hundred years to observe in a laboratory that electromagnetic waves carry momentum and thus exert forces on macroscopic objects in the form of radiation pressure [2.2]. With the advent of the XX century, the discovery of the atom and the formulation of quantum mechanics brought a new interpretation to these physical phenomena. Soon after the deflection due to radiation pressure was finally observed for atoms, by shining a lamp perpendicular onto a sodium beam and thereby deflect it [2.3].

In the second half of the XX century the discover of the laser [2.4] and the development of progressively more sophisticated spectroscopy techniques enabled the measurement of atomic energy levels with high precision. It was apparent that not only does light act on a mechanical level, but that it also affects the atomic internal structure by shifting and broadening its energy levels. Light-exerted dissipative and reactive forces are used today to manipulate the atomic state. Atoms are cooled to temperatures of the order of the nanokelvin, and forces arising from spatial light shift gradient generate traps, mirrors, and optical lattices.

Just as light is a source of perturbation for the atoms, so is the atomic medium for the electromagnetic field. An atom interacting with nearly resonant monochromatic light can often be effectively described by a two-level system. The electromagnetic field couples to the selected transition through the atomic dipole moment. In the low intensity regime, the atom stays in the ground state, and electrons are bound to the attractive potential

generated by the nuclei. The quantum picture then coincides with a semi-classical description of the atom as a driven oscillating dipole that modifies the electromagnetic field around it via three fundamental processes: emission, absorption, and dispersion. As a result, atoms perturb the electromagnetic field by attenuating its intensity and affecting the propagation speed of light in the medium. In Section 2.2 we will see that these effects can be connected to a single parameter, the electronic susceptibility of the medium.

Although the atomic medium modifies the propagation of light, the field changes are not strong enough to substantially act back on the atoms in free space. Specifically, the cross-section of the photon scattering process limits the probability that a scattered photon interacts again with the same or a closeby atom [2.5]. It is an intriguing question, whether the light-matter coupling can become strong enough for the back-action of the radiation emitted by the dipole on itself to induce substantial effects. In Section 2.3 we will show that placing a polarizable particle in a cavity can significantly enhance the interaction between light and matter, i.e. atoms and photons. Despite the atoms being linearly polarizable, the enhanced coupling of the atom-photon dynamics in a cavity generates a nonlinear field response.

In a cavity, the collective increase of the atom-light interaction for large atomic ensembles ultimately leads to superradiance, i.e. light scattering proportional to the atom number squared. When mechanical effects of light, i.e. photon momentum, are taken into account, the electromagnetic field couples to the center of mass motion of the atoms. As a result, superradiance derives from the self-organization of the atomic density into a self-consistent optical potential generated from the constructive interference of the field radiated by each atomic emitter [2.6]. In Section 2.4 we will interpret this process as a second order phase transition with the self-organized atomic density playing the role of an order parameter. We will show that the transition point is uniquely determined by the atomic susceptibility, and we will retrace the same topics introduced at the beginning of this Chapter from a completely new perspective.

2.2 Light-matter interaction in dielectric materials

Different materials react differently in response to applied electromagnetic fields. While conductors develop currents due to the numerous free charges in the medium, insulating materials cannot conduct electricity because their electrons are tightly bound to the nuclei. Such materials, also know as dielectrics, are still affected by electromagnetic fields, and develop a polarization in response to an applied electric field. Specifically, each dielectric material is composed of many small dipoles, and a dipole moment is induced by the external driving field. The following section describes the origin of the polarization in dielectric materials, and how different media affect the light propagation properties in the medium.

2.2.1 Polarizible media

To understand the origin of the dielectric polarization, it is necessary to look at how a dipole moment can develop in a medium [2.7]. Some molecules like water vapor feature an asymmetric charge distribution and thus posses a permanent electric dipole moment, which aligns directly along the applied electromagnetic field. For neutral atoms the charge distribution is symmetric, and the origin of the dipole moment is less obvious as it needs a relative shift of the electrons with respect to the nucleus.

An atom constitutes of a positively charged core and a surrounding electronic density. An applied electric field will stretch the charge distribution pushing the electrons and the nuclei in opposite directions. The displacement of the center of the negative charge distribution from the core behaves like a dipole. For an incoming wave the dipole oscillates at the same frequency of the incident electric field, absorbing power from it and scattering it into other free space modes, see Figure 2.1. If a charge q has been displaced by $\delta\mathbf{r}$, the dipole moment per atom is defined as $\mathbf{p} = q\delta\mathbf{r}$. For N atoms per unit volume, the total dipole moment per unit volume defines the polarization vector of the medium $\mathbf{P} = Nq\delta\mathbf{r}$.

If the applied electric field $\mathbf{E}$ is weak, we can approximate the displacement as being linear in the electric field. The polarization vector then reads as

$$\mathbf{P} = \epsilon_0 \chi_e \mathbf{E}, \tag{2.1}$$

with ϵ_0 the permittivity in vacuum. The electric susceptibility χ_e is a parameter that varies from material to material, and describes how the medium reacts in response to the applied electric field.

A simple way to understand the origin of the susceptibility is by considering a spring model of the atom (Lorentz oscillator) [2.7]. One can think that the electron is held by a spring to the nuclei, oscillating at a natural frequency ω_0 and emitting radiation at a rate γ. The parameter γ encloses dissipative effects and represents the spontaneous emission coefficient of the excited state appearing in a quantum picture. An external electric field applies an additional force onto the oscillator so that the equation of motion for the displacement reduces to a simple driven-damped harmonic oscillator,

$$m(\delta\ddot{\mathbf{r}} + \gamma\delta\dot{\mathbf{r}} + \omega_0^2\delta\mathbf{r}) = q\mathbf{E}, \tag{2.2}$$

with $\delta\mathbf{r}$ the displacement parallel to $\mathbf{E}$. Assuming that the electric field $\mathbf{E}$ oscillates at a single frequency ω, we can solve for $\delta\mathbf{r}$,

$$\delta\mathbf{r} = \frac{q/m}{\omega_0^2 - \omega^2 + i\gamma\omega}\mathbf{E}. \tag{2.3}$$

The induced dipole moment of the atom is

$$\mathbf{p} = \alpha(\omega)\mathbf{E}, \tag{2.4}$$

and

$$\alpha(\omega) = \frac{q^2/m}{\omega_0^2 - \omega^2 + i\gamma\omega} \tag{2.5}$$

is the atomic polarizability. The atomic polarizability is complex, and its real and imaginary part take the simple form of a dispersive and absorptive lineshape, as shown in the inset of Figure 2.1. The first determines the phase shift experienced by the electric field, as the dipole behaves as a refractive medium. The latter quantifies the power absorbed by the dipole from the drive and determines the attenuation of the electric field. Knowing the atomic polarizability, the susceptibility of the gas can be easily derived as $\chi_e(\omega) = \alpha(\omega)/\epsilon_0$.

Usually, dielectric media are much more complex than the Lorentz model described above. Even for the simplest case of a dilute atomic gas, many atomic transitions couple to the light fields resulting in different resonance frequencies contributing to the total polarizability. Such resonances are located in the optical domain as they depend on the energy spacing between different electronic transitions. It is even more difficult for dense ensembles, where each atom is surrounded by a bubble of other dipoles very close to each other. In dense ensembles, the modification of the local electromagnetic field acting on the central dipole and self-consistent effects acting on the macroscopic electric field cannot be neglected. In the course of this Thesis, we will deal only with ultra-cold dilute gases. The concept of atomic susceptibility will be recurrent along this Thesis. By the end of this Chapter we will extend these concepts and look at the response of a quantum gas with either fermionic or bosonic statistics. Ultimately, we will show that when the electromagnetic field couples to the mechanical atomic degrees of freedom, the polarizability will acquire a new set of resonances due to the mechanical coupling of light with the motional atomic degrees of freedom.

2.2.2 Propagation of light in a dielectric medium

Let us now discuss how the propagation properties of light are affected by the presence of the dielectric medium. By combining the Maxwell equations,

$$\nabla \cdot \mathbf{E} = -\frac{\nabla \cdot \mathbf{P}}{\epsilon_0}, \qquad c^2 \nabla \times \mathbf{B} = \frac{\partial}{\partial t}\left(\mathbf{E} + \frac{\mathbf{P}}{\epsilon_0}\right), \tag{2.6}$$

$$\nabla \times \mathbf{E} = -\frac{\partial \mathbf{B}}{\partial t}, \qquad \nabla \cdot \mathbf{B} = 0, \tag{2.7}$$

we can derive a wave equation for the propagation of the electric field, $\mathbf{E}$, which only depends on the polarization $\mathbf{P}$,

$$\nabla^2 \mathbf{E} - \frac{1}{c^2}\frac{\partial^2 \mathbf{E}}{\partial t^2} = -\frac{1}{\epsilon_0}\nabla(\nabla \cdot \mathbf{P}) + \frac{1}{\epsilon_0 c^2}\frac{\partial^2 \mathbf{P}}{\partial t^2}. \tag{2.8}$$

Assuming that the dielectric is isotropic and that the polarization vector is pointing in the same direction as the electric field, we can look for wave-like solution of the equation above. Considering am incoming wave propagating in the $\hat{\mathbf{e}}_z$ direction and linearly polarized along the $\hat{\mathbf{e}}_x$ direction, $\mathbf{E} = \hat{\mathbf{e}}_x E_0 e^{i(kz+\omega t)}$, results into the Helmholtz equation

$$\left(-k^2 + \frac{\omega^2}{c^2}\right) E_0 = -\frac{\omega^2}{\epsilon_0 c^2} P_0 \tag{2.9}$$

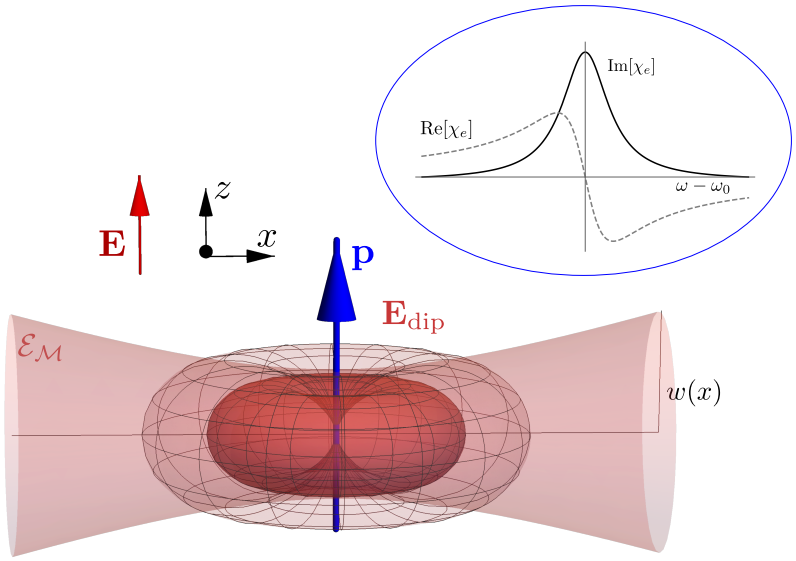

Figure 2.1: A polarizable particle in free space develops an induced dipole moment, $\mathbf{p} = \frac{1}{2}p\hat{\mathbf{e}}_z e^{i\omega t} + c.c.$, (here schematized as a blue arrow). The atom is driven by a transverally incident electric field $\mathbf{E} = \frac{1}{2}\hat{\mathbf{e}}_z e^{-i\omega t} + c.c$ lineraly polarized in the $\hat{\mathbf{e}}_z$ direction. The dipole oscillates at the same frequency ω of the driving electric field $\mathbf{E}$. The radiation absorbed by the dipole is emitted all directions, $\mathbf{E}_{\text{dip}}$, and can be collected into a Gaussian mode of interest $\mathcal{M}$ of the free electromagnetic spectrum propagating in a direction perpendicular to the incident field $\mathbf{E}$, and with waist $w(x = 0) = w_0$. The mode amplitude is $\mathcal{E}_{\mathcal{M}}$. The strength of light-matter interaction in free space is set by the ratio between the power emitted into the full solid and the power collected into the mode $\mathcal{M}$. This ratio defines the single atom cooperativity in free space $\mathcal{C}_{fs} = 2P_{\mathcal{M}}/P_{4\pi}$. Inset: The response of the atom is embedded in the atomic susceptibility χ_e, which in the rotating wave approximation, $\omega - \omega_0 \ll \omega_0$, acquires a Lorentzian absorption (solid black line) and dispersion profile (dashed gray line).

for a uniform polarization, that is $\nabla \cdot \mathbf{P} = 0$. For a linearly polarizable media, $\mathbf{P} = \epsilon_0 \chi_e \mathbf{E}$, we can finally derive the wave vector k at which the wave needs to propagate for the electromagnetic wave to be solution of Equation 2.9,

$$k^2 = \frac{\omega^2}{c^2}\left(1 + \chi_e\right). \tag{2.10}$$

The result above shows that the phase velocity of the wave

$$v = \frac{\omega}{k} = \frac{c}{\sqrt{1+\chi_e}} = \frac{c}{n}, \tag{2.11}$$

is reduced compared to the propagation velocity in vacuum by the refractive index of the medium,

$$n^2 = 1 + \chi_e. \tag{2.12}$$

The refractive index intrinsically depends on the susceptibility of the medium, and thus on the polarizability. Upon decomposing it in his imaginary and real part $n = n' + in''$, the solution for the wave equation reads as

$$\mathbf{E} = \hat{\mathbf{e}}_x E_0 e^{i\omega(t+\frac{nz}{c})} = \hat{\mathbf{e}}_x E_0 e^{-\frac{n''z}{c}} e^{i\omega(t+\frac{n'z}{c})}. \tag{2.13}$$

The electromagnetic wave amplitude is exponentially decreasing along the propagation direction $E_0 e^{-\frac{n''z}{c}}$ and travelling at a speed n'/c. The imaginary part of the index of refraction determines the attenuation of the electric field due to the absorption of the medium, and the real part of the index of refraction determines the dispersive effects which modify the propagation speed in the dielectric.

2.3 Cooperative phenomena in atomic ensembles

In the previous section we have seen that an atom driven by an electric field behaves like a dynamic dipole, absorbing power from the driving electric field and scattering it over the full solid angle. The strength of the atom-photon coupling in this process is determined by the single particle cooperativity

$$C_{fs} = 6/(k^2 w^2). \tag{2.14}$$

The cooperativity C_{fs} regulates all aspects of light-matter interaction [2.25], from the absorption and the dispersive phase shift induced by the atoms on the light, to the fraction of the field power scattered into a single Gaussian mode of the free electromagnetic spectrum. In free space, the cooperativity is set by the ratio of the cross-section of a resonant photon-atom scattering process, $\sigma_0 = 6\pi/k^2$, and the scattered beam area, $A = \pi w^2/2$. Typically the scattered mode only subtends a small fraction of the full solid angle, so that the beam waist, w, is much larger than the wavelength, $\lambda = 2\pi/k$. As a result, the cooperativity in free space is upper bounded, $C_{fs} \ll 1$, and light-matter interaction is typically too weak to induce non-linear effects in the atom-photon

dynamics. This raises the question, whether is it possible to coherently enhance light-matter interaction, so that the back-action of the radiation emitted by the dipole acts back on the dipole itself. While coupling radiation to an ensemble of N atoms enhances the cooperativity by a factor NC_{fs}, it does not fundamentally change the scattering cross-section per atom. In the following section we will see how the coupling of polarizible particles to the electromagnetic fields in an optical resonator can provide a coherent enhancement of the light-matter interaction.

2.3.1 Optical resonators

An optical resonator consists of two or more highly reflective mirrors, which are arranged such that the propagating light is forced to come back to its origin. As photons go back and forth between the mirrors, the power of the cavity electromagnetic field is largely amplified. However, the light inside the resonator can only freely propagate at few specific wave-vectors, k_m, that are commensurate with the cavity length,

$$\omega_m = ck_m = 2\pi\frac{c}{\lambda_m} = 2\pi m\frac{c}{2L}. \tag{2.15}$$

Here, L is the length of the resonator, $2L$ is the round trip distance and m is a natural integer. Only a discrete number of equally-spaced modes can be amplified in a cavity. The separation distance between the frequency, ω_m, of two consecutive longitudinal modes set the free spectral range of the cavity, $\delta\omega_{\mathrm{FSR}}/2\pi = c/2L$. Depending on the resonator geometry and on the curvature of the mirrors, each longitudinal mode is accompanied by a family of transversal modes in the form of Laugerre-Gaussian or Hermite-Gaussian modes [2.8]. Despite taking into account the transversal profile can be of interest [2.9], in the following of this Thesis we will restrict atomic ensembles coupled to a single, or a pair, of longitudinal TEM_{00} Gaussian modes.

The inherent losses that arise from the diffraction and imperfections of the mirrors are another fundamental characteristic of the physics of light fields propagating in optical resonators. For a Fabry-Perot resonator, which consists of two parallel mirrors placed at distance L from each other, the quality of the cavity is embedded in the finesse,

$$\mathcal{F} = \frac{\pi\sqrt{\mathcal{R}}}{1-\mathcal{R}^2}, \tag{2.16}$$

and is a feature of the cavity which only depends on the reflectivity of the mirrors $\mathcal{R}$. Here, we define $\mathcal{R}$ and $i\mathcal{T}$ as the reflection and transmission coefficient of the mirrors with, $\mathcal{R}^2 + \mathcal{T}^2 = 1$. The finesse set the lifetime of the electromagnetic field inside cavity, and determines the cavity decay rate coefficient,

$$\kappa = \frac{\delta\omega_{FSR}}{2\mathcal{F}} \sim \mathcal{T}^2\frac{c}{L}, \tag{2.17}$$

for a highly reflective cavity $\mathcal{T}^2 \ll 1$.

2.3.2 Light-matter interaction in a cavity

A polarizible particle in an optical resonator

Let us now consider a polarizable particle positioned at an antinode of a cavity mode of frequency ω_c. An electric field $\mathcal{E}_{in}$ drives the atom and propagates in the direction perpendicular to the cavity axis, as shown in Figure 2.2. The fraction of the field emitted by the atom, which is scattered into the cavity can be expressed by projecting the radiated field over the small angle subtended by the cavity [2.25],

$$\mathcal{E}_{\mathcal{M}} = i\beta\mathcal{E} = i\frac{k}{\pi w^2}\frac{\alpha}{\epsilon_0}\mathcal{E}. \tag{2.18}$$

Here, α is the atomic polarizability introduced in the previous section, w is the waist of the cavity mode, and k is the wave-vector of electromagnetic field propagating into the cavity. In contrast to the scattering in free space, where the atom would only feel the effects of the incident field $\mathcal{E}_{in}$, the field $\mathcal{E}$ driving the dipole includes both the incident and cavity field,

$$\mathcal{E} = \mathcal{E}_{in} + \mathcal{E}_c. \tag{2.19}$$

The confinement of the electromagnetic radiation by the cavity mirrors increases the scattering probability of the photons in a mode with the atom. The particle scatters photons into the cavity, and the resonator amplifies the electromagnetic field so that it becomes strong enough to self-consistently drive the atom. The stationary condition for the field inside the resonator then reads as

$$\mathcal{E}_c = 2\mathcal{E}_{\mathcal{M}} + \mathcal{R}^2 e^{2ikL}\mathcal{E}_c. \tag{2.20}$$

The first term of the Equation (2.20) represents the field scattered by the atom into the forward and backward direction, $\mathcal{E}_{\mathcal{M}}$. The second term represents the propagated cavity field after one trip and takes into account two consecutive reflections at the mirrors and the phase acquired during propagation, e^{2ikL}. For highly reflective mirrors $\mathcal{R} \gg \mathcal{T}$, the phase factor can approximated as $\mathcal{R}^2 e^{2ikL} = 1 - \mathcal{T}^2 + 2i\mathcal{T}^2\Delta_c/\kappa$, with $\kappa = \mathcal{T}^2 c/L$ the cavity decay rate.

By writing the scattered field in terms of the driving field $\mathcal{E}$, we can derive the stationary electric field in the cavity:

$$\mathcal{E}_c = i\beta\frac{2\mathcal{E}_{in}}{t^2}\frac{1}{1 - 2i\frac{\Delta_c}{\kappa} - \frac{4i\beta}{t^2}}. \tag{2.21}$$

The intensity emitted into the cavity is equal to the intensity transmitted through one of the mirrors, $I_c = c\epsilon_0/2\mathcal{T}^2|\mathcal{E}_c|^2$, and the intensity emitted in free space in absence of the cavity is given by $I_{4\pi} = c\epsilon_0/2|\mathcal{E}_{in}|^2/C_{fs}$. The ratio between the two quantities

$$\frac{I_c}{I_{4\pi}} = \frac{C}{\left(1 + \frac{\mathrm{Im}(4\beta)}{t^2}\right)^2 + \left(\frac{\Delta_c}{\kappa} - \frac{\mathrm{Re}(4\beta)}{t^2}\right)^2} \tag{2.22}$$

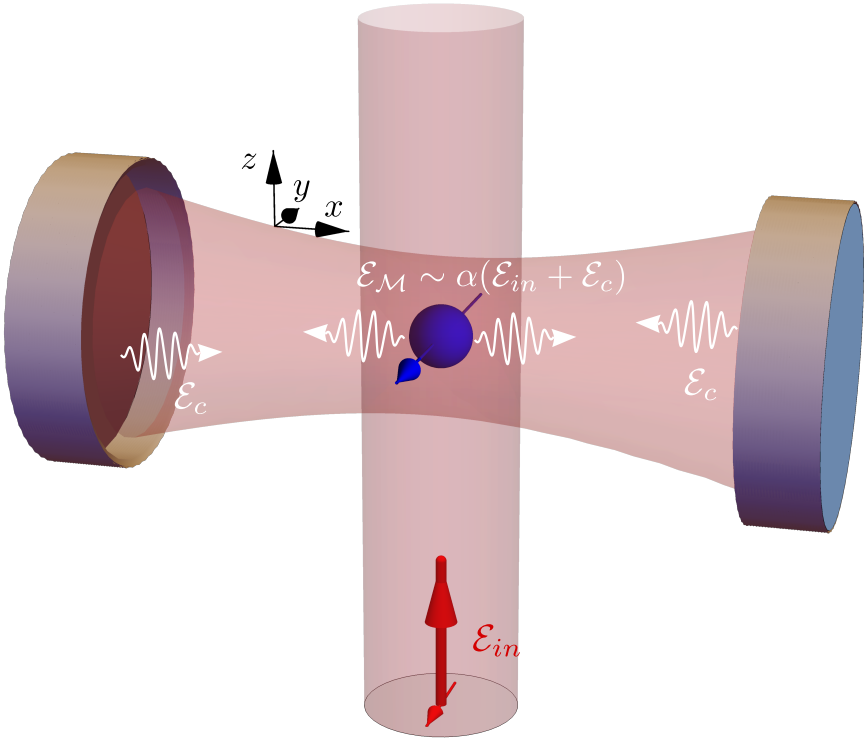

Figure 2.2: A single polarizible particle (in blue) is placed at an antinode of a single mode in a linear cavity. The atom is driven by the the cavity electromagnetic field $\mathcal{E}_c$ and an incident field $\mathcal{E}_{in}$, linearly polarized along the $\hat{\mathbf{e}}_y$ direction. The projection of the electromagnetic field emitted by atom into the cavity is $\mathcal{E}_{\mathcal{M}}$.

describes the enhancement of the scattering into the cavity compared to free space. The power emitted into free space is presence of the cavity is strongly enhanced (or suppressed) compared to free space by a factor proportional to a newfound cooperativity,

$$C = \frac{4C_{fs}}{\mathcal{T}^2} = \frac{4\mathcal{F}C_{fs}}{\pi}. \tag{2.23}$$

In comparison to free space the cavity cooperativity is enhanced by a factor proportional to the finesse of the cavity, $4/\mathcal{T}^2 = 4\mathcal{F}/\pi$. This enhancement arises from the constructive interference of the radiation emitted by the single dipole on different round trips of the light, before photons are lost from one of the mirrors. Interestingly, the enhancement of the light field can be seen as resulting from the constructive interference of an atom with itself at a later time.

Collective response in atomic ensembles

Let us now briefly comment on the behavior of N atoms identically coupled to a cavity mode in the same scattering configuration of Figure 2.2. The position occupied by the atoms along the cavity axis will affect the emission, however Equation (2.22) still applies upon substituting the single atom parameters, β and C, with the collective coefficients,

$$\beta_N = \beta \sum_{j=1}^{N} \cos^2(kx_j), \qquad \text{and} \qquad C_N = C \left| \sum_{j=1}^{N} e^{ikz_i} \cos(kx_j) \right|^2 , \tag{2.24}$$

here $\mathbf{r}_j$ is the position of the j particle in the cavity volume [2.25]. The form factor $\sum_j \cos^2(kx_j)$ determines the absorptive and dispersive properties of the atomic ensemble. The intensity of the light scattered into the cavity is collectively enhanced by a form factor $\sim \sum_{j=1}^{N} e^{ikz_i} \cos(kx_j)$, which measures the ordering of the atomic distribution with respect the wavelength $\lambda = 2\pi/k$ of the cavity mode. For a perfectly ordered ensemble all particles are kept λ apart and there is an overall $C_N = N^2 C$ enhancement of scattering compared to the single atom case. This effect arises in atomic ensembles due to the collective interference of the field scattered by each emitter: when the atoms are ordered in a perfect lattice they emit in phase with each other, maximizing the scattering into the mode $\mathcal{E}_{\mathcal{M}}$. The power emitted into the mode then scales as N^2 which set the superradiant properties of the scattering into the cavity. Superradiance hence arise as a phenomenon based on constructive interference of the radiation emitted by the individual atoms. If particles are allowed to move, light forces can act on the particles favoring the emergence of the optimal lattice structure in a self-organized manner. Then self-organization arise as a phase transition which sets by increasing the power of the incident laser as we will see in the next section.

2.4 Self-organization Phase Transition

The previous section showed that cooperative effects in atomic ensembles lead to the superradiant scattering into an optical resonator. In this context, superradiance and self-organization are interpreted as classical non-linear phenomena.

Nevertheless, there is an explicit connection between the build-up of a coherent classical electromagnetic field inside the cavity and the emergence of an atomic order parameter that measures the spatial ordering of the atomic cloud. Self-organization and superradiance provide yet another example of spontaneous symmetry breaking.

This section aims to bridge quantum optics and condensed matter physics. We will look at the superradiant scattering into the cavity within the framework of classical phase transitions, and introduce the numerical and analytical techniques adopted in the following Chapters. To this extent the simplest system of a transversally pumped atomic gas in a linear cavity will provide a pedagogical example to study superradiance and self-organization in ultra-cold atomic gases. We will then reconnect to classical electromagnetism and show that, independently of the microscopic details of our models,

each medium is ultimately a polarizable material whose interaction with light fields is completely determined by its susceptibility.

2.4.1 Ultra-cold atoms dispersively coupled to a single mode cavity

Consider an ensemble of ultra-cold two level atoms with internal states $\{|g\rangle, |e\rangle\}$ of energy $\omega_g = 0$ and $\omega_e = \omega_a$. An optical transverse pump of frequency ω_p and intensity Ω_p drives the atomic transition. The driving laser is back-reflected by a mirror placed on-axis with the laser along a direction $\hat{\mathbf{e}}_p$ with respect to the cavity axis. The atomic transition is also coupled to a cavity mode with frequency ω_c and coupling strength $g_0 = \wp\sqrt{\omega_a/2\hbar\epsilon_0\mathcal{V}}$, where $\wp$ is the dipole moment relative to the addressed atomic transition and $\mathcal{V}$ is the effective cavity mode volume.

Within the rotating wave approximation the system is described by the Hamiltonian

$$\begin{aligned}\hat{H}' = -\hbar\Delta_c\hat{a}^\dagger\hat{a} + \sum_{\sigma=g,e}\int d\mathbf{r}\hat{\psi}^\dagger_\sigma(\mathbf{r})\left[-\frac{\hbar^2\nabla^2_{\mathbf{r}}}{2m} + V_{\text{ext}}(\mathbf{r}) - \hbar\Delta_a\delta_{\sigma,e}\right]\hat{\psi}_\sigma(\mathbf{r}) \\ + \hbar\int d\mathbf{r}\Big\{\hat{\psi}^\dagger_e(\mathbf{r})\left[\Omega_p\cos(\mathbf{k}_p\cdot\mathbf{r}) + g_0\hat{a}\cos(\mathbf{k}_c\cdot\mathbf{r})\right]\hat{\psi}_g(\mathbf{r}) + \text{h.c.}\Big\} \qquad (2.25)\end{aligned}$$

Here, $\Delta_a = \omega_a - \omega_p$ and $\Delta_c = \omega_c - \omega_p$ are the atomic and cavity detuning in the frame rotating at the pump frequency ω_p, and $V_{\text{ext}}(\mathbf{r})$ is an harmonic trapping potential. The operator $\hat{\psi}_{g(e)}(\mathbf{r})$ destroys a particle in the ground (excited) state at position $\mathbf{r}$, and can either follow bosonic or fermionic commutation rules depending on the atomic species adopted. The bosonic operator $\hat{a}$ destroys a photon from the cavity field.

Following the discussion in the previous section, the atom-cavity system should be treated as an open system due to the photon losses through the mirrors. The evolution of the density matrix of the system can be then describes with a master equation approach

$$\dot{\hat{\rho}} = -\frac{i}{\hbar}[\hat{H}', \hat{\rho}] + \hat{\mathcal{L}}_c\hat{\rho}, \qquad (2.26)$$

with $\hat{\rho}$ denoting the density matrix of the full system and

$$\hat{\mathcal{L}}_c\hat{\rho} = -\kappa\left(\hat{a}^\dagger\hat{a}\hat{\rho} + \hat{\rho}\hat{a}^\dagger\hat{a} - 2\hat{a}\hat{\rho}\hat{a}^\dagger\right) \qquad (2.27)$$

being the Liouville operator which describes decay processes from the cavity at a rate 2κ.

In the dispersive regime when the atomic detuning Δ_a is the fastest time scale, the excited state is only virtually populated and its dynamics can be adiabatically eliminated. This gives rise to an effective Hamiltonian for the ground state and photons only,

$$H = -\hbar\Delta_c\hat{a}^\dagger\hat{a} + \int d\mathbf{r}\hat{\psi}^\dagger(\mathbf{r})\left[-\frac{\hbar^2\nabla^2_{\mathbf{r}}}{2m} + V_{\text{ext}}(\mathbf{r}) + V_{\text{opt}}(\mathbf{r})\right]\hat{\psi}(\mathbf{r}), \qquad (2.28)$$

where $\hat{\psi}(\mathbf{r}) \equiv \hat{\psi}_g(\mathbf{r})$ is the destruction operator for a particle in the ground state level at position $\mathbf{r}$. Note that the model is general at this point, and the shape of the Hamiltonian is independent on the specific quantum statistics of the particles.

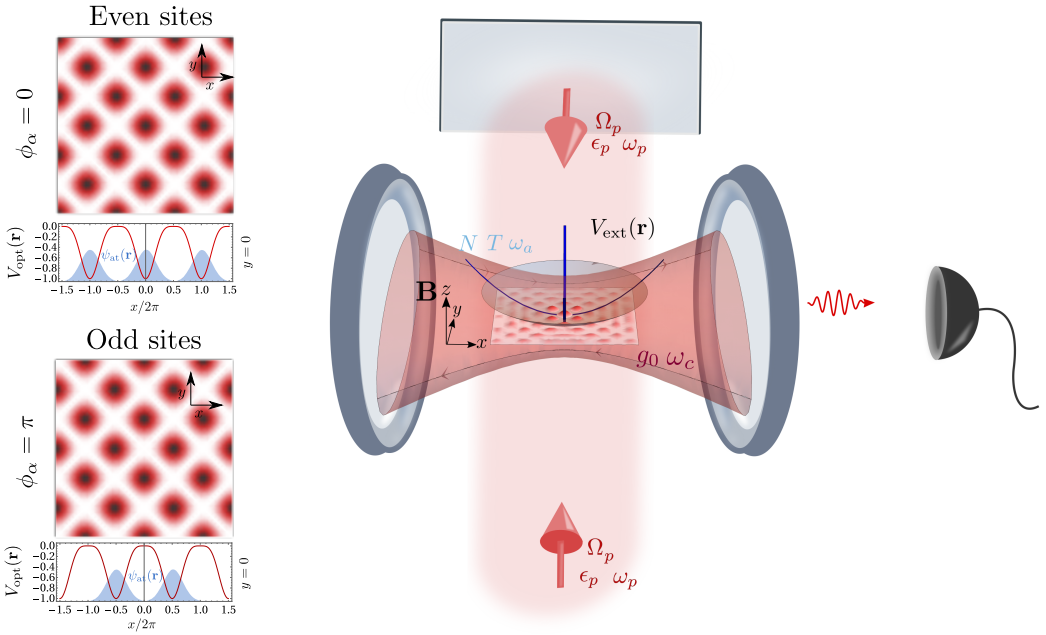

Figure 2.3: Typical experimental set-up for the observation of the self-organization phase transition in a quantum gas coupled to a single Gaussian mode of a linear optical resonator. An harmonic trap $V_{\rm ext}(\mathbf{r})$ confines the atomic gas into the cavity. A transversal back-reflected pump Ω_p polarized along the direction $\hat{e}_p$ drives an atomic transition $|g\rangle \leftrightarrow |e\rangle$. The effective optical potential generated by the dispersively coupled cavity field can be seen as a projection on the x-y plane on the left hand side. The $\mathbf{Z}_2$ symmetry breaking coincides in this case with the emergence of one of the two possible optical lattices which correspond to the phase locking of the intra-cavity field to the external pump laser, with a relative phase $\phi_a = 0$ or $\phi_\alpha = \pi$. The two check-board lattices correspond to a density configuration which is localized at even or odd sites of the emerging cavity potential.

In the dispersive regime the interaction between the electromagnetic fields and the atomic medium appears as an optical potential acting on the center of mass motion of the atoms,

$$V_{\rm opt}(\mathbf{r}) = \hbar\Omega_0 \cos^2(\mathbf{k_p}\cdot\mathbf{r}) + \hbar U_0 \cos^2(\mathbf{k}_c\cdot\mathbf{r})\,\hat{a}^\dagger\hat{a} + \hbar\eta_0(\hat{a}^\dagger+\hat{a})\cos(\mathbf{k}_p\cdot\mathbf{r})\cos(\mathbf{k}_c\cdot\mathbf{r})\,. \tag{2.29}$$

There are three main contributions to the optical potential $V_{\rm opt}(\mathbf{r})$. The first term, $\sim \hbar\Omega_0\cos^2(\mathbf{k_p}\cdot\mathbf{r})$ creates a $\lambda_p/2$ periodic optical lattice generated by the incident pump laser along the transversal direction. The depth of the optical lattice is set by the two-photon Rabi frequency, $\Omega_0 = \Omega_p^2/\Delta_a$. The second term, $\sim \hbar U_0\cos^2(\mathbf{k}_c\cdot\mathbf{r})\,\hat{a}^\dagger\hat{a}$, is a $\lambda_c/2$

periodic optical lattice generated along the cavity axis, $\hat{\mathbf{e}}_c$, through the consecutive photon absorption and emission into the cavity mode. The depth of this potential dynamically depends on the number of photons in the cavity, $U_0\langle\hat{a}^\dagger\hat{a}\rangle$, with $U_0 = g_0^2/\Delta_a$ being the single photon lattice depth. The third term, $\sim \hbar\eta_0(\hat{a}^\dagger + \hat{a})\cos(\mathbf{k}_p \cdot \mathbf{r})\cos(\mathbf{k}_c \cdot \mathbf{r})$ is an interference potential generated by scattering of photons from the pump to the cavity, and it is controlled by the two photon Rabi frequency, $\eta_0 = g_0\Omega_p/\Delta_a$. The interference lattice is confined in the plane intercepted by the cavity axis $\hat{\mathbf{e}}_c$ and the pump axis $\hat{\mathbf{e}}_p$. If the wave-vector of the pump, $\mathbf{k_p} = k\hat{\mathbf{e}}_y$, is perpendicular to the cavity wave-vector, $\mathbf{k_c} = k\hat{\mathbf{e}}_x$, the optical lattice is a $\lambda \sim 2\pi/k$ periodic check-board potential in the $x-y$ plane with primitive vectors $\mathbf{a} = \lambda(n\hat{\mathbf{e}}_+ + m\hat{\mathbf{e}}_-,)$, and $\hat{\mathbf{e}}_\pm = (\hat{\mathbf{e}}_x \pm \hat{\mathbf{e}}_y)/\sqrt{2}.$, as indicated in Figure 2.3.

While the pump lattice is a *static* periodic potential, whose depth is set by the power of the external pump laser $\propto \Omega_p$, the cavity generated potentials are *dynamical*. Namely, the amplitude of the cavity electromagnetic field $\langle\hat{a}\rangle$ intrinsically depends on the spatial structure of the atomic cloud. When the cavity field is strong, atoms localize at the minima of the potential, and the cloud develops a density modulation. The emerging crystalline structure maximizes the scattering into the cavity and triggers a runaway process. The more atoms self-organize in the dynamical optical potential the more photons are scattered into the cavity, thus strengthening the cavity-generated potential and the atomic crystalline structure.

Perhaps one of the most intriguing aspects of the atomic self-organization in such dynamical potentials is that the emerging density pattern breaks the symmetries of the Hamiltonian. The potential $V_{\rm opt}(\mathbf{r}) = V_{\rm opt}(\mathbf{r}+\mathbf{a})$ possesses an intrinsic discrete translational symmetry due to its periodic nature, which can be coupled to the gauge freedom for the phase rotation of the photonic operator, $\hat{a} \to \hat{a}e^{i\phi}$, to form a global $\mathbb{Z}_2$ symmetry. In particular, the $\mathbb{Z}_2$ transformation which leaves the Hamiltonian invariant is a translational symmetry $x \to x + \lambda/2$ combined with a π phase rotation of the photonic operators $\hat{a} \to -\hat{a}$. This transformation corresponds to two distinct optical lattices shifted in the $\hat{\mathbf{e}}_x$ direction by $\lambda/2$, and to two distinct density configurations with particles occupying either even or odd sites of a checkboard optical lattice. The two states are energetically degenerate, and the collapse of the system to one of them is an example of spontaneous symmetry breaking in an open driven-dissipative system.

2.4.2 Mean-field

A common method for studying self-organization phenomena in a cavity is based on a mean-field approximation of the atom-photon system. In essence, quantum effects due to atom-photon correlations that result into non-classical states of light are disregarded. Instead, the light fields inside the resonator are treated as classical coherent states, $\langle\hat{a}\rangle \equiv \alpha$. In the adiabatic limit for the photon dynamics, $\Delta_c, \kappa \gg \max[g_0, U_0]$, photons evolve on a much faster timescale with respect to atoms and instantaneously adapt to the atomic configuration by reaching a steady state.

The steady state value of the intra-cavity field amplitude, $\alpha = \langle\hat{a}\rangle$, is then derived by

averaging the Heisenberg equation of motion for the photon destruction operator,

$$i\hbar\frac{\partial\alpha}{\partial t} = -\hbar\left(\Delta_c - U_0\mathcal{N}_{2k_c} + i\kappa\right)\alpha + \hbar\eta_0\Theta = 0, \tag{2.30}$$

and is directly determined by the atomic mean-field averages, Θ and $\mathcal{N}_{2k_c}$. Here we have defined $\mathcal{N}_{2k_c} = \int d\mathbf{r}\cos^2(\mathbf{k_c}\cdot\mathbf{r})n(\mathbf{r})$ and $\Theta = \int d\mathbf{r}\cos(\mathbf{k_c}\cdot\mathbf{r})\cos(\mathbf{k_p}\cdot\mathbf{r})n(\mathbf{r})$ as the integral overlap between the atomic density $n(\mathbf{r}) = \langle\hat{\psi}^\dagger(\mathbf{r})\hat{\psi}(\mathbf{r})\rangle$ and the cavity generated optical potentials. The atomic average, Θ, measures the self-ordering of the atomic state in the interference lattice, $\propto\cos(\mathbf{k_c}\cdot\mathbf{r})\cos(\mathbf{k_p}\cdot\mathbf{r})$, and acts as a source term for the light fields inside the cavity. When the cavity is empty, $\alpha = 0$, the density is uniform and $\Theta = 0$. By increasing the tranversal probe intensity, η_0, more photons are scattered into the cavity, atoms accumulate at the minima of a stronger interference potential, and the density develops a structural modulation. In this regime the cavity field develops a coherent amplitude α and the average Θ is non-vanishing. The atomic average Θ then acts as an order parameter for a phase transition from a dark to a superradiant state.

In this context, the atomic average of an observable $\hat{O}$ is defined as an expectation value over the atomic ground state, $O = \langle\mathrm{GS}|\hat{O}|\mathrm{GS}\rangle$. The ground state however intrinsically depends on the stationary electromagnetic field inside the cavity, α. In order to fully solve the problem, the ground state must be determined with an iterative self-consistent procedure.

The single particle Hamiltonian H_α can be diagonalized for a given value of the intra-cavity amplitude α, and the ground state can be written as a tensor product of single particle wave-functions with eigenenergies ϵ_i^α,

$$\hat{\Psi}^\alpha_{\mathrm{GS}}(\mathbf{r}) = \Pi_i\phi_i^\alpha(\mathbf{r})\hat{c}_i^\alpha. \tag{2.31}$$

Here $\hat{c}_i^\alpha$ is the destruction operator in an eigenstate of the Hamiltonian with energy ϵ_i, following either bosonic or fermionic statistics. The generic creation operator can be expanded in terms of the eigenstates of the Hamiltonian

$$\hat{\psi}(\mathbf{r}) = \sum_i \phi_i^\alpha(\mathbf{r})\hat{c}_i^\alpha, \tag{2.32}$$

and density can be written as

$$n(\mathbf{r}) = \sum_i |\phi_i^\alpha(\mathbf{r})|^2 n_{FD(B)}(\epsilon_i^\alpha), \tag{2.33}$$

and

$$n_{FD(B)}(\epsilon_i^\alpha) = \frac{1}{e^{(\epsilon_i^\alpha-\mu)/k_bT}\pm 1} \tag{2.34}$$

is either the Fermi-Dirac or Bose statistics depending on the atomic species adopted. Note that at this point the statistical nature particles must be specified. Beneath this requirement lies the underlying assumption that, despite the full system being an open system and photons being in non-equilibrium stationary state, the atomic state still

follows an equilibrium thermal distribution. This is a direct consequence of the separation of the time-scales dynamics mentioned at the beginning of this section.

At zero temperature bosons form a Bose-Einstein Condensate with atoms collectively occupying the lowest single particle state, $n(\mathbf{r}) = N|\phi_0^\alpha(\mathbf{r})|^2$. The ground state of the system can be then easily found with a self-consistent iterative procedure, where the lowest energy state is iteratively optimized until the equation for photon amplitude converges,

$$\alpha = \frac{\eta_0}{\Delta_c - U_0\mathcal{N}_{2k_c} + i\kappa} \int \cos(\mathbf{k_c}\cdot\mathbf{r})\cos(\mathbf{k_p}\cdot\mathbf{r})|\phi_0^\alpha(\mathbf{r})|^2 d\mathbf{r}. \tag{2.35}$$

While bosons all contribute to the superradiant scattering into the cavity, for fermions only particles around the Fermi surface can contribute to superradiance. In fact, the Pauli principle suppresses scattering processes to states that are already occupied. Upon diagonalizing the Hamiltonian H_α, the photon amplitude α and an additional equation for fermions fixing the number of particles N must be iteratively solved,

$$\alpha = \frac{\eta_0 N}{\Delta_c - U_0\mathcal{N}_{2k_c} + i\kappa} \int \cos(\mathbf{k_c}\cdot\mathbf{r})\cos(\mathbf{k_p}\cdot\mathbf{r})|\phi_i^\alpha(\mathbf{r})|^2 n_{FD}(\epsilon_i^\alpha) d\mathbf{r}, \tag{2.36}$$

$$N = \int n(\mathbf{r}) d\mathbf{r} = \sum_i \int |\phi_i^\alpha(\mathbf{r})|^2 n_{FD}(\epsilon_i^\alpha) d\mathbf{r}. \tag{2.37}$$

The reliability of the mean-field method is based on the scaling with the volume as, $\sim 1/V$, of the corrections beyond mean-field which in the thermodynamic limit are strongly suppressed, $N \to \infty$, $V \to \infty$ and $N/V = \text{const}$ [2.10]. The mean-field is then valid in the superradiant regime where the coherent build up of a classical field is guaranteed by the constructive interference of the atomic radiation pattern.

2.4.3 Symmetry breaking and Landau theory

As shown in the previous section, the system undergoes a phase transition from a dark to a superradiant state by increasing the transversal pump intensity, η_0. The amplitude Θ measures the crystalline order of the atomic ground state, and smoothly evolves from a vanishing value in the disordered phase to a finite value in the ordered phase. The amplitude Θ acts as an order parameter for a phase transition discerning the phase with structural order from the disordered one. The resulting atomic ground state is not invariant under the symmetry operation of the system Hamiltonian, i.e., it breaks the symmetry of the Hamiltonian.

The transition from the ordered to the disordered state is an example of quantum phase transition driven at $T = 0$ by increasing an external control parameter, here represented by the strength of the transversal drive η_0. The general classification of phase transitions is a problem that dates back to the beginning of the XX century motivated by the discovery in 1932 of the "lambda" transition in superfluid helium [2.11]. Phase transition were first catalogued by Ehrenfest [2.12] in terms of first or second order transition based on the appearance of a discontinuity at the first or second order derivative of the

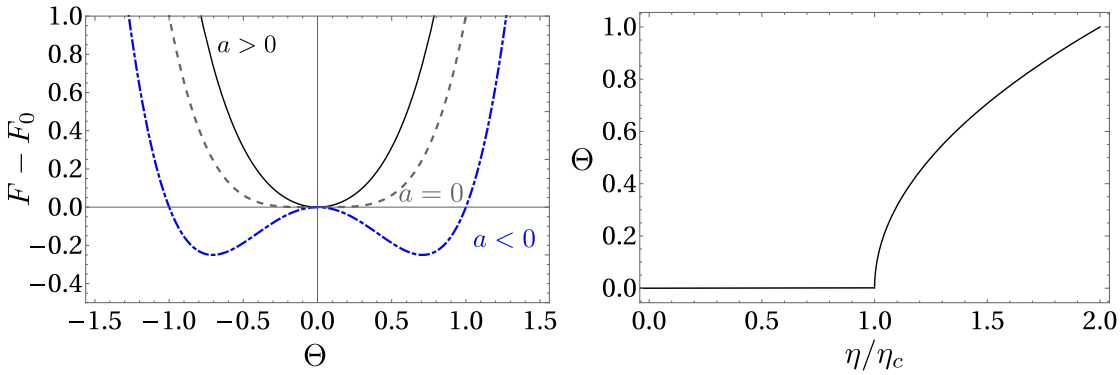

Figure 2.4: a) Free energy of a $|\Theta|^4$-theory for different values of the second order coefficient a and $b = 1$, in arbitrary units. The spontaneous symmetry breaking manifests itself at $a < 0$ (blue dashed-dotted line) with the development of two distinct minima in the free energy. The point $a = 0$ set the critical threshold for a second order phase transition (gray dashed line). b) Typical functional behavior of a mean field order parameter Θ upon assuming that the second-order coefficient has a dependence $a \sim a_0(\eta_c - \eta_0)$ on the external control parameter η_0. The smooth increase of the order parameter across the transition point is an indication of a second order phase transition.

thermodynamical potential (i.e., free energy). This classification is rather obsolete today but the terminology remained intact over time. Instead, the modern classification of phase transitions relies on the presence of latent heat and on the behavior of the order parameter across the transition point.

- In a *first order* phase transition the increase of the order parameter is discontinuous across the transition point. The transition is accompanied by absorption or release of latent heat, and often exhibits hysteresis. Among this class are included transitions in which the system change abruptly from one internal symmetry to another, such as the liquid-crystal transition or the modification of a crystal structure in two different symmetry classes.

- In a *second order* phase transition the order parameter continuously evolves from zero to a non-vanishing amplitude across the transition point. The system gores from a disordered phase to an ordered state with the ground state breaking the symmetry of the Hamiltonian. Examples of this transition include superconductivity, superfluidity in a interacting Bose gases or the Curie ferromagnetic transition.

The modern classification of phase transition strongly relies on the new scheme developed by Landau, who was the first to emphasize the relation between symmetry and phase transitions. He developed a phenomenological approach which deals with the macroscopic features of a system, typically embedded into the order parameter, Θ, and conceals all the microscopic structural details into an effective phenomenological theory.

By assuming that the energy is a smooth continuous functional of the order parameter, the free energy can be expanded in powers of the order parameter in proximity of the transition threshold where the order parameter is small,

$$F[\Theta] = F_0 + a\Theta^2 + b\Theta^4 + c\Theta^6 + \mathrm{o}(\Theta^8), \tag{2.38}$$

where F_0 is the free energy of the disordered state. In the expansion, the linear term in the order parameter is associated with an external static driving field and has been neglected. Since we will deal with systems that possess an inversion symmetry, $\Theta \to -\Theta$, we have also neglected other higher odd powers in the order parameter, which vanish as they would already break the symmetry of the Hamiltonian.

The free energy is illustrated for the simplest case of $c = 0$ in Figure 2.4. The free energy exhibits a single minimum at $\Theta = 0$ for $a > 0$, and a double minima at $\Theta = \pm\sqrt{-a/2b}$ for $a < 0$. The point $a = 0$ set the point at which the phase transition occurs.

Let us now consider the case where the order parameter Θ measures the self-organization of the atomic density in the cavity generated interference potential. If we assume that second order coefficient would scale with the pump intensity as $a \sim a_0(\eta_c - \eta_0)$ and η_0 is the strength of the external pump laser, the condition $\eta_0 = \eta_c$ will determine the threshold for a second order phase transition from a dark to a superradiant phase. The scaling of the second order coefficient with the pump strength η_0 will be demonstrated more rigorously in the next section. In particular we will derive the macroscopic phenomenological coefficient a, b and c introduced in this section in terms of the parameters of the microscopic theory, which are embedded in the Hamiltonian (2.28).

Construction of the Energy Functional

Let us consider the Hamiltonian for a non interacting ultra-cold gas dispersively coupled to a single cavity mode introduced in Section 2.4.1,

$$H[\psi^\dagger, \psi, \alpha^*, \alpha] = -\hbar\Delta_c|\alpha|^2 + \int d\mathbf{r}\hat{\psi}^\dagger(\mathbf{r})\left[-\frac{\hbar^2\nabla_{\mathbf{r}}^2}{2m} + V_{\mathrm{ext}}(\mathbf{r}) + V_{\mathrm{opt}}^{\alpha}(\mathbf{r})\right]\hat{\psi}(\mathbf{r}). \tag{2.39}$$

The Hamiltonian is an indirect functional of the order parameter Θ through the steady state cavity field amplitude,

$$\alpha = \frac{\eta}{\Delta_c - U_0\mathcal{N}_{2k_c} + i\kappa}\Theta. \tag{2.40}$$

The free energy of the system is defined as

$$F = -\frac{1}{\beta}\ln\left[\frac{\mathcal{Z}}{\mathcal{Z}_0}\right] \tag{2.41}$$

where $\beta = 1/k_BT$ is the inverse temperature, $\mathcal{Z}$ is the partition function of the system

$$\mathcal{Z} = \int D(\psi^\dagger, \psi)D(\alpha^*, \alpha)e^{-S[\psi^\dagger,\psi,\alpha^*,\alpha]} = \int D(\psi^\dagger, \psi)D(\alpha^*, \alpha)e^{-\beta H[\psi^\dagger,\psi,\alpha^*,\alpha]}, \tag{2.42}$$

and $\mathcal{Z}_0$ is the partition function of a non-interacting atomic gas for an empty cavity.

In vicinity of the transition point the order parameter is small and we can expand the action S perturbatively in powers of the mean-field amplitude α (thus indirectly of the order parameter Θ). The action can be cast in terms of the atomic propagator $\mathcal{G}^{-1}(\mathbf{r},\tau)$,

$$\frac{S[\psi^\dagger,\psi,\alpha^*,\alpha]}{\beta} = -\hbar\Delta_c|\alpha|^2 + \int d\mathbf{r}\int d\tau\hat{\psi}^\dagger(\mathbf{r})\mathcal{G}^{-1}(\mathbf{r},\tau)\hat{\psi}(\mathbf{r}), \tag{2.43}$$

We can derive an effective theory for the photon field only by integrating out the fermionic degrees of freedom through Gaussian integration [2.13],

$$\frac{S[\psi^\dagger,\psi,\alpha^*,\alpha]}{\beta} = -\hbar\Delta_c|\alpha|^2 + \ln\mathrm{tr}[\mathcal{G}^{-1}(\mathbf{r},\tau)]. \tag{2.44}$$

If $\mathcal{G}_0(\mathbf{r},\tau) = \mathcal{G}(\mathbf{r},\tau)|_{\alpha=0}$ is the atomic propagator in absence of photons, the total propagator $\mathcal{G}(\mathbf{r},\tau)$ is perturbatively expanded as,

$$\mathrm{tr}\ln\mathcal{G}^{-1} = \mathrm{tr}\ln\mathcal{G}_0^{-1}(1+\mathcal{G}_0\Lambda_\alpha) = \mathrm{tr}\ln\mathcal{G}_0^{-1} - \sum_{n=0}^{\infty}\frac{1}{2n}(\mathcal{G}_0\Lambda_\alpha)^{2n}, \tag{2.45}$$

where

$$\Lambda_\alpha(\mathbf{r}) = \hbar U_0\cos^2(\mathbf{k}_c\cdot\mathbf{r})|\alpha|^2 + \hbar\eta_0(\alpha^*+\alpha)\cos(\mathbf{k}_p\cdot\mathbf{r})\cos(\mathbf{k}_c\cdot\mathbf{r}) \tag{2.46}$$

is a matrix that self-consistently depends on the photon amplitude α. Note that only even contribution to the free energy survive and that we have omitted the space and imaginary time index of the Green function for brevity.

The zero order contribution $\mathrm{tr}\ln\mathcal{G}_0^{-1}(\mathbf{r},\tau)$ recovers the free energy of the non interacting atomic gas without cavity photons. The second order term reads as

$$-\frac{1}{2}\mathrm{tr}\ln\mathcal{G}_0\Lambda_\alpha\mathcal{G}_0\Lambda_\alpha = -\frac{\hbar^2\eta_0^2(\alpha+\alpha^*)^2}{2}\mathrm{tr}\ln\langle\mathcal{G}_0(\mathbf{r},\tau)\eta(\mathbf{r})\mathcal{G}_0(\mathbf{r}',\tau')\eta(\mathbf{r}')\rangle + \mathrm{o}(|\alpha|^4), \tag{2.47}$$

with $\eta(\mathbf{r}) = \cos(\mathbf{k}_p\cdot\mathbf{r})\cos(\mathbf{k}_c\cdot\mathbf{r})$ being the space profile of the interference potential. Note that the trace subtends the integration over both space and imaginary time.

The quantity on the right hand side of equation (2.47) is related to density susceptibility of the medium as we will see in the next section,

$$\chi_2 = \ln\langle\mathcal{G}_0(\mathbf{r},\tau)\eta(\mathbf{r})\mathcal{G}_0(\mathbf{r}',\tau')\eta(\mathbf{r}')\rangle, \tag{2.48}$$

and represents the response of the medium to the density perturbations generated by the cavity electromagnetic field.

The total action expanded up the second order in α is,

$$\frac{S^{(2)}[\alpha^*,\alpha]}{\beta} = -\hbar\Delta_c|\alpha|^2 - \frac{\hbar^2\eta_0^2\chi_2(\alpha+\alpha^*)^2}{2}. \tag{2.49}$$

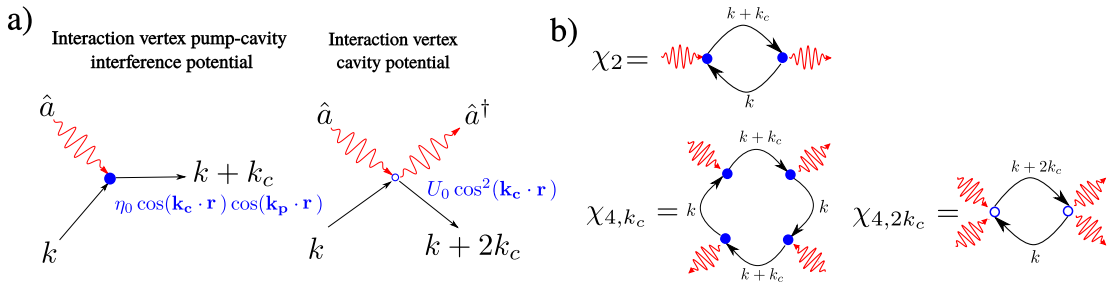

Figure 2.5: 1) Sketch of the interaction vertex between cavity photons and atoms. The solid black arrows represent the atomic propagator at momentum k and the red arrow represent the propagator for a photon with momentum k_c. Left: Typical interaction vertex of the scattering process *from the pump to the cavity* restricted to a one dimension along the cavity axis. A particle propagating with wave-vector k scatter a photon from the cavity into the pump and experiences a momentum kick $k + k_c$. Right: Typical interaction vertex of the scattering process *from and to the cavity* restricted to a one dimension along the cavity axis: a particle with wave-vector k absorbs and emits a photon into the cavity and is scattered to the $k + 2k_c$ momentum. b) Sketch of atomic susceptibility χ_2, χ_{4,k_c} and $\chi_{4,2k_c}$ in terms of one of the four possible momenta combination contributing to it from the scattering with a photon with momentum k_c.

Above the critical point the quadratic action becomes unstable and the expansion must be carried out up to the fourth order. The relevant terms scaling with $|\alpha|^4$ are

$$-\frac{1}{2}\mathrm{tr}\ln(\mathcal{G}_0\Lambda_\alpha)^2 = -\frac{\hbar^2 U_0^2|\alpha|^4}{2}\mathrm{tr}\ln\langle(\mathcal{G}_0(\mathbf{r},\tau)U(\mathbf{r}))^2\rangle + \mathrm{o}(|\alpha|^6) \tag{2.50}$$

$$-\frac{1}{4}\mathrm{tr}\ln(\mathcal{G}_0\Lambda_\alpha)^4 = -\frac{\hbar^2 \eta_0^4(\alpha^* + \alpha)^4}{4}\mathrm{tr}\ln\langle(\mathcal{G}_0(\mathbf{r},\tau)\eta(\mathbf{r}))^4\rangle + \mathrm{o}(|\alpha|^6) \tag{2.51}$$

The first term (2.50) arises from the two-photon absorption from the cavity followed a two-photon emission into the cavity, the second term (2.51) is of higher order and describes four consecutive processes involving the scattering of pump photons into the cavity and viceversa. These processes can graphically pictured in Figure 2.5b.

Overall the portion of the action that scales with the fourth power of α is

$$\frac{S^{(4)}[\alpha^*,\alpha]}{\beta} = -\frac{\hbar^2 U_0^2|\alpha|^4}{2}\chi_{4,2k_c} - \frac{\hbar^4\eta_0^4(\alpha^* + \alpha)^4}{4}\chi_{4,k_c}. \tag{2.52}$$

By using the relationship between the photon amplitude α and the order parameter Θ in Equation (2.20) the energy functional can be recast in a more familiar form,

$$\frac{S[\Theta^*,\Theta]}{\beta} \propto \left(\eta_c^2 - \eta_0^2\right)\Theta^2 + u\Theta^4 \tag{2.53}$$

with

$$\eta_c = \sqrt{-\frac{\Delta_c^2 + \kappa^2}{2\Delta_c \chi_2}} \qquad \text{and} \qquad u = -\frac{\eta_0^2 U_0^2 \chi_{4,2\mathrm{kc}}}{4\chi_2 \Delta_c}\left(1 + \frac{\eta_0^4}{\eta_c^4}\frac{2\Delta_c^2}{U_0^2}\frac{\chi_{4,\mathrm{kc}}}{\chi_2^2 \chi_{4,2\mathrm{kc}}}\right) \tag{2.54}$$

The microscopic theory and the phenomenological description of the phase transition in the vicinity of the critical point are tied together by atomic susceptibility of second, χ_2, and fourth order, χ_{4,k_c} and $\chi_{4,2k_c}$. The order parameter is given by

$$\Theta = \sqrt{-\frac{\eta_c^2 - \eta_0^2}{u}} \tag{2.55}$$

To summarize we have expanded the free energy functional in powers of the order parameters starting from the microscopic Hamiltonian of an ultra-cold gas interacting with a quantized cavity mode. Besides, we have formally demonstrated the scaling of the second order term as a function of the effective pump strength η_0. According the previous section, when the sign of the second order term changes from positive to negative, $\eta = \eta_c$, the system undergoes a second order phase transition. The threshold η_c is uniquely determined by the cavity parameters, $\{\Delta_c, \kappa\}$, and by the second order susceptibility, χ_2. To this extent the forth order term u must be positive. If the fourth order term becomes negative an expansion of the free energy up the sixth order is required. In these conditions the system can undergo a first order phase transition in some regions of the phase diagram. A similar example is given in Chapter 6, where the expansion up the sixth order of the free energy has been carried out explicitly.

The role of the second order susceptibility

Let us now take a deeper look into the behavior of atomic susceptibility χ_2 for an ultra-cold degenerate gas coupled to a single mode of a linear cavity. For simplicity we will only deal with non-interacting degenerate gases at $T = 0$, and we will restrict to a one-dimensional case: ideally the gas is confined into a cigar shaped trap elongated along the cavity axis so that the physics along the transversal direction can be neglected. Hence, only longitudinal momentum kicks $\Delta k = \pm k_c \hat{x}$ are experienced by the atom by scattering cavity photons.

At zero temperature the excitation energy for an atom in the cloud can only arise from the absorption and emission of photons propagating at the cavity wave-vector $q = \pm k_c$. The single particle excitation energy in this process is just the difference between the bare atomic energies, $\Delta E_{\pm k_c} = \hbar^2(k \pm k_c)^2/2m - \hbar^2 k^2/2m$, and is a fundamental quantity in the calculation of the density-density correlation function $\chi_D(q, \omega)$. The density correlation function set the response of the atomic medium to an external perturbation propagating at a wave-vector q and with energy ω, and can be then easily calculated by doing a re-summation of the Matsubara frequencies [2.14],

$$\chi_D(q, \omega) = \sum_k \frac{n_{FD(B)}(\epsilon_{k+q}) - n_{FD(B)}(\epsilon_k)}{\hbar\omega + \epsilon_{k+q} - \epsilon_k + i0^+}. \tag{2.56}$$

Here, $n_{FD(B)}$ is the statistical distribution of the atomic gas, and $\epsilon_k = \hbar^2 k^2/2m$ are the atomic energies for an empty cavity.

At zero temperature the bosonic statistical distribution can be approximated as a Dirac function, $n_B(\epsilon_k) = N\delta(k=0)$, and the atomic susceptibility of Equation 2.48 can be written in terms of the density susceptibility as,

$$\chi_2 = \frac{1}{2}\chi_D(k_c, 0) = -\frac{N}{E_R} \tag{2.57}$$

The threshold for the Dicke phase transition is easily retrieved as $\sqrt{N}\eta_{\text{Dicke}} = \sqrt{E_R(\Delta_c^2 + \kappa^2)/2\Delta_c}$ [2.15, 2.16]. This result can be intuitively understood if one thinks of the scattering processes that are available when a Bose-Einstein condensate interact with photons (see Figure 2.6). When the cavity is empty the density is uniform, and all particles are condensed in the $k = 0$ state. Only two scattering processes can occur and contribute to the susceptibility in Equation 2.48: either the whole cloud is the $k = 0$ momentum and acquires a momentum kick $q = \pm k_c$ from the absorption (emission) of a photon, or the atoms are in the excited state $k = \pm k_c$ and are scattered back to the $k = 0$ state by emitting (absorbing) a photon. The energy difference in both processes is the recoil energy of the atomic species, $\Delta E = E_R = \hbar k_c^2/2m$, which sets the scaling as $\chi_2 \sim 1/E_R$ of the static susceptibility for bosons. The collective atomic response produces a coherent enhancement of the susceptibility $\chi_2 \sim N$, scaling with the total atom number N rather than with the density $n = N/L$ of the condensate.

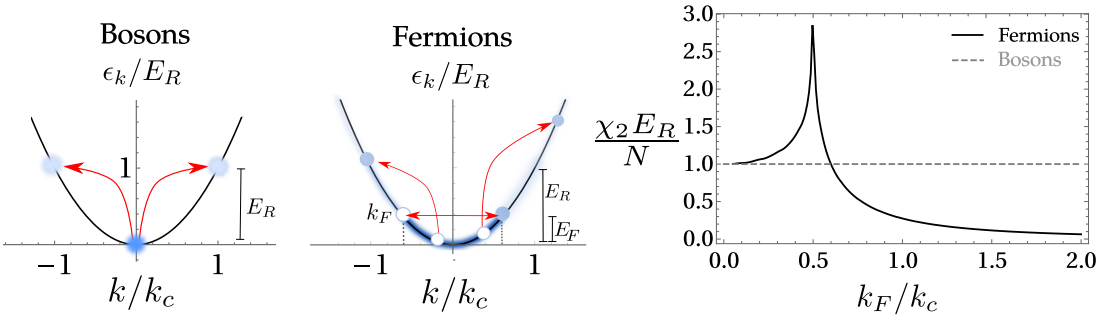

Figure 2.6: Single particle spectrum of a non interacting atomic gas, $\epsilon_k = \hbar^2 k^2/2m$, and cavity-induced scattering processes as red arrows for bosons and fermions at half filling, $k_F/k_c = 1/2$. For fermions the particle-hole excitations create a hole in the Fermi sea (dark shaded area in the energy dispersion) and scatter it above the Fermi surface. When the *nesting condition* is realized, $k_c = 2k_F$, the scattering from one side of the Fermi surface to the other is resonant (horizontal red arrow). The adimensional atomic susceptibility $\chi_2 E_R/N$ is showed as a function of k_F/k_c for fermions as a solid black line. The nesting of the Fermi surface induces a divergence in the atomic susceptibility at $k_F/k_c = 1/2$. For comparison we also show the value of susceptibility for bosons which does not depend on the density of the gas (gray dashed line).

In contrast, the fermionic susceptibility exhibits a complex structure which introduces a non trivial dependence on the atomic density n. Due to the Pauli principle each state can only be occupied by one fermion, and due to the build up of a Fermi surface a new length scale, set by the Fermi momentum k_F, is introduced. Commensurability effects between the the cavity wave-vector k_L and the Fermi momentum k_F induce a non-trivial dependence of the susceptibility on the density of the medium [2.17]. For a non interacting Fermi gas the density susceptibility coincides with the Lindhard function, which describes the response of an electron gas to an electromagnetic field [2.18, 2.19]. Note however that here all the electrons are bound to the nuclei of the atoms and there are no free charges. The shape of the polarizability arise due to the effective coupling with the electromagnetic field in the dispersive regime which acts on the density as seen in Section 2.4.1.

In Figure 2.6 we show the density susceptibility for a Fermi gas in one dimension as a function of the density, $n \sim k_F$. The divergence of the susceptibility at $k_F/k_c = 0.5$ is a consequence of the nesting of the Fermi surface. That is, at $k_c = 2k_F$ a scattering process with the photon induces resonant gapless excitation from one side of the Fermi surface to the other, resulting in the divergence of the susceptibility and a drastic suppression of the critical threshold. The nesting effect is rather fragile, and is directly smeared out by increasing temperature, trap averaging and changing dimensionality [2.19, 2.20].

The susceptibility $\chi_2(\omega)$ also defines the properties of light and affects the refractive index of the medium. This is evident if we extend the mean-field theory to the Gaussian fluctuations $\delta\hat{a}$ [2.10]. The propagator of the cavity electromagnetic field is

$$D^{-1}(\omega) = \begin{bmatrix} \omega + \delta_c + i\kappa - \frac{\eta_0^2}{2}\chi_2(\omega) & -\frac{\eta_0^2}{2}\chi_2(\omega) \\ -\frac{\eta_0^2}{2}\chi_2^*(-\omega) & -\omega + \delta_c - i\kappa - \frac{\eta_0^2}{2}\chi_2^*(-\omega) \end{bmatrix} \tag{2.58}$$

with $\chi_2^*(-\omega) = \chi_2(\omega)$. The poles of the cavity propagators $\mathrm{Det}[D^{-1}(\omega_{\mathrm{pol}})] = 0$ determine the frequency of the collective excitations of the system which arise from the mixing of density fluctuations at k_c and photons, i.e., *polariton*. The phase transition to the superradiant regime can be then interpreted as mode softening of the lowest energy polariton branch.

2.4.4 Observation of the self-ordering phase transition

The superradiant self-organization of an atomic gas into a cavity-generated optical potential was first experimentally demonstrated for thermal atoms at MIT in 2003 [2.21]. Laser cooled Cesium atoms self-assembled into a Bragg grating diffracting light into the cavity. The observation of random π phase jumps in the measurement of the phase of the out-coming light demonstrated the symmetry breaking of the $\mathbf{Z}_2$ symmetry of the Hamiltonian. Later on the superradiant phase transition was observed for quantum degenerate gases in the Zürich experiment of 2010 for the first time [2.22]. A BEC of 10^5 atoms was transverally pumped by a far red-detuned laser beam. The pump power was progressively increased until the system would enter the superradiant phase and a two-dimensional interference checkboard lattice was formed. Atoms trapped in such

potential macroscopically populate four momentum state $\mathbf{k}_{\pm,\pm} = (\pm k_c; \pm k_c)$, which were measured through absorption imaging after time of flight expansion. The symmetry breaking of translational symmetry was proven using heterodyne detection, demonstrating the locking of the phase of the cavity field with a 0 or π relative phase with respect to the pump field. The two phases coincide with the occupation of even or odd sites of the resulting checkboard lattice [2.23]. The excitation spectrum and mode softening of the $\mathbf{k}_{\pm,\pm}$ momentum states in the dispersion relation of the condensate was later on measured in [2.24].

2.5 Conclusions

In this Chapter we have examined some pivotal aspects of light-matter interaction from a classical point of view. After highlighting the effect of dielectric materials on the propagation of light, we showed that coupling a polarizable particle to an optical resonator can coherently enhance the coupling between light and matter. We have therefore described the cooperative effects established from coupling atomic ensembles to the light fields in an optical cavity. Finally dealing with ultra-cold quantum gases, we showed how superradiance and self-organization are linked to a phase transition where the $\mathbb{Z}_2$ symmetry of the Hamiltonian is broken by the ground state.

The concepts outlined in this Chapter are fundamental for the understanding the non-linear effects that arise from the coupled photon-atom dynamics described in the following part of this Thesis. In particular, the next two Chapters will be devoted to extend the theory here presented to two particular cases of study: the self-organization set up for multi-component degenerate gases, in Chapter 3, and the generation of cavity-mediated artificial gauge fields, in Chapter 4.

From the methodological point of view this Chapter introduces the main techniques adopted throughout the Thesis:

- The mean-filed tool introduced through the pedagogical example of a transversally pumped cavity will be adopted in all the publications presented in this Thesis, in Chapter 5 and 6;
- The importance of the susceptibility of a quantum gas will be a recurrent theme and it will appear again in Chapter 5, and in Chapter 6 where an explicit expansion of the free energy is accomplished up to sixth order in the order parameter.

3 Many-body physics with spinor quantum gases in optical cavities

The previous Chapter introduced the main features of light-matter interaction within a cavity, and important tools to study the self-organization of atomic gases in cavity generated potentials. This Chapter focuses on self-organization with respect to the internal degrees of freedom of multi-level atomic systems, which typically includes electron spin and nuclear spin of the atoms. After introducing the tool of two-photon Raman transitions, upon which most models of spin self-organization are based upon, we will discuss the features of the superradiant phase transition in multi-level atomic systems and lay out the future perspectives that this novel field of study has opened.

3.1 Introduction

Due to the delocalization of a photon in the electromagnetic field modes throughout the cavity, a photon emitted by one atom can be absorbed by any other particle in the mode at an arbitrary distance. For dispersively coupled ensembles as seen in Chapter 2, the consecutive photon absorption and emission by two different atoms mediate long-range two-body forces that are insensitive to the internal state of the atom. This rules out any possibility to investigate the interplay between mechanical and internal degrees of freedom on self-organization. Hence we need to find new spin-dependent coupling mechanisms, which can simulate long-range interactions among particles in two different internal states.

Multi-level atoms optically driven on independent transitions can be reduced to an effective two-level manifold, when the excited states are far from resonance. That is, two isolated hyperfine levels of an atom can be coupled through an effective Rabi frequency by multiple photon optical transitions through virtually populated excited states according to the appropriate selection rules. The resulting two-level manifold follows the same spin algebra as a spin 1/2 and can be used for building quantum simulation devices that simulate the behavior of electronic matter, i.e, Fermi-Hubbard model. In Section 3.2 we will present the simplest among such multi-photon transitions schemes. It consists of a stimulated Raman process, where two ground states of a three-level atom are coupled through a far detuned excited state by a two-photon transition, i.e., a so called *lambda* scheme. In such conditions the two ground state levels are coupled by an effective two-photon Rabi frequency, realizing a "spin"-dependent term in the Hamiltonian, where the population of the spin- or pseudospin- components is not conserved. When the underlying Raman process is enhanced by a cavity mode, the coupling between atom

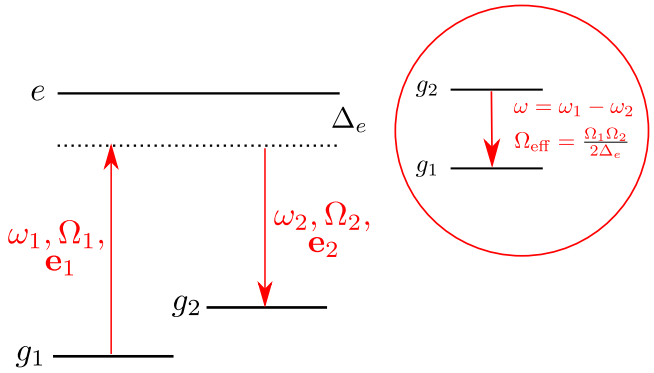

Figure 3.1: Stimulated Raman transition in a three-level system: an atom goes from a ground state $|g_1\rangle$ to a second ground state $|g_2\rangle$ via the absorption of a photon at frequency ω_1 and stimulated emission of a photon of frequency ω_2. Inset: The system effectively behave like a two-level system interacting with a monochromatic light of frequency $\omega = \omega_1 - \omega_2$ and Rabi frequency $\Omega_{\text{eff}} = \Omega_1\Omega_2/2\Delta_e$

and photons becomes non-linear and dynamical, in analogy to the conventional self-organization schemes. We will show in Section 3.3 the simplest and most general cavity configuration, which allows to generate a spin-dependent coupling Hamiltonian. Such effective realizations of spinor interactions pave the way for the simulation of quantum magnetism, spin-orbit coupling and long-range spin-spin interactions in cavity systems.

3.2 Stimulated Raman transition

Stimulated Raman processes are the main tool adopted in typical set-ups for the realization of spin self-organization in multi-level atomic system. A stimulated Raman process is a two-photon transition which resonantly couples two atomic ground state levels, say $|g_1\rangle$ and $|g_2\rangle$, via the consecutive absorption and stimulated emission from two independent laser fields. A typical lambda transition as shown in Figure 3.1 is the most basic example of such processes. The ground state $|g_1\rangle$ ($|g_2\rangle$) is coupled to a far detuned excited state $|e\rangle$ via a laser field of Rabi constant Ω_1 (Ω_1) and frequency ω_1 (ω_2). If the frequencies of the driving lasers are very far detuned from the excited state. $\Delta_e \gg \Omega_i, \omega$, the system effectively behaves like a two-level atom excited by a monochromatic light with excitation frequency $\omega = \omega_1 - \omega_2$, and with effective Rabi frequency

$$\frac{\hbar\Omega_{\text{eff}}}{2} = \frac{\hbar\Omega_1\Omega_2}{4\Delta_e}. \tag{3.1}$$

For atomic systems, the same coupling could alternatively be realized by direct coupling of the two hyperfine states through a microwave driving field. However, the advantage of using optical transitions relies in the simultaneous coupling to both the internal and

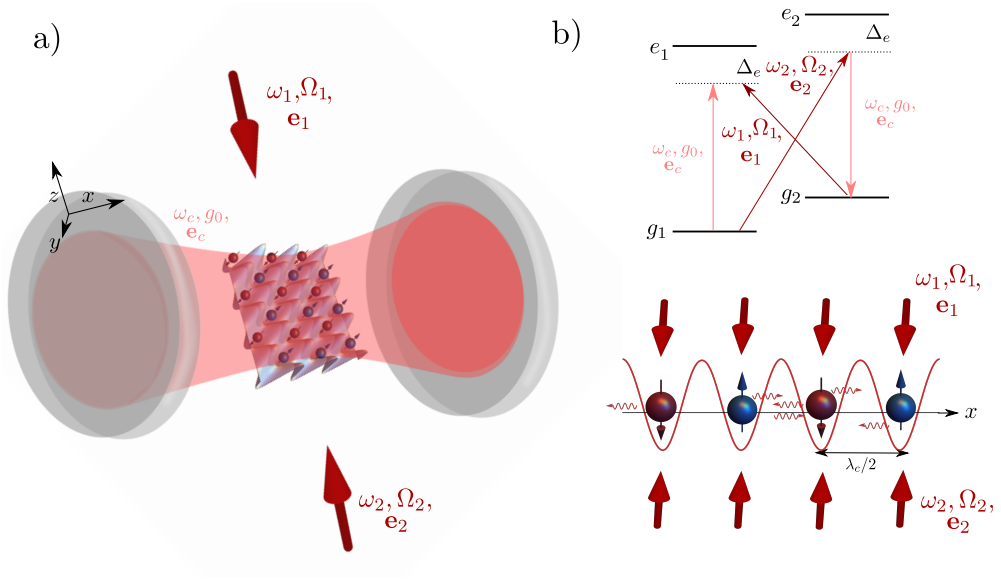

Figure 3.2: Typical set-up for the study of spin self-organization in a), and atomic level structure adopting a *butterfly* pumping configuration in b). Two independent transversal pump lasers of Rabi frequency Ω_1 and Ω_2 drive two independent transitions of ultra-cold gas prepared in an equal mixture of two hyperfine states, say $|g_1\rangle$ and $|g_2\rangle$. The Bragg scattering into the cavity favours the emergence of complex spin textures, and the emerging optical lattice potential traps the atoms at its minima inducing a density modulation as well. On the bottom side of b) a sketch of an anitferromagnetic spin texture is shown.

external degrees of freedom. In fact, for two counter-propagating lasers the photon scattering process induces an appreciable momentum transfer $\hbar(\mathbf{k}_1 - \mathbf{k}_2) \sim \hbar 2k_1$, which finds numerous applications from laser cooling and momentum distribution measurement thorough Bragg scattering methods, to coherent population trapping and phase imprinting on the atomic wave-function [3.1].

3.3 Multi-component atomic gases coupled to optical cavities

A very general theoretical model that takes into account both density and spin self-ordering can be found in Ref. [3.2]. In order to avoid the trapping of population in the dark state for the *lambda* transition scheme, a repumping mechanism from the second ground state to the first is needed. Then to avoid the problem of a decoupled dark state, it is preferable to adopt two independent stimulated Raman transitions, also known as *butterfly* scheme, as shown in Figure 3.2b.

When the excited state is adiabatically eliminated, the effective Hamiltonian reduces

to the spin 1/2 manifold, $\hat{H} = \Delta_c \hat{a}^\dagger \hat{a} + \int d\mathbf{r} \hat{\Psi}^\dagger(\mathbf{r}) \hat{\mathcal{H}}_{\text{eff}} \hat{\Psi}(\mathbf{r})$. Here the components of the vector $\hat{\Psi}(\mathbf{r}) = \left(\hat{\psi}_\uparrow(\mathbf{r}), \hat{\psi}_\downarrow(\mathbf{r})\right)$ are the atomic destruction operator for a particle at position $\mathbf{r}$ and with spin σ, and $\hat{a}$ is the photon destruction operator. The Hamiltonian density then is given by:

$$\hat{\mathcal{H}}_{\text{eff}} = \hbar \begin{pmatrix} -\frac{\hbar\nabla^2}{2m} + \delta + \hat{V}_\uparrow(\mathbf{r}) & \Omega_R(\mathbf{r}) \\ \hat{\Omega}_R^*(\mathbf{r}) & -\frac{\hbar\nabla^2}{2m} + \hat{V}_\downarrow(\mathbf{r}) \end{pmatrix}, \tag{3.2}$$

with δ being the effective frequency difference between the two pseudospin states. In analogy with the self-organization of a one component quantum gas, there is a periodic potential acting on the density

$$\hat{V}_\sigma(\mathbf{r}) = \hbar \frac{|\Omega_\sigma(\mathbf{r})|^2}{\Delta_e} + \hbar U_\sigma \cos^2(\mathbf{k}_c \cdot \mathbf{r})\, \hat{a}^\dagger \hat{a} \tag{3.3}$$

which include the pump generated potential, with $\Omega_\sigma(\mathbf{r})$ being the space profile of the classical pump lasers, and the cavity generated optical lattice with depth, $U_\sigma = g_\sigma^2/\Delta_e$.

Raman scattering processes between the cavity and the pump lead to local spin flips, which are driven by an effective two-photon Rabi frequency

$$\hat{\Omega}_R(\mathbf{r}) = \eta_\uparrow^*(\mathbf{r})\hat{a} + \eta_\downarrow(\mathbf{r})\hat{a}^\dagger, \tag{3.4}$$

where we have defined $\eta_\sigma = g_\sigma \Omega_\sigma / \Delta_e$. Then the steady state cavity amplitude is

$$\alpha = \langle \hat{a} \rangle = \frac{\int d\mathbf{r} \left[\eta_\uparrow(\mathbf{r}) s_-(\mathbf{r}) + \eta_\downarrow(\mathbf{r}) s_+(\mathbf{r})\right]}{\Delta_c + i\kappa - \int d\mathbf{r} \left[U_\downarrow(\mathbf{r}) n_\downarrow(\mathbf{r}) + U_\uparrow(\mathbf{r}) n_\uparrow(\mathbf{r})\right]} \tag{3.5}$$

where $n_\sigma(\mathbf{r}) = \langle \hat{\psi}_\sigma^\dagger(\mathbf{r}) \hat{\psi}_\sigma(\mathbf{r}) \rangle$ and $\mathbf{s}(\mathbf{r}) = \langle \hat{\Psi}^\dagger(\mathbf{r}) \hat{\boldsymbol{\tau}} \hat{\Psi}(\mathbf{r}) \rangle$ are the local atomic density average and local spin average with, $\hat{\boldsymbol{\tau}}$, being the vector of Pauli matrices.

The steady state value of the cavity field can be directly plugged in the Hamiltonian $\hat{H}$, giving rise to effective spin-spin interactions which include long-range Heisenberg-type terms, $\hat{\mathbf{s}}(\mathbf{r}') \cdot \hat{\mathbf{s}}(\mathbf{r})$, favouring ferromagnetic or antiferromagnetic ordering, and more complex Dzyaloshinskii-Moriya-type couplings, $\hat{\mathbf{s}}(\mathbf{r}') \times \hat{\mathbf{s}}(\mathbf{r})$, favouring chiral states such as skyrmions and spin spirals [3.3].

Adopting different pumping schemes allows the simulation of a plethora of different spin interacting models. Several theoretical studies demonstrated the self-organization in magnetic structures above a critical pump intensity when ultra-cold gases are coupled to single or multi-mode cavities. These structure range from ferro- and ferri-magnetic spin lattices as shown in an early proposal [3.4], to antiferromagnetic spin waves [3.5]. More complex schemes adopting several modes result in cavity mediated spin orbit coupling leading to spin-spirals [3.6], and spin-helix or supersolid spin-density-wave in two dimensions [3.7]. In the blue detuning, introducing a polarization gradient along the cavity axis allows to investigate the competition between long-range density-density, spin-density and spin-spin interactions, thus implementing a generalized t-J-V-W model with even richer phase diagram [3.8]. From a completely different perspective, the cavity can also stabilize spin liquid states in frustrated systems [3.9].

From the experimental point of view, the typical level structure shown in Fig. 3.2 is at the base of the realization of an open Dicke model in Ref. [3.10], which constitutes the first observation of superradiance spin self-organization for thermal atoms. More recently, a superradiant spin density wave in a spinor BEC coupled to an optical resonator above a critical pump strength was observed [3.11], which constitute the first experiment to realize a dynamical spin-orbit coupling in a cavity.

3.4 Concluding remarks

In this Chapter we reviewed some aspects of the superradiant self-organization in multi-component quantum gases. We introduced the physics of Raman transition as a tool for generating photon spin-dependent couplings that affects the center of mass motion of the atoms. The coupling to a cavity results into effective long-range spin-spin interactions which stabilize exotic states of matter such as spin liquids, ordered magnetic structures, and topological chiral states.

This Chapter introduces the fundamental concepts which will be relevant for the publication in Chapter 5, where we will study the properties of the self-organization phase transition for a spinor Fermi gas coupled to a two-mode ring cavity. In this system spin-resolved two-body correlations arise between particles in momentum states differing by the cavity wave-vector, thus remarking the significance of two-photon Raman transitions for the coupling between internal and external degrees of freedom of the atoms.

4 Emulating artificial gauge fields in cold atom lattices

This Chapter introduces the concept of artificial gauge fields relevant for the dynamical examples presented in Chapters 6 and 7. After briefly introducing the concept of gauge freedom with electromagnetic potentials as an example, we will describe how gauge fields can be implemented on a lattice. We will deal then with the problem of how to generate synthetic gauge fields for neutral atoms, and what are the advantages in coupling ultra-cold atoms to the electromagnetic fields in a cavity rather than in free space.

4.1 Introduction

In the previous Chapters we have discussed symmetry breaking mechanisms in the context of superradiance and self-organization of an ultra-cold gas coupled to an intra-cavity electromagnetic field. The symmetries that we have discussed so far are global. That is, the symmetry operation acts at every point in space and time the same way, and is associated to some conserved quantity in the system [4.1]. In the context of the self-organization phase transition in a linear cavity, the Z_2 symmetry associated in Chapter 2 with the transformation $\hat{a} \rightarrow -\hat{a}$ is coupled to a translational shift $x \rightarrow x + \lambda$ of the whole space, which identically acts on each position of the particle the same way. Such Z_2 symmetry guarantees the conservation of the number of excitations in the system.

Along with global symmetry operations, local transformations that leave invariant the Hamiltonian can only act on a single point in space and time. Among these there is a particular set of transformations, which are not associated with any conserved quantities, but rather they are mathematical operations that do not induce any measurable physical consequences. These constructs are called gauge freedom, and are often associated to the presence of redundant degrees of freedom in the way we describe Nature.

To illustrate a trivial example of gauge freedom we can consider the choice of a coordinate system or of the temperature scale [4.2]. The choice of Cartesian or a spherical coordinates will affect the form of the equations of motion describing the dynamics of an object in space, but it will not change its actual physical trajectory. Similarly, choosing to use the Celsius or Fahrenheit temperature scale will not change the temperature of an object. These choices are completely arbitrary and do not affect the physics of the system.

In fact the term gauge freedom was first conceived by Hermann Weyl in 1919 as *eichinvarianz* in his book *Raum, Zeit und Materie*, where the term *eich* refers to a change in scale of a measurement device [4.3]. Weyl introduced this concept in an unsuccessful

attempt to unify gravity with electromagnetism, after realizing the invariance of the general relativity equations under a local transformation. With the advent of quantum mechanics Schrödinger derived the equation of motion for a charged particle in an external electromagnetic field [4.4], and Fock demonstrated that the quantum mechanical wave equation is invariant under a local symmetry transformation provided the wave-function is transformed accordingly [4.5]. We will see these concepts in more detail in Section 4.3. At that point Weyl soon realized that the concept of gauge invariance. which he coined years back ties together electricity and matter, rather than electricity and gravity. Since then the term *gauge invariance* or *gauge symmetry* was accepted by the scientific community. The principle of gauge freedom became a touchstone for modern physics, being at the basis not only of classical electromagnetism and quantum electrodynamics, but also for the Standard model and quantum chromodynamics.

Due to the ubiquitous presence of gauge theories throughout our modelling of Nature, artificially recreating typical phenomena of interacting gauge potentials enables to probe the limits of such theories. The problem of building a quantum simulator for gauge theories requires understanding how to simulate an artificial Aharonov-Bohm phase in free space and on a lattice, as we will see in Section 4.4. At this day ultra-cold atoms have already proved to be a resourceful tool and quantum simulators for charged matter interacting with static magnetic and electric fields have been successfully implemented [4.6]. We will briefly review such schemes in Section 4.5 along with some theoretical proposals adopting optical cavity potentials. We will show that in hybrid light-matter systems the synthetic magnetic field dynamically and spontaneously arises along with superradiance and could ultimately open the possibility to a the quantum simulation of genuine gauge theories.

4.2 Maxwell electromagnetism and gauge transformations

Let us start out with the simplest of the gauge theories that we can construct, Maxwell theory of classical electromagnetism. The physical observables of the theory such as the electric, $\mathbf{E}$, and magnetic, $\mathbf{B}$, fields, are often rewritten in terms of a four-potential $A_\mu = (\phi, -\mathbf{A})$, with ϕ and $\mathbf{A}$ respectively being a scalar and vector potential. In a chosen rest frame the electric and magnetic fields are related to the potentials through the relations

$$\mathbf{E} = -\nabla\phi - \frac{\partial \mathbf{A}}{\partial t} \qquad\qquad \mathbf{B} = \nabla \times \mathbf{A}, \tag{4.1}$$

and the electromagnetic field action

$$S_{e.m} = \frac{1}{2\mu_0} \int dt d\mathbf{r} \left(\frac{1}{c^2}\mathbf{E}^2 - \mathbf{B}^2 \right) \tag{4.2}$$

is invariant under gauge transformations of the form

$$\phi(\mathbf{r}, t) \to \phi(\mathbf{r}, t) - \frac{\partial \chi(\mathbf{r}, t)}{\partial t}, \tag{4.3}$$

$$\mathbf{A}(\mathbf{r}, t) \to \mathbf{A}(\mathbf{r}, t) + \nabla\chi(\mathbf{r}, t), \tag{4.4}$$

where $\chi(\mathbf{r}, t)$ is an arbitrary local time-dependent function. The electric field and the magnetic fields are gauge invariant as they do not depend on the choice of the function $\chi(\mathbf{r}, t)$.

The gauge freedom in the context of classical electromagnetism is understood as a redundancy in the degrees of freedom of the theory. Of the four terms of the vector potential, only three components are needed to derive the electric and magnetic fields, given the restrictions of the Maxwell equations. One of the components of the vector potential is thus trivial or redundant, and can be arbitrarily fixed.

4.3 Schrödinger equation in a magnetic field

Let us now discuss the significance of a gauge transformations in quantum mechanics by considering the quantum behavior of a charged particle in an external magnetic field. The Schrödinger equation describing the time evolution of the matter wave-function is

$$i\hbar\frac{\partial\psi(\mathbf{r})}{\partial t} = \frac{1}{2m}\left[(-i\hbar\nabla - q\mathbf{A}(\mathbf{r},t))^2 + q\phi(\mathbf{r},t)\right]\psi(\mathbf{r}) = H\psi(\mathbf{r}). \tag{4.5}$$

Here $\mathbf{A}(\mathbf{r}, t)$ and $\phi(\mathbf{r}, t)$ are the vector and scalar potential introduced in the previous section, and

$$H = \frac{1}{2m}(\mathbf{p} - q\mathbf{A}(\mathbf{r},t))^2 + q\phi(\mathbf{r},t) \tag{4.6}$$

is the Hamiltonian of a charged particle in *minimal coupling*. In quantum mechanics the gauge potentials play a central role as the vector potential $\mathbf{A}(\mathbf{r}, t)$ is directly appearing in the Hamiltonian and coupling to the canonical momentum $\mathbf{p} = -i\hbar\nabla$. The electromagnetic potentials are, as stated above, defined only up to a gauge transformation as in Equation 4.4. The Hamiltonian accordingly transforms under the same transformation as

$$H_\chi = \frac{1}{2m}(\mathbf{p} - q\mathbf{A}(\mathbf{r},t) - q\nabla\chi(\mathbf{r},t))^2 + q\phi(\mathbf{r},t) - q\frac{\partial\chi(\mathbf{r},t)}{\partial t} \tag{4.7}$$

At first look it would seem that the Hamiltonian and the Schrödinger equation are not invariant under gauge transformations. However, the physics of the system must stay the same as the electric and magnetic fields, which give rise to the physical observables are gauge invariant.

Hence to keep physical observables invariant under the gauge transformation , the wave-function must be also transformed according to a local time-dependent unitary transformation

$$\psi_\chi \equiv \exp\left(i\frac{q\chi(\mathbf{r},t)}{\hbar}\right)\psi. \tag{4.8}$$

The transformed wave-function then satisfies the transformed Schrödinger equation of motion

$$i\hbar\frac{\partial\psi_\chi}{\partial t} = H_\chi\psi_\chi. \tag{4.9}$$

From this example we see that a gauge transformation in quantum mechanics requires the wave-function to pick up a *geometric* phase, which only depends on the geometry of

the path taken by the particle and not on the velocity of the particle itself. While it is locally hard to observe, such geometric phase can be still measured through matter-wave interferometry as was first proposed in 1959 by Aharonov and Bohm in a famous *gedanken* experiment [4.7]. This was successfully demonstrated by Tonomura in 1982 [4.8]. The geometrical nature of such phase is the crucial aspect that paves the way towards the quantum simulation of synthetic gauge fields in neutral atoms [4.9].

4.4 Gauge fields on a lattice

A charged particle that moves freely in space in an external magnetic field B undergoes a uniform oscillatory motion at the cyclotron frequency $\omega_c = |q|B/m$. If particles are confined in a periodic potential, the magnetic length set by the minimal orbit size, $\ell_b = \sqrt{\hbar/qB}$, and the lattice constant a determine the two important length scales of the system. The strength of the magnetic field piercing the plaquette of the lattice can be directly written as a ratio of these two lengths,

$$2\pi\frac{\Phi}{\Phi_0} = \frac{a^2}{\ell_b^2}. \tag{4.10}$$

When the flux is small, the cyclotron orbit is much bigger than the lattice size and the orbit of the charged particle will span many units cell so that lattice structure is not felt by the particle. When the orbit becomes of the same size as the lattice cell, the competition of the two length scales becomes important and a plethora of new effects become observable.

To look at these effects we need to derive the lattice Hamiltonian describing the physics of a charged particle q in a periodic lattice. Consider the basic Hamiltonian written in the previous section,

$$H = \frac{\left(\mathbf{p} - q\mathbf{A}(\mathbf{r})\right)^2}{2m} + V(\mathbf{r}), \tag{4.11}$$

where $V(\mathbf{r}) = V(\mathbf{r} + \mathbf{a})$ is an additional periodic potential with lattice constant a, the scalar gauge potential is zero everywhere $\phi(\mathbf{r}, t) = 0$ and $\mathbf{A}(\mathbf{r})$ is a static vector potential. For vanishing potential $\mathbf{A}(\mathbf{r}) = 0$, the eigenstates with energies $\epsilon_{n,\mathbf{k}}$ of the system are Bloch states $\phi_{n,\mathbf{k}}(\mathbf{r}) = e^{i\mathbf{k}\cdot\mathbf{r}}u_{n,\mathbf{k}}(\mathbf{r})$ with the same periodicity of the external optical lattice, $u_{n,\mathbf{k}}(\mathbf{r} + \mathbf{a}) = u_{n,\mathbf{k}}(\mathbf{r})$.

If the optical potential is deep, it is easier to write the Bloch functions in terms of localized Wannier states,

$$\phi_{n,\mathbf{k}}(\mathbf{r}) = \sum_m e^{i\mathbf{k}\cdot\mathbf{R}_m} w_n(\mathbf{r} - \mathbf{R_m}), \tag{4.12}$$

where $\mathbf{R_m} = m\mathbf{a}$ is the position of the m-lattice site .

In presence of a vector potential the wave-function acquires a phase defined by the circulation of the vector potential over the path enclosed by it. As a result the new Bloch wave function,

$$\tilde{\phi}_{n,\mathbf{k}}(\mathbf{r}) = \sum_m e^{i\frac{q}{\hbar}\int_{\mathbf{R_m}}^{\mathbf{r}} \mathbf{A}(\mathbf{r}')d\mathbf{r}'} e^{i\mathbf{k}\cdot\mathbf{R}_m} w_n(\mathbf{r} - \mathbf{R_m}), \tag{4.13}$$

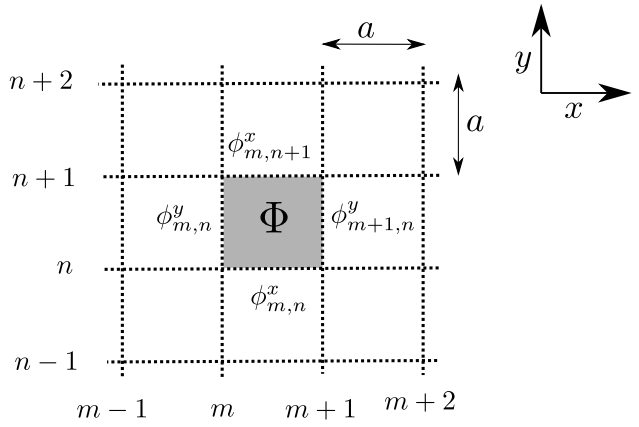

Figure 4.1: Sketch of a 2D optical lattice pierced by a magnetic field. The flux on a single plaquette Φ depends on the values of the Peierls phases $\phi^{x,y}_{m,n}$ at links between the plaquette vertices.

has acquired a phase proportional to the vector potential $\mathbf{A}$ as, $\propto \frac{q}{\hbar}\int_{\mathbf{R_m}}^{\mathbf{r}} \mathbf{A}(\mathbf{r}')d\mathbf{r}'$. The Hamiltonian in the new localized basis is

$$H = \sum_{n,m} \tilde{J}_{n,m}\hat{b}^\dagger_n \hat{b}_m + \tilde{J}^*_{n,m}\hat{b}^\dagger_m \hat{b}_n, \tag{4.14}$$

with the hopping parameter defined as

$$\tilde{J}_{n,m} = -\int d\mathbf{r}\tilde{\phi}^*_{n,\mathbf{k}}(\mathbf{r})\left[\frac{(\mathbf{p}-q\mathbf{A}(\mathbf{r}))^2}{2m} + V(\mathbf{r})\right]\tilde{\phi}_{n,\mathbf{k}}(\mathbf{r}) \tag{4.15}$$

$$\simeq -e^{i\frac{q}{\hbar}\int_{\mathbf{R_n}}^{\mathbf{R_m}} \mathbf{A}(\mathbf{r}')d\mathbf{r}'}\int d\mathbf{r}\phi^*_{n,\mathbf{k}}(\mathbf{r})\left[\frac{\mathbf{p}^2}{2m} + V(\mathbf{r})\right]\phi_{n,\mathbf{k}}(\mathbf{r}) \tag{4.16}$$

$$\simeq -J_{n,m}e^{i\frac{q}{\hbar}\int_{\mathbf{R_n}}^{\mathbf{R_m}} \mathbf{A}(\mathbf{r}')d\mathbf{r}'}. \tag{4.17}$$

In presence of a static vector potential $\mathbf{A}(\mathbf{r})$ the tunneling amplitudes $J_{n,m}$ of the Hubbard Hamiltonian [4.10] have to acquire a phase shift which depends on the local value of the vector potential at the links between the sites. This procedure is also known in literature as Peierls substitution [4.11]. The total flux enclosed by a contour $\mathcal{C}$ is

$$\Phi_B = -\frac{e}{\hbar}\oint_{\mathcal{C}} \mathbf{A}(\mathbf{r})\cdot d\mathbf{r}. \tag{4.18}$$

For a 2D optical lattice in the tight-binding limit the Hamiltonian can be written as

$$H_{2\mathrm{D}} = -J\sum_{m,n}\left(e^{i\phi^x_{m,n}}\hat{b}^\dagger_{m+1,n}\hat{b}_{m,n} + e^{i\phi^y_{m,n}}\hat{b}^\dagger_{m,n+1}\hat{b}_{m,n} + \mathrm{h.c.}\right), \tag{4.19}$$

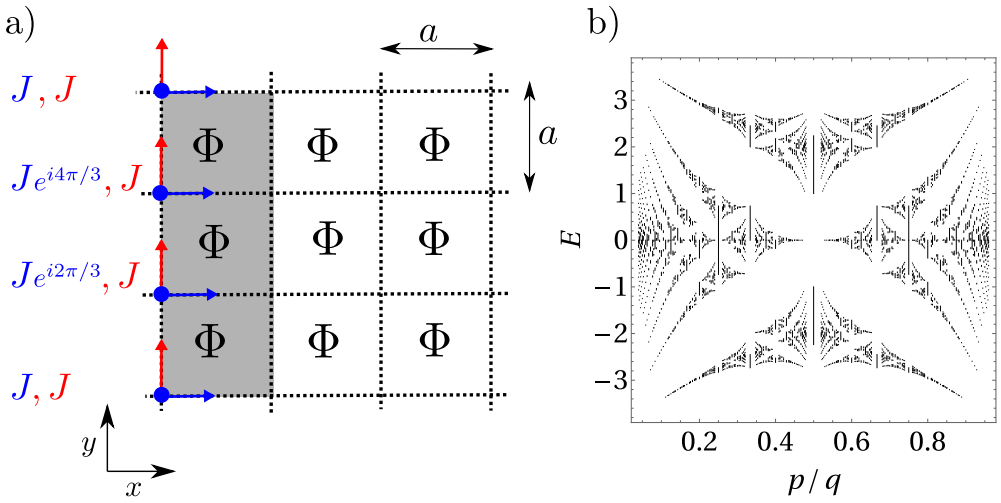

Figure 4.2: a) A 2D lattice in a uniform magnetic field with constant flux Φ for each unit cell. The effective magnetic unit cell is shown for $p/q = 1/3$ as a shaded gray area. The blue and red arrows respectively show the tunneling along the J_x and J_y direction. b) Fractal energy spectrum of the Hofstadter Hamiltonian.

where the phases, $\phi^{x(y)}_{m,n} = -qA^{x(y)}_{m,n}/\hbar$, depend on the vector potential at the links. The total flux piercing one unit cell can then be written in terms of the Peierls phases as

$$\Phi = \phi^{x}_{m,n} + \phi^{y}_{m+1,n} - \phi^{x}_{m,n+1} - \phi^{y}_{m,n}. \tag{4.20}$$

4.4.1 Hofstadter model

The simplest case of a uniform magnetic flux piercing a 2D lattice is known in literature as *Harper-Hofstadter* problem [4.12]. In the Landau gauge $\mathbf{A}(\mathbf{r}) = -By\mathbf{u}_x$, the Peierls phase breaks the transnational invariance along the y direction while preserving the one in the x direction. For rational values of the magnetic flux $\Phi = p/q$ with $p, q \in \mathbb{N}$, the translational invariance is restored along the y direction, if one considers an effective magnetic unit cell enlarged by a factor q along the y-direction. As a consequence the Brillouin zone is also reduced by a factor $1/q$ and the original tight-binding band splits into q sub-bands. An example of the effective magnetic unit cell is given for $p/q = 1/3$ as a gray shaded area in Figure 4.2a. The corresponding complex tunneling amplitude are explicitly written for the same case in blue for the x-direction and red for the y-direction. The energy spectrum as a function of p/q is shown in Figure 4.2b. The spectrum of the Hamiltonian exhibit an interesting fractal structure also known as *Hofstadter butterfly*. For small fluxes $p/q \ll 1$ the energy levels are split into an equidistant set thus retrieving the Landau level structure of a 2D system in free space [4.13].

4.5 Generation of synthetic gauge fields in neutral atoms

The ambition of simulating the physics of a charged particle in an external magnetic field with neutral atoms comes from the desire of reproducing and understanding predicted phenomena that are very difficult to observe in Nature. Electrons confined in a lattice crystal provide an indicative example of the necessity of quantum simulation: a typical lattice constant of the order of few Ångström sets a limit on the flux per unit cell to very small values in solid state systems. The resulting fractal energy structure predicted by Hofstadter thus is virtually impossible to observe. One needs to resort to synthetic artificial magnetic in ultra-cold atoms or superconducting q-bits to fully reproduce and measure the Hofstadter spectrum [4.14].

In the context of neutral cold-atoms, different techniques were developed to simulate artificial gauge fields. A harmonic a-spherical trap rotating close to the trap frequency allows to balance the trapping and centrifugal forces [4.15, 4.16], so that the remaining Coriolis force couples to the velocity field the same way the Lorentz force does for a charged particle. Atom-light interaction provides an alternative tool to generate synthetic geometric phases by either adiabatic following of a dressed state [4.6] or by phase imprinting techniques [4.17]. In this context tuning the wave-length of running wave laser beams in optical lattices revealed to be one of the best tools to generate space-dependent Peierls phases, which result in tunable strong artificial magnetic fields. This technique lead to the observation of the band splitting of the Hofstadter spectrum in Ref. [4.18–4.20], and the observation of the Meissner-vortex transition in isolated ladders [4.21].

Such gauge fields are static and externally prescribed as they solely depend on the external experimental parameters, and are not affected by changes in the atomic configuration. Generating dynamical gauge fields, which would feel the back-action of the atomic dynamics and currents, constitute the next conceptual step for the realization of a genuine gauge theory. The ambitious goal to study strongly interacting lattice gauge theories or exotic anyonic states requires the realization of density-dependent gauge fields. Such dynamical gauge fields can be now realized by employing Floquet engineered systems as proposed in Ref. [4.22]. Three independent experiments were able to simulate dynamical gauge fields in a lattice by imprinting a density dependent Peierls phase in 2019 [4.23–4.25], thus realizing a true $\mathbb{Z}_2$ and $\mathbb{Z}_3$ lattice gauge theory.

Coupling the atomic system to a cavity provides an alternative route for realizing dynamical gauge fields, which exploit the intrinsic non-linearity of the atom-photon interaction in a cavity. We will introduce a few examples of such schemes in the following paragraph.

4.5.1 Cavity-induced gauge potentials

The inability of laser-induced gauge fields to act back on the matter they are coupled to, is based on the static nature of laser-induced gauge potentials. The resulting synthetic electric and magnetic fields do not follow Maxwell's equations and do not exist without the matter to which they are coupled to. Among different approaches adopting light-matter interaction, cavity QED based schemes allow to create gauge field, which dynamically

depend on the state of the atoms. The first theoretical proposal for the realization of cavity-induced gauge potential is reported in Ref. [4.26]. A dispersively coupled atomic ensemble is confined in a quasi-one dimensional ladder and scatters photons into the cavity via two independent Raman transition. In such scheme the atomic wave-function acquires a geometric phase, which is imprinted by two counterpropagating running-wave pump lasers. This phase can be directly tuned by adjusting the ratio between the pump and the cavity wave-vector. When the cavity is empty the tunneling along the cavity direction is suppressed. The emergence of the cavity field restores the hopping along the cavity direction and imprints a phase on the atomic wave-function. The scheme can be easily extended to a 2D lattice [4.27, 4.28] realizing a dynamical Hofstadter model whose spectrum depends on the stationary value of the cavity field amplitude.

While these proposals introduce some coupling between the artificial magnetic field and the atomic state, the gauge potential still acquires a fixed value set by the experimental laser parameters. It therefore still remains a very interesting question, whether is it possible to generate a fully dynamical gauge field, which is not fixed a priori but that would be dynamically affected by the atomic state. On this line, alternative ideas employing cavity-induced directional hopping [4.29] and a multi-mode cavity coupling [4.30] constitute the first attempts to couple neutral atoms to a fully dynamical gauge field.

4.6 Concluding remarks

In this Chapter we briefly introduced the notion of gauge symmetry and the physics of a charged particle coupled to electromagnetic potentials. We discovered that the concept of Aharonov-Bohm phase – or Peierls phases in a lattice – is crucial for the simulation of geometric phases in neutral atoms. We have seen how the coupling to laser fields is indeed a resourceful tool for the simulation of artificial magnetic and electric fields, and we have reviewed some major advances in the experimental quantum simulation of electromagnetism and lattice gauge theories. Finally we highlighted the advantages of realizing dynamical gauge fields in optical cavities, where the emerging magnetic field arises spontaneously along with superradiance.

This Chapter set the basic concepts upon which the publications in Chapters 6 and 7 are based. In particular, in Chapter 6 we will study the dynamical behavior of the energy spectrum of a 2D Fermi gas in a uniform artificial magnetic field. In Chapter 7 we will generalize the system to a multi-mode cavity realizing a fully dynamical model which ultimately will lead to the simulation of a synthetic Faraday's induction law.

5 Antiferromagnetic self-ordering of a Fermi gas in a ring cavity

New Journal of Physics, **21**, 043019 (2019)

Antiferromagnetic self-ordering of a Fermi gas in a ring cavity[†]

Elvia Colella[1], Stefan Ostermann[1], Wolfang Niedenzu[1], Farokh Mivehvar[1] and Helmut Ritsch[1]

[1] *Institut für Theoretische Physik, Universität Innsbruck, Technikerstraße 21a, A-6020 Innsbruck, Austria*

We explore the density and spin self-ordering of driven spin-1/2 collisionless fermionic atoms coupled to the electromagnetic fields of a ring resonator. The two spin states are two-photon Raman-coupled via a pair of degenerate counter-propagating cavity modes and two transverse pump fields. In this one-dimensional configuration the coupled atom-field system possesses a continuous $U(1)$ translational symmetry and a discrete $\mathbf{Z}_2$ spin inversion symmetry. At half filling for sufficiently strong pump strengths, the combined $U(1) \times \mathbf{Z}_2$ symmetry is spontaneously broken at the onset of a superradiant phase transition to a state with self-ordered density and spin structures. We predominately find an antiferromagnetic lattice order at the cavity wavelength. The self-ordered states exhibit unexpected positive momentum pair correlations between fermions with opposite spin. These strong cavity-mediated correlations vanish at higher pump strength.

doi: 10.1088/1367-2630/ab151e

[†]The author of this thesis performed all analytical and numerical calculations presented in this work. Stefan Ostermann provided support in the numerical development of the code. Wolfang Niedenzu and Farokh Mivehvar provided helpful discussion and support in the physical interpretation of the data.

5.1 Introduction

Laser manipulation and control of cold atomic gases has recently seen spectacular advances of experimental technology [5.1] as well as theoretical modelling [5.2–5.5]. In combination with state-of-the-art cavity technology it is now possible to routinely explore the dynamics of degenerate quantum gases in high-Q optical cavities [5.6–5.9]. Numerous intriguing quantum phenomena ranging from spontaneous crystallization to supersolidity or non-trivial magnetic ordering have been predicted and experimentally observed [5.10–5.14]. Although so far experiments have been limited to bosonic atoms with only one or two internal states contributing to the dynamics, experiments using fermionic gases are well in reach and realizable with current technology.

The opto-mechanical coupling of the atom and the cavity fields allows for dynamical trapping of the atoms and even cavity cooling of the gas towards quantum degeneracy [5.15, 5.16]. As a decisive new feature, cavity modes can be designed to introduce tailored long-range interactions [5.17] and dynamic gauge fields for the ultracold atoms [5.18–5.20]. Thus, atom-cavity systems have proven to be a versatile basis for quantum simulations of exotic phases [5.10, 5.21, 5.22] with a wealth of further theoretical proposals still open for implementation [5.23, 5.24]. Generalizations to many field modes and laser frequencies should allow the implementation of fully connected quantum annealing [5.17, 5.25].

With the prediction of new intriguing phenomena such as Umklapp superradiance [5.26, 5.27], topologically protected edge states [5.28, 5.29], superconducting pairing [5.30, 5.31], artificial dynamic gauge fields [5.20], unconventional momentum correlations and quantum

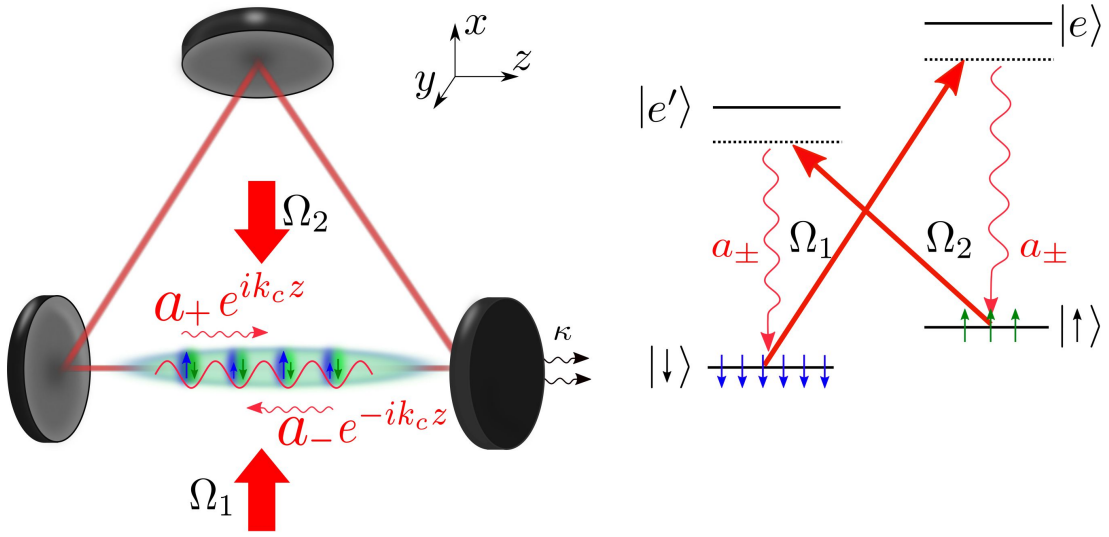

Figure 5.1: Schematic view of the system and the atomic-field coupling. The transitions between two atomic ground states $\{|\uparrow\rangle, |\downarrow\rangle\}$ and two excited states $\{|e'\rangle, |e\rangle\}$ are induced via two far red-detuned lasers with Rabi frequencies $\Omega_{1,2}$ and two cavity field modes with coupling strengths $g_0 e^{\pm ik_c z}$.

phases in multiple dimensions [5.32–5.35], implementations of fermionic systems coupled to cavity fields have gained more attention recently. In the present article, we propose the realization of density and spin self-ordering for a transversely driven multi-level Fermi gas coupled to a pair of counterpropagating degenerate modes of a ring cavity as depicted in Fig. 5.1 [5.36–5.42]. The multi-level atomic structure allows to implement spinor states [5.11], while the cavity geometry guarantees a continuous translational symmetry [5.43, 5.44]. The dynamical coupling between the light fields and the atomic states induces a transversal spin-wave texture of antiferromagnetic nature [5.45]. We show that the common interaction of the atoms with the cavity fields results in the build up of unexpected positive momentum correlations between the atoms.

This paper is organized as follows. In Sec. 5.2 we introduce the model. In Sec. 5.3 we derive the mean-field coupled equations of motion and discuss our numerical approach. We then present the main numerical results and describe the phase diagram of the system in Sec. 5.4A. The superradiance transition threshold is analytically obtained in Sec. 5.4B and the nature of the density and spin self-organized states is further discussed in Sec. 5.4C. Section 5.5 is devoted to analyse the photon-induced momentum correlations between the atoms. Concluding remarks are presented in Sec. 5.6.

5.2 Model

Consider an ensemble of transversely-driven ultracold, fermionic four-level atoms coupled to two modes of a ring cavity as shown in Fig. 5.1. The two atomic ground states $\{|\uparrow\rangle, |\downarrow\rangle\}$ with energies $\{\hbar\omega_\uparrow, \hbar\omega_\downarrow = 0\}$ are coupled to two excited states $\{|e\rangle, |e'\rangle\}$ with energies $\{\hbar\omega_e, \hbar\omega_{e'}\}$ through the interaction with the cavity fields and two external classical pump fields. The energy difference between the two ground states can be tuned by an external longitudinal magnetic field B_z. The atoms are assumed to be strongly confined in the transverse directions, therefore, their motion is restricted along the cavity axis. The ring cavity supports a pair of degenerate counterpropagating modes $\hat{a}_\pm e^{\pm ik_c z}$ with the same linear polarization and frequency ω_c, and opposite wave-numbers $\pm k_c = \pm 2\pi/\lambda_c$. Here, $\hat{a}_+$ ($\hat{a}_-$) is a bosonic field operator annihilating a photon in the forward (backward) propagating cavity mode. The atoms are pumped from the side by two lasers with frequencies $\{\omega_{p1}, \omega_{p2}\}$ and opposite circular polarization, where we have chosen the quantization axis along the cavity axis. The two classical laser fields with Rabi frequencies Ω_1 and Ω_2 drive the transitions $|\downarrow\rangle \leftrightarrow |e\rangle$ and $|\uparrow\rangle \leftrightarrow |e'\rangle$, respectively. Without loss of generality we take both Rabi frequencies to be real. The cavity fields $\hat{a}_\pm$ couple both transitions $|e'\rangle \leftrightarrow |\downarrow\rangle$ and $|e\rangle \leftrightarrow |\uparrow\rangle$, with coupling strengths $g_0 e^{\pm ik_c z}$.

In the limit where the pumps and cavity fields are far detuned from the atomic excited states $|e\rangle$ and $|e'\rangle$, only virtual excitations are created and the system can be effectively described as a spin-1/2 system $\{|\downarrow\rangle, |\uparrow\rangle\}$. As discussed in 5.A, this system is described

by the effective time-independent Hamiltonian

$$H = \sum_{\sigma\in\{\uparrow,\downarrow\}} \int dz\ \hat{\Psi}^\dagger_\sigma(z)\Big[-\frac{\hbar^2}{2m}\frac{d^2}{dz^2} + \hbar\delta_\sigma + \hat{U}_\sigma(z)\Big]\hat{\Psi}_\sigma(z)$$
$$+ \int dz\ \hbar\hat{\eta}_R(z)\ \Big[\hat{\Psi}^\dagger_\uparrow(z)\hat{\Psi}_\downarrow(z) + \hat{\Psi}^\dagger_\downarrow(z)\hat{\Psi}_\uparrow(z)\Big]$$
$$- \hbar\Delta_c(\hat{a}^\dagger_+\hat{a}_+ + \hat{a}^\dagger_-\hat{a}_-), \tag{5.1}$$

where $\hat{\Psi}_\sigma(z)$ are fermionic field operators fulfilling the anti-commutation relation

$$\{\hat{\Psi}_\sigma(z), \hat{\Psi}^\dagger_{\sigma'}(z')\} = \delta(z-z')\delta_{\sigma,\sigma'}. \tag{5.2}$$

The effective detunings between the two spin states and the pump fields are denoted as $\delta_\downarrow = 0$ and $\delta_\uparrow = \omega_\uparrow + B_z - (\omega_{p2} - \omega_{p1})/2$, respectively. That is, $\hbar\delta \equiv \hbar(\delta_\uparrow - \delta_\downarrow)$ defines the effective energy splitting between the two spin states.

In this model photons interact with atoms via two fundamental mechanisms. The scattering of photons by the atoms between the two cavity modes $\hat{a}_\pm$ induces a potential with $\lambda_c/2$ periodicity,

$$\hat{U}_\sigma(z) = U_{0\sigma}(\hat{a}^\dagger_+\hat{a}_+ + \hat{a}^\dagger_-\hat{a}_- + e^{-i2k_cz}\hat{a}^\dagger_+\hat{a}_- + e^{i2k_cz}\hat{a}^\dagger_-\hat{a}_+), \tag{5.3}$$

with $U_{0\uparrow} = \hbar g_0^2/\Delta_e$ and $U_{0\downarrow} = \hbar g_0^2/\Delta_{e'}$, where $\Delta_e = (\omega_{p1}+\omega_{p2})/2-\omega_e$ and $\Delta_{e'} = \omega_{p1}-\omega_{e'}$. On the other hand, scattering of photons from the pumps into the cavity modes by the atoms results in spin flipping processes with $\pm\hbar k_c$ momentum kicks to the atoms described by the λ_c-periodic Raman coupling term

$$\hat{\eta}_R(z) = \eta(\hat{a}_+e^{ik_cz} + \hat{a}_-e^{-ik_cz} + \hat{a}^\dagger_+e^{-ik_cz} + \hat{a}^\dagger_-e^{ik_cz}). \tag{5.4}$$

We have considered the balanced Raman coupling configuration $\eta \equiv \Omega_1 g_0/\Delta_e = \Omega_2 g_0/\Delta_{e'}$, where η is the two-photon Rabi frequency.

The last line in the Hamiltonian (5.1) represents the energy contribution of the two cavity modes $\hat{a}_\pm$, where the cavity detuning is $\Delta_c = (\omega_{p1} + \omega_{p2})/2 - \omega_c$. Cavity losses will be phenomenologically included in the equations of motion for the field operators $\hat{a}_\pm$ via the cavity decay rate κ [5.46]. Note that contact two-body interactions between atoms are assumed to be negligible throughout this work.

The processes acting on the spin and the density degrees of freedom are characterized by competing periodicity. The periodic potentials $\hat{U}_\sigma(z)$ [Eq. (5.3)] favour the organization of the atoms in a $\lambda_c/2$-periodic structure. By contrast, the position dependent Raman coupling $\hat{\eta}_R(z)$ [Eq. (5.4)] favours a spin texture with λ_c periodicity. Therefore, the Raman coupling term defines the periodicity of the Hamiltonian and the size of the Brillouin zone $[-k_c/2, k_c/2]$.

The Hamiltonian (5.1) is invariant under the parity transformation of the photonic operators $\hat{a}_\pm \to -\hat{a}_\pm$ and the π-rotation of the local transverse spin of the system $\hat{S}_x(z) \to -\hat{S}_x(z)$ and $\hat{S}_y(z) \to -\hat{S}_y(z)$. Here, the total local spin operator is defined as

$$\hat{\mathbf{S}}(z) = \Big(\hat{\Psi}^\dagger_\uparrow(z), \hat{\Psi}^\dagger_\downarrow(z)\Big)\,\boldsymbol{\tau}\begin{pmatrix}\hat{\Psi}_\uparrow(z)\\ \hat{\Psi}_\downarrow(z)\end{pmatrix}, \tag{5.5}$$

where $\boldsymbol{\tau} = (\tau_x, \tau_y, \tau_z)$ is the vector of the Pauli matrices. The combination of parity and spin inversion yields a discrete $\mathbf{Z}_2$ symmetry. In addition, the Hamiltonian (5.1) is invariant under the simultaneous transformations $z \to z + \Delta z$ and $\hat{a}_\pm \to \hat{a}_\pm e^{\mp i k_c \Delta z}$, yielding a continuous $U(1)$ symmetry. Any arbitrary displacement of the position of the atom can be compensated by a phase shift of the photonic operators. This continuous $U(1)$ symmetry is a specific character of the ring cavity geometry [5.47]. In fact, in a ring cavity the intensity maxima of the cavity fields can sit at any position on the cavity axis, realizing a continuous translational symmetry. This is in sharp contrast to linear cavities where the cavity fields must have a node on the mirrors to satisfy the boundary conditions, giving rise to a discrete $\mathbf{Z}_2$ symmetry [5.28].

Therefore, the Hamiltonian (5.1) possesses a $U(1) \times \mathbf{Z}_2$ symmetry, which is spontaneously broken at the onset of the superradiant phase transition with the emergence of a self-organized density and spin texture, as will be shown in the following. In contrast to single component quantum gases [5.48, 5.49], where the phase transition is driven by a density order parameter, here the spin self-organization plays the fundamental role in the superradiant process [5.23, 5.50, 5.51]. In other words, the cavity modes can only be populated for a non-vanishing spin order parameter.

5.3 Self-consistent mean-field method

In order to determine the steady state of the system we employ a self-consistent mean-field method. The atomic state is dynamically coupled to the cavity-photon dynamics, see 5.B. The large cavity detuning $|\Delta_c|$ and cavity linewidth 2κ dictate a fast dynamical evolution of the cavity fields, which at each moment adiabatically follows the atomic state [5.52]. On the other hand, the fermionic dynamics evolve in the self-consistent potentials and the Raman field created by the cavity modes (and pump lasers). At a given value of the cavity fields $\langle \hat{a}_\pm \rangle = \alpha_\pm$, the atomic dynamics can be described by a single-particle Hamiltonian. Upon making a Bloch ansatz for the single-particle wave function $\psi_{nq\sigma}(z) = e^{iqz} u_{nq\sigma}(z)$ [5.53], the atomic field operators can be expanded in the basis of the Bloch functions,

$$\hat{\Psi}_\sigma(z) = \sum_{n,q} \psi_{nq\sigma}(z) \hat{c}_{nq}. \tag{5.6}$$

Here $\hat{c}_{nq}$ is a fermionic operator which annihilates a particle in the nth band with quasi-momentum q and $u_{nq\sigma}(z)$ are λ_c-periodic functions. Therefore, the single particle problem is solved by diagonalizing the Hamiltonian within one unit cell $[0, \lambda_c = 2\pi/k_c]$ with periodic boundary conditions. We aim to determine the eigenvalues ϵ_{nq} of the coupled Schrödinger equations for the functions $u_{nq\uparrow}(z)$ and $u_{nq\downarrow}(z)$,

$$\Big[\frac{\hbar^2}{2m}\Big(i\frac{d}{dz} - q\Big)^2 + \hbar\delta_\uparrow + U_\uparrow(z)\Big] u_{nq\uparrow}(z) + \hbar\eta_R(z) u_{nq\downarrow}(z) = \epsilon_{nq} u_{nq\uparrow}(z), \tag{5.7a}$$

$$\Big[\frac{\hbar^2}{2m}\Big(i\frac{d}{dz} - q\Big)^2 + \hbar\delta_\downarrow + U_\downarrow(z)\Big] u_{nq\downarrow}(z) + \hbar\eta_R(z) u_{nq\uparrow}(z) = \epsilon_{nq} u_{nq\downarrow}(z), \tag{5.7b}$$

where the quasi-momentum q lies in the first Brillouin zone, $q \in [-k_c/2, k_c/2]$.

The chemical potential μ of the system has to be determined self-consistently by fixing the total number of particles

$$N = \sum_{\sigma} \int_0^L dz\; n_\sigma(z), \tag{5.8}$$

where

$$n_\sigma(z) = \sum_{nq} |u_{nq\sigma}(z)|^2 n_F(\epsilon_{nq}) \tag{5.9}$$

is the local atomic density in the σ-spin state with $n_F(\epsilon) = 1/[1 + e^{(\epsilon-\mu)/k_B T}]$ being the Fermi distribution. We assume thermal equilibrium between the two spin states and therefore use the same chemical potential μ for both states throughout the calculation.

Equations (5.7) are solved in a self-consistent way in combination with the stationary values of the cavity fields $\alpha_\pm$. As discussed in 5.B, the stationary field amplitudes are given by

$$\alpha_+ = \frac{2\eta(\tilde{\Delta}_c + i\kappa)}{(\tilde{\Delta}_c + i\kappa)^2 - U_0^2|\mathcal{N}_{2k_c}|^2}\Big(\Theta^* + \frac{U_0 \mathcal{N}^*_{2k_c}}{\tilde{\Delta}_c + i\kappa}\Theta\Big), \tag{5.10a}$$

$$\alpha_- = \frac{2\eta(\tilde{\Delta}_c + i\kappa)}{(\tilde{\Delta}_c + i\kappa)^2 - U_0^2|\mathcal{N}_{2k_c}|^2}\Big(\Theta + \frac{U_0 \mathcal{N}_{2k_c}}{\tilde{\Delta}_c + i\kappa}\Theta^*\Big). \tag{5.10b}$$

Here we have defined the effective shifted cavity detuning $\tilde{\Delta}_c = \Delta_c - U_0 N$ and the atomic averages

$$\mathcal{N}_{2k_c} = \int dz e^{2ik_c z} n(z), \tag{5.11}$$

and

$$\Theta = \int dz e^{ik_c z} S_x(z), \tag{5.12}$$

where Θ is the spin order parameter driving the superradiant phase transition. Indeed, a non-vanishing Θ is required for non-zero cavity fields in Eqs. (5.10). Here,

$$n(z) = n_\uparrow(z) + n_\downarrow(z) \tag{5.13}$$

is the total atomic density and

$$S_x(z) = \frac{1}{2}\sum_{q,n}\Big[u^*_{nq\uparrow}(z)u_{nq\downarrow}(z) + u^*_{nq\downarrow}(z)u_{nq\uparrow}(z)\Big]n_F(\epsilon_{qn}) \tag{5.14}$$

is the average local spin component in the x-direction. These atomic averages can also be interpreted as the probabilities of photon-atom scattering processes. In fact, $\mathcal{N}_{2k_c}$ is the probability that an atom absorbs a photon and then re-emits it in the opposite direction receiving a $2\hbar k_c$ momentum kick without changing its internal state. On the other hand, Θ is the probability of scattering a photon from a pump laser into a cavity mode where the atom changes both its internal and external states, with a momentum exchange of $\hbar k_c$.

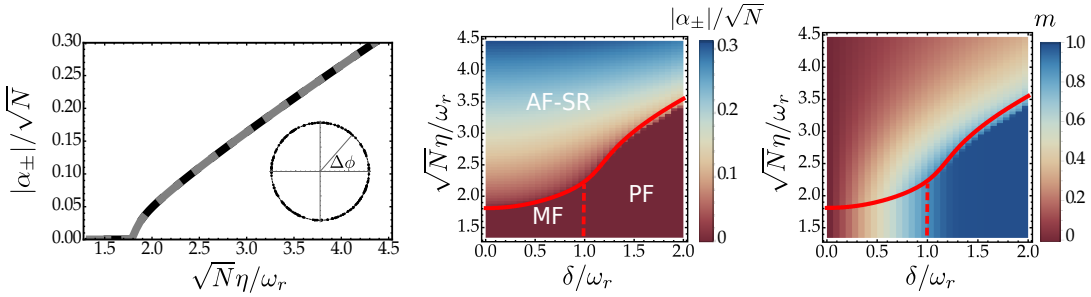

Figure 5.2: (a) Intra-cavity amplitudes of the two modes α_+ (α_-) as a function of the rescaled pump strength $\sqrt{N}\eta/\omega_r$ for the effective energy splitting $\delta = 0$ shown as grey (dashed black) curves. Inset: relative phase $\Delta\phi = \phi_+ - \phi_-$ of the two modes for 200 realizations demonstrating the $U(1)$ symmetry breaking. Parameters: $\{\delta, \sqrt{N}\eta\} = \{0, 2.7\}\omega_r$. (b) Phase diagram of the system. The color encodes the amplitudes $|\alpha_\pm|/\sqrt{N}$ of the fields. Below threshold, the system can be either a mixed Fermi (MF) gas or a polarized Fermi (PF) gas, separated by a dashed red line. Above threshold, we find a superradiant state with antiferromagnetic character (AF-SR). The red solid line is the analytical result (5.19) for the critical pump strength. (c) Global longitudinal magnetization (5.15) of the system. Cavity parameters: $\{\Delta_c, \kappa, U_0 N\} = \{-20, 10, -8\}\omega_r$.

5.4 Superradiant phase transition

In the following, we characterize the phase diagram of a Fermi gas at fixed density, $k_F/k_c = 1/2$, i.e., half filling, with k_F being the Fermi momentum. The single-particle Hamiltonian is diagonalized within one unit cell with periodic boundary condition and fifty quasi-momenta q (equivalent to a lattice of $N_c = 50$ sites) at finite temperature $k_B T = 0.05\hbar\omega_r = 0.2 k_B T_F$. Here, T_F is the Fermi temperature, defined as $k_B T_F = \hbar^2 k_F^2/2m$, and $\omega_r = \hbar k_c^2/2m$ is the recoil frequency. The cavity is red detuned, $\Delta_c = -20\omega_r$. The presence of the Fermi gas induces a shift of the cavity frequency proportional to the refractive index, $U_0 N = -8\omega_r$. For a fixed value of the refractive index, the effective shifted cavity detuning $\tilde{\Delta}_c = \Delta_c - U_0 N = -12\omega_r$ is still in the red detuned regime. The cavity linewidth is chosen as $\kappa = 10\omega_r$.

5.4.1 Phase diagram

In Fig. 5.2(a) we show the amplitudes $|\alpha_\pm|/\sqrt{N}$ of the two cavity fields as a function of the rescaled pump strength $\sqrt{N}\eta/\omega_r$ for the degenerate case, where the effective level splitting vanishes, $\delta = 0$. In our mean-field picture, in the superradiant phase the cavity fields are coherent states, $\langle \hat{a}_\pm \rangle = \alpha_\pm = |\alpha_\pm| e^{i\phi_\pm}$. The two modes are symmetrically coupled to the two atomic transitions and hence are equally populated. Their amplitudes

grow monotonically across the transition point, hinting to the occurrence of a second order phase transition. Above threshold the field amplitudes scale as $\sim \eta^{3/2}$ which differs from the $\sim \eta^{1/2}$ power law exponent found in conventional self-organization in standing-wave cavities [5.54, 5.55]. The phase difference of the two modes, $\Delta\phi = \phi_+ - \phi_-$, can acquire any value between 0 and 2π as shown in the inset of Fig. 5.2(a), where the relative phase of the two fields is shown for 200 realizations at fixed parameters. The relative phase uniformly distributes on a circle, demonstrating the continuous $U(1)$ symmetry breaking. This implies that the minima of the optical potential generated by the interference of the two cavity modes can be located anywhere within one unit cell. The translational symmetry is therefore connected with the relative phase of the two modes and the system possesses a full $U(1)$ symmetry.

In Fig. 5.2(b) the amplitudes of the two modes are shown as a function of the effective level splitting δ/ω_r and the rescaled pump strength $\sqrt{N}\eta/\omega_r$. At each fixed δ the transition to the superradiant state, indicated by the solid red line, is of second order. Note that the critical threshold grows with increasing atomic energy spacing δ. In Fig. 5.2(c) we show the global magnetization

$$m = \frac{N_\uparrow - N_\downarrow}{N}, \tag{5.15}$$

of the atomic gas in the same parameter space, where $N_\sigma = \int_0^L dz n_\sigma(z)$. Below the superradiant transition threshold the Fermi gas is in a trivial phase where the population imbalance is governed by the energy difference δ between the two spin states. In fact, this parameter acts as an effective longitudinal magnetic field, orienting the spin of the particles in its direction. For $\delta = 0$ the system is not magnetized, $m = 0$. With increasing δ, an increasing amount of atoms align with the effective magnetic field and the system is an incoherent mixed Fermi (MF) gas, $0 < m < 1$. The mixed phase is arising from the incoherent superposition of the atoms in the two spin states. It is a direct result of the thermalization of the atoms in the Zeeman sub-levels. The studied system can thermalize via two-body contact interactions, incoherent decay or Raman transitions induced by thermal photons or vacuum fluctuations. For $\delta > \omega_r$ all particles are aligned in the same direction and the system becomes a polarized Fermi (PF) gas with $m = 1$. In the superradiant regime, the magnetization of the system gradually decreases, evolving towards an ordered state of antiferromagnetic character with zero magnetization $m = 0$, which exhibits superradiant photon scattering (AF-SR).

5.4.2 Transition threshold

Due to the continuous change of the order parameters $\alpha_\pm$ across the critical point, the superradiant phase transitions can be described within the framework of the Landau theory of second-order phase transitions [5.56]. The transition threshold can be obtained by expanding the free energy in powers of the order parameter and requiring that the coefficient of the second order term vanishes at the critical point. Integrating out fermionic degrees of freedom [5.27, 5.50, 5.51], the free energy as a functional of the cavity-field

order parameters $\alpha_\pm$ is expressed as

$$F[\alpha_\pm^*, \alpha_\pm] = -\tilde{\Delta}_c \left(|\alpha_-|^2 + |\alpha_+|^2\right) - \eta^2 N \chi_m |\alpha_+^* + \alpha_-|^2. \tag{5.16}$$

Here only terms up to second order in $\alpha_\pm$ are retained and

$$\chi_m = \sum_k \frac{n_F(\epsilon_{k+k_c\uparrow}) - n_F(\epsilon_{k\downarrow})}{\epsilon_{k\downarrow} - \epsilon_{k+k_c\uparrow}} \tag{5.17}$$

is the magnetic susceptibility of the Fermi gas, where $\epsilon_{k\uparrow} = \hbar^2 k^2/2m - \mu + \delta$ and $\epsilon_{k\downarrow} = \hbar^2 k^2/2m - \mu$ are the bare energies of the two fermionic spins before the transition.

We express the free energy as a functional of the atomic order parameter Θ using Eq. (5.10). In a first-order approximation we neglect the contribution of the mixing of the two cavity fields due to scattering processes which stem from the optical potentials $U_\sigma(z)$. This approximation is well justified in our parameter regime $U_0|\mathcal{N}_{2k_c}|/\tilde{\Delta}_c \ll U_0 N/\tilde{\Delta}_c \sim 1$ at the onset of the phase transition. The quadratic free energy in terms of the atomic order parameter therefore takes the form

$$F[\Theta^*, \Theta] \sim \left(1 - \frac{\eta^2}{\eta_c^2}\right)|\Theta|^2, \tag{5.18}$$

where

$$\sqrt{N}\eta_c = \sqrt{\frac{\tilde{\Delta}_c^2 + \kappa^2}{2\tilde{\Delta}_c \chi_m}} \tag{5.19}$$

is the critical pump strength, which depends on the cavity parameters $\tilde{\Delta}_c$ and κ and on the magnetic susceptibility χ_m. At zero temperature and for the degenerate case $\delta = 0$, the divergence of χ_m leads to a strong suppression of the transition threshold. In fact, the scattering of a photon from the pump into the cavity by an atom results in a $k_c = 2k_F$ momentum transfer, causing the atom to scatter from one side of the Fermi surface to the other. This process requires nearly no energy cost and leads to a vanishing critical pump strength at $T = 0$. In order for this to occur, the nesting condition $k_c = 2k_F$ must be satisfied, in analogy to polarized fermions in linear cavities [5.26–5.28, 5.34]. A finite temperature washes out the divergence of the magnetic susceptibility, resulting in a finite, although small threshold. In analogy to the one component case, superradiance should be robust against thermal fluctuations. At high temperature, the atomic system can be described as a classical gas following the Boltzmann statistics. An expansion of Eq. (5.19) for high temperatures reveals a $T^{1/2}$ scaling of the transition threshold. For sufficiently high pump strengths, this should still allow to observe the transition to the magnetic state. In addition, the presence of a finite energy splitting δ shifts the nesting wave-vector, resulting in an increase of the critical threshold in comparison to $\delta = 0$, where the nesting condition perfectly holds. Similarly deviations from the nesting condition, due to trapping inhomogeneities or the incommensurability between the cavity wave-vector and the Fermi momentum, increase the critical threshold but preserve superradiance, as it is shown in 5.C. The critical threshold (5.19) is shown in

Figs. 5.2(b) and 5.2(c) as a red solid curve separating the superradiant regime from the trivial phase. The analytic threshold is consistent with the numerical result. Small deviations from the theoretical prediction for big level spacing δ can be attributed to neglected terms scaling with $U_0|\mathcal{N}_{2k_c}|/\tilde{\Delta}_c$ in the analytic calculation.

5.4.3 Self-organization

In Fig. 5.3 we illustrate the structure of the Fermi gas in the superradiant phase by analysing the behaviour of the local density and spin of the system. Figure 5.3(a) illustrates the local spin vector $\langle\hat{\mathbf{S}}\rangle$ [cf. Eq. (5.5)] as a function of the position along the cavity axis within one unit cell. The individual $S_x(z)$ and $S_z(z)$ components are shown in Fig. 5.3(b). Note that the spin of the system always lies in the $\{S_x, S_z\}$ plane, i.e., $S_y(z) = 0$. A non-vanishing $S_z(z)$ component is induced by the effective energy spacing δ acting as an effective longitudinal magnetic field. In addition, the Raman coupling acts as a transversal magnetic field in the x-direction, which adiabatically drives the $S_x(z)$ spin component [5.3]. The optical potential $U_\sigma(z)$ favors a $\lambda_c/2$-periodic density pattern, as shown in Fig. 5.3(c).

For intermediate pump strengths, the system is weakly self-organized and the spin texture is characterized by the presence of a transversal λ_c-periodic spin wave in the x-direction, $S_x(z)$, and a longitudinal $\lambda_c/2$-periodic spin wave in the z-direction, $S_z(z)$, see Fig. 5.3(b). The $S_x(z)$ component spontaneously emerges from the interference of two counterpropagating photon-induced spin waves. The phenomenon has common features with itinerant antiferromagnetism in Chromium and Chromium alloys [5.57–5.59]. At very high pump strengths, the system is strongly self-organized and gradually evolves toward an antiferromagnetic state in a more conventional sense. The corresponding state arises from the freezing of the spin degrees of freedom, which would result in a reduced entropy per particle in the self-organized state. The global magnetization drops to zero (see Fig. 5.2(c)) and the $S_z(z)$ component becomes negligible. In this regime the optical potentials $U_\sigma(z)$ localize the atoms, resulting in the emergence of a λ_c-periodic antiferromagnetic lattice order similar to bosonic atoms inside linear cavities [5.3, 5.23].

The position of the density peaks within the unit cell is arbitrarily chosen, indicating the spontaneous $U(1)$ symmetry breaking. However, for a given density configuration, the ground state is twofold degenerate. In Fig. 5.3(a) we show the two degenerate spin textures (black and red). The $\mathbf{Z}_2$ symmetry breaking corresponds to the realization of one of the two possible spin textures.

The spin and density structures induce a metal-insulator transition which can be observed in the appearance of a gap in the atomic band structure. In Fig. 5.4, we show the band structure for different δ both in the superradiant regime (solid curves) and below threshold (dashed curves). The spin gap can open at any quasimomentum q, where the original $|\uparrow\rangle$ and $|\downarrow\rangle$ bands cross each other. In particular, at $\delta = 0$, where the two states $\{|\uparrow\rangle, |\downarrow\rangle\}$ are degenerate, the gap opens at the edges of the Brillouin zone $q = \pm k_c/2$. Increasing δ the gap opening gradually shifts toward zero until reaching the critical value $\delta = \omega_r$. In fact, by increasing the effective spin energy spacing the bands of the two states are gradually pushed apart, until for $\delta = \omega_r$ the $|\downarrow\rangle$ states becomes energetically

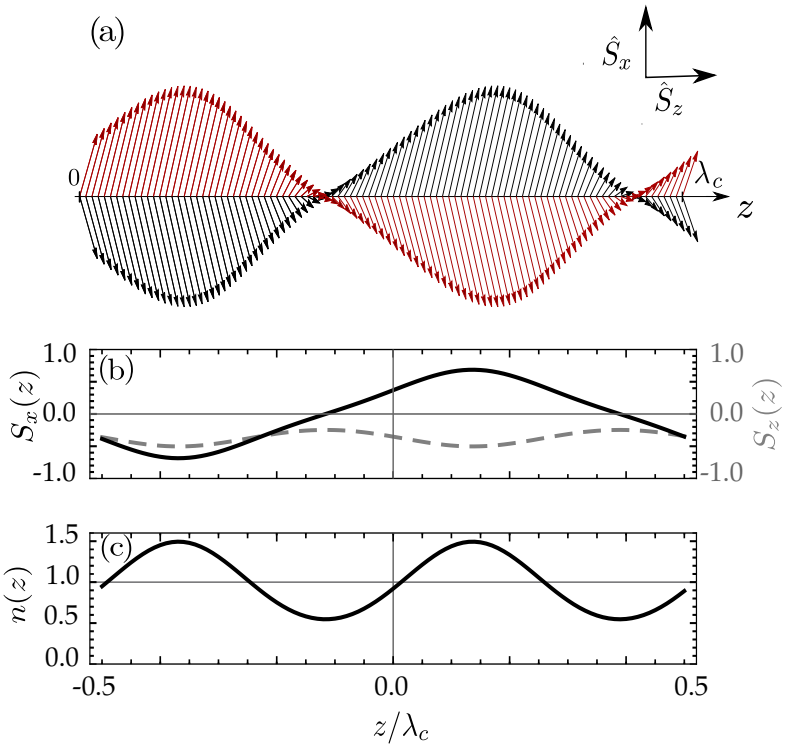

Figure 5.3: Atomic structure above threshold, $\eta > \eta_c$. (a) Spin texture within one unit cell $[0, \lambda_c]$ in the $\{S_x, S_z\}$ plane: note that $S_y(z) = 0$. The two possible spin textures are shown in black and red for a given density configuration, exhibiting the $\mathbf{Z}_2$ symmetry of the system as described in the main text. (b) Individual local spin components $S_x(z)$ and $S_z(z)$, and (c) total atomic density distribution $n(z) = n_\uparrow(z) + n_\downarrow(z)$. Parameters: $\sqrt{N}\eta = 2.7\omega_r$ and $\delta = 0.6\omega_r$. Other parameters as in Fig. 5.2.

more favourable and the system becomes fully polarized. For $\delta > \omega_r$ the spin gap opens between higher bands. However, the presence of the self-consistent optical lattices $U_\sigma(z)$ favours the opening of a density gap at $q = 0$, which preserves the insulating state.

5.5 Momentum correlations

Studies of momentum correlations between two particles in ring cavities revealed a strong coupling between the light fields and the atomic motion [5.60, 5.61]. In particular, while classical particles show a strong damping of the center-of-mass motion and anticorrelated momenta, quantum particles tend to correlate their motion [5.61]. Quantum simulations of particles with Fermi or Bose statistics show momentum anticorrelation and correlation, respectively [5.16]. The momentum correlation coefficient for two atoms in spin states σ_1

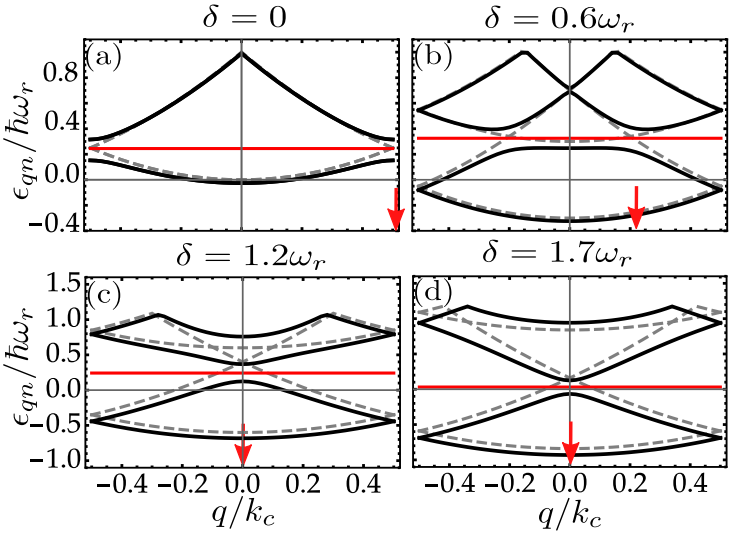

Figure 5.4: Atomic band structure both below threshold (dashed gray) and above the ordering transition (black solid). The position of the chemical potential (red line) indicates a metal-insulator transition. The red arrows show the quasimomentum q at which the insulating gap opens. The energy splitting is (a) $\delta = 0\omega_r$, (b) $\delta = 0.6\omega_r$, (c) $\delta = 1.2\omega_r$ and (d) $\delta = 1.7\omega_r$.

and σ_2 is defined as

$$\mathcal{C}_{\sigma_1\sigma_2} = \frac{\langle k_1 k_2\rangle_{\sigma_1\sigma_2} - \langle k_1\rangle_{\sigma_1}\langle k_2\rangle_{\sigma_2}}{\Delta k_1 \Delta k_2}, \tag{5.20}$$

where $\mathcal{C}_{\sigma_1\sigma_2} = 1$ ($\mathcal{C}_{\sigma_1\sigma_2} = -1$) indicates perfect correlation (anticorrelation) between the two particle momenta. The expectation values in Eq. (5.20) read

$$\langle k_1 k_2\rangle_{\sigma_1\sigma_2} = \iint \mathrm{d}k_1 \mathrm{d}k_2\, k_1 k_2\, \rho_2(k_1,\sigma_1;k_2,\sigma_2), \tag{5.21a}$$

$$\langle k_1\rangle_{\sigma_1} = \int \mathrm{d}k_1\, k_1\, \rho_1(k_1\sigma_1), \tag{5.21b}$$

where $\rho_2(k_1,\sigma_1;k_2,\sigma_2)$ is the two-body density matrix in momentum space and $\rho_1(k_1,\sigma_1)$ is the one-body density matrix.

In Fig. 5.5(a), we show the momentum correlation coefficient (5.20) for increasing pump strength for the degenerate case $\delta = 0$ (the results do not change qualitatively for finite level splitting). Below threshold, particles with the same spin (black and grey curves in Fig. 5.5(a)) show perfectly anticorrelated momenta, $\mathcal{C}_{\uparrow\uparrow} = \mathcal{C}_{\downarrow\downarrow} = -1$. However, as the threshold is surpassed by increasing the pump strength, the two-photon scattering with $\pm 2k_c$ momentum transfer enhance the correlations between comoving particles with the same spin, eventually leading to uncorrelated momenta.

By contrast, the momenta of particles in opposite spin states (blue curve in Fig. 5.5(a)) are uncorrelated below threshold, $\mathcal{C}_{\uparrow\downarrow} = \mathcal{C}_{\downarrow\uparrow} = 0$. In the superradiant regime, however, the

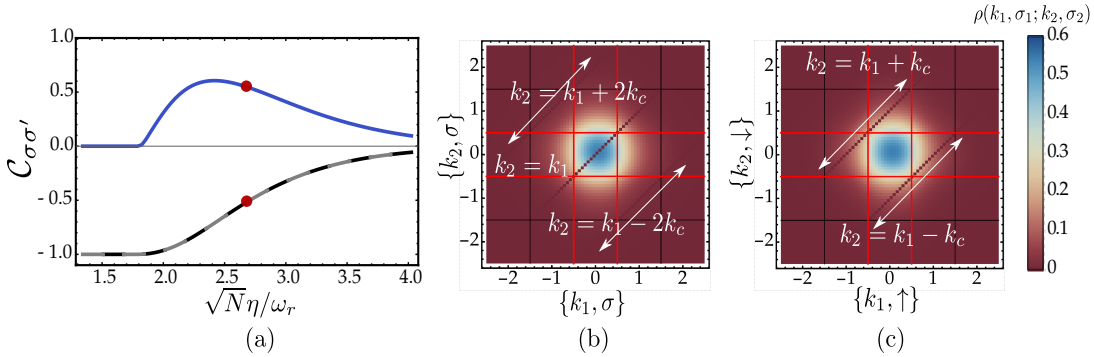

Figure 5.5: (a) Correlation coefficient for the same (gray and dashed black) and opposite spin directions (blue) as a function of the rescaled pump strength $\sqrt{N}\eta/\omega_r$ at the effective energy splitting $\delta = 0$. The red dot represents the pump value for which the two-body density matrix is shown. The two-body density matrix $\rho(k_1, \sigma_1; k_2, \sigma_2)$ in momentum space for $\delta = 0$ and $\sqrt{N}\eta = 2.7\omega_r$ for particles with (b) the same spin and (c) opposite spins. The red lines show the position of the Fermi surface below transition, $k_F = 1/2k_c$. The thermal background strongly deviates from the trivial phase, evolving from a perfect square below the threshold to a smooth circle above η_c. The interaction between cavity photons and fermions is responsible for the appearance of the off-diagonal dips at $k_1 = k_2 \pm k_c$ and $k_1 = k_2 \pm 2k_c$. The white arrows are guides to the eye for emphasising the off-diagonal dips.

scattering processes from the pumps to the cavity induce unexpected positive correlations. These positive correlations saturate for intermediate pump strengths and vanish in the limit of very strong pump strengths.

The behaviour of the correlation coefficient $\mathcal{C}_{\sigma_1\sigma_2}$ in Fig. 5.5(a) can be understood from the two-body density matrix in momentum space, shown in Figs. 5.5(b) and 5.5(c). There, the thermal background is visible as a smooth circle extending outside the Fermi surface below threshold ($\pm k_F$), indicated by the red lines. In the superradiant phase the scattering of photons by the atoms leads to the population of higher momentum states. Hence, the momentum distribution loses its sharpness and acquires tails at higher momenta which are responsible for the observed shape. In addition, forbidden states revealed by the dips along the diagonal, $k_2 = k_1$, and the shifted diagonals, $k_2 = k_1 \pm 2k_c$, appear in the two-body density matrix with the same spin, see Fig. 5.5(b). Likewise, for particles with opposite spins dips at $k_2 = k_1 \pm k_c$ develop (Fig. 5.5(c)).

These diagonal dips can be understood as a consequence of the Pauli principle for fermions in a ring cavity. The Pauli principle forbids particles with the same spin to occupy the same momentum state, which explains the diagonal dip $k_2 = k_1$ in Fig. 5.5(b). The off-diagonal dips are then a manifestation of the Pauli principle at higher momenta, indicating the absence of two-particle states that cannot be created via

the interaction with the cavity photons because the required initial state is prohibited by the fermionic statistics. Since the state $|k_1, \sigma_1; k_2 = k_1, \sigma_2 = \sigma_1\rangle$ is forbidden by the Pauli principle, the Hamiltonian (5.1) cannot populate states with opposite spins and momenta $k_2 = k_1 \pm k_c$ or same spin and momenta $k_2 = k_1 \pm 2k_c$. The propagation of the Pauli principle to higher momenta then forbids states with the same spin and momenta differing by even multiples of the cavity wave-vector, $|k_1, \sigma_1; k_2 = k_1 \pm 2jk_c, \sigma_2 = \sigma_1\rangle$ ($j \in \mathbb{N}_0$), and states with opposite spin and momenta differing by odd multiples of k_c, $|k_1, \sigma_1; k_2 = k_1 \pm (2j+1)k_c, \sigma_2 = -\sigma_1\rangle$. These higher-order dips become visible as the momentum distribution broadens in momentum space.

For intermediate pump strengths above threshold the thermal background only moderately surpasses the $T = 0$ Fermi surface. The forbidden states, i.e., the overlap of the off-diagonal dips with the thermal background, then mainly consist of counterpropagating pairs. This leads to an excess of co-moving particles in the Fermi gas, which causes an increase of the momentum correlation coefficient (5.20) above threshold, both for particles having the same or opposite spin (Fig. 5.5(a)). However, the correlations increase faster for particles having opposite spin than for particles in the same spin state, since for the former the first off-diagonal forbidden states pertain to smaller momenta ($k_2 = k_1 \pm k_c$) than for the latter ($k_2 = k_1 \pm 2k_c$). With increasing pump strength, however, the momentum distribution broadens and the off-diagonal dips include a balanced contribution of both counterpropagating and co-moving pairs, leading to a decrease in correlation and eventually to uncorrelated particle momenta, $\mathcal{C}_{\uparrow\downarrow} = 0$, far above threshold.

5.6 Conclusion and Outlook

We explored the self-ordering of a fermionic gas coupled to the light fields of a tranversally-pumped ring resonator. The system is characterized by a continuous $U(1)$ translational symmetry and a disc rete $\mathbf{Z}_2$ spin inversion symmetry. The combined $U(1) \times \mathbf{Z}_2$ symmetry is spontaneously broken at the onset of a superradiant phase transition where the cavity modes become macroscopically populated. Above the transition threshold the atomic gas self-organizes in an state with antiferromagnetic character with spontaneously emerging density and spin waves. On a mean-field level, a very similar phase diagram could be realized for bosonic species. The effect of the quantum statistics is fundamental for low photon numbers where the mean-field approximation breaks down, which gives rise to new phases [5.32]. Within our level of approximation the essential signature of the Fermi statistics is found in the two-body momentum correlations.

In fact, cavity photons mediate strong cooperative effects between the atomic motion and the internal atomic dynamics. We accordingly observed strong correlations in momentum space: atoms in the same spin state show anticorrelation while atoms with opposite spin are characterized by unexpected positive correlations. Such correlations can be traced back to the propagation of the Pauli principle to higher momenta through the interaction with the cavity modes. Their nature is therefore a direct consequence of the fermionic statistics and can lead to the generation of strongly entangled states [5.62].

In conclusion, our system allows to explore a wealth of novel and interesting phenomena

where the light fields are dynamically coupled to the atomic state. Such systems represent an optimal platform for the study of strongly correlated systems in many-body physics and condensed matter. In particular, the possibility of inducing a BCS-type pairing [5.63–5.65] with cold atoms in optical cavities paves the way to the realization of light-induced superconductivity under controllable conditions and will be object of our future studies [5.66–5.68]. In addition, interesting competing effects between the cavity wavelength and the density length-scale can be found at different filling factors, leading to the emergence of incommensurate spin and density structures. The role of inter-particle interactions, neglected in this work, has to be investigated as well [5.31].

Acknowledgments

We thank Maria Luisa Chiofalo and Francesco Piazza for fruitful discussions. We acknowledge support by the Austrian Science Fund FWF through the Project SFB FoQuS F4013. W. N. acknowledges support from an ESQ fellowship of the Austrian Academy of Sciences (ÖAW).

Appendices

5.A Derivation of the many-body Hamiltonian

We consider a four-level fermionic atom coupled to two degenerate modes of a ring cavity, as represented in Fig. 5.1. The atomic motion is restricted along the cavity axis (z-direction). The four states $\{|\downarrow\rangle, |\uparrow\rangle, |e\rangle, |e'\rangle\}$ have energies $\{\hbar\omega_\downarrow = 0, \hbar\omega_\uparrow, \hbar\omega_e, \hbar\omega_{e'}\}$, respectively. The atom is pumped from the side by two lasers with frequencies $\{\omega_{p1}, \omega_{p2}\}$ and Rabi frequencies Ω_1 and Ω_2. The pumping lasers drive the transitions $|\downarrow\rangle \leftrightarrow |e\rangle$ and $|\uparrow\rangle \leftrightarrow |e'\rangle$, respectively. The cavity fields $\hat{a}_\pm$ couple both transitions $|e'\rangle \leftrightarrow |\downarrow\rangle$ and $|e\rangle \leftrightarrow |\uparrow\rangle$. The single-particle Hamiltonian for this system is

$$\begin{aligned} H_1(t) = &\sum_{i\in\{\uparrow,e,e'\}} \hbar\omega_i |i\rangle\langle i| + \hbar\omega_c\left(\hat{a}_+^\dagger\hat{a}_+ + \hat{a}_-^\dagger\hat{a}_-\right) \\ &+ \hbar\left(\Omega_1 e^{i\omega_{p1}t}|\downarrow\rangle\langle e| + \Omega_2 e^{i\omega_{p2}t}|\uparrow\rangle\langle e'| + \text{h.c.}\right) \\ &+ \hbar g_0\left(e^{ik_cz}\hat{a}_+|e'\rangle\langle\downarrow| + e^{-ik_cz}\hat{a}_-|e'\rangle\langle\downarrow| + e^{ik_cz}\hat{a}_+|e\rangle\langle\uparrow| + e^{-ik_cz}\hat{a}_-|e\rangle\langle\uparrow| + \text{h.c.}\right). \end{aligned} \tag{A5.1}$$

In order to eliminate the explicit time dependence we perform a unitary transformation to a frame where the lowest ground state $|\downarrow\rangle$ is at rest. Applying the unitary transformation

$$\begin{aligned} U(t) = &\exp\left\{i\Big[\Big(\frac{\omega_{p1}+\omega_{p2}}{2}\Big)(\hat{a}_+^\dagger\hat{a}_+ + \hat{a}_-^\dagger\hat{a}_-)\Big]t\right\} \\ &\times\exp\left\{i\Big[\Big(\frac{\omega_{p1}+\omega_{p2}}{2}\Big)|e'\rangle\langle e'| + \omega_1|e\rangle\langle e| + \Big(\frac{\omega_{p2}-\omega_{p1}}{2}\Big)|\uparrow\rangle\langle\uparrow|\Big]t\right\}, \end{aligned} \tag{A5.2}$$

the time-independent Hamiltonian $\tilde{H}_1 = UH_1U^\dagger + i\hbar(\partial_t U)U^\dagger$ is

$$\begin{aligned} \tilde{H}_1 = &\sum_{i\in\{\uparrow,e,e'\}} -\hbar\Delta_i|i\rangle\langle i| - \hbar\Delta_c\left(\hat{a}_+^\dagger\hat{a}_+ + \hat{a}_-^\dagger\hat{a}_-\right) + \hbar\left(\Omega_1|\downarrow\rangle\langle e| + \Omega_2|\uparrow\rangle\langle e'| + \text{h.c.}\right) \\ &+ \hbar g_0\left(e^{ik_cz}\hat{a}_+|e'\rangle\langle\downarrow| + e^{-ik_cz}\hat{a}_-|e'\rangle\langle\downarrow| + e^{ik_cz}\hat{a}_+|e\rangle\langle\uparrow| + e^{-ik_cz}\hat{a}_-|e\rangle\langle\uparrow| + \text{h.c.}\right), \end{aligned} \tag{A5.3}$$

where $\Delta_\downarrow = 0$, $\Delta_\uparrow = (\omega_{p2}-\omega_{p1})/2 - \omega_\uparrow$, $\Delta_e = (\omega_{p1}+\omega_{p2})/2 - \omega_e$, $\Delta_{e'} = \omega_{p1} - \omega_{e'}$ are the detunings of the four levels after the unitary transformation and $\Delta_c = (\omega_{p1}+\omega_{p2})/2 - \omega_\uparrow$ is the cavity detuning.

For large atomic detunings, the excited states are adiabatically eliminated and the Hamiltonian reduces to the one of a spin-1/2 system,

$$\begin{aligned} \tilde{H} = &\sum_{\sigma\in\{\downarrow,\uparrow\}}\left[\hbar\delta_\sigma + U_{0\sigma}\left(\hat{a}_+^\dagger\hat{a}_+ + \hat{a}_-^\dagger\hat{a}_- + \hat{a}_+^\dagger\hat{a}_-e^{-2ik_cz} + \hat{a}_-^\dagger\hat{a}_-e^{-2ik_cz}\right)\right]|\sigma\rangle\langle\sigma| \\ &+ \hbar\eta\left(|\uparrow\rangle\langle\downarrow| + |\downarrow\rangle\langle\uparrow|\right)\left(e^{ik_cz}\hat{a}_+ + e^{-ik_cz}\hat{a}_- + \text{h.c.}\right) - \hbar\Delta_c\left(\hat{a}_+^\dagger\hat{a}_+ + \hat{a}_-^\dagger\hat{a}_-\right), \end{aligned} \tag{A5.4}$$

with $\delta_\downarrow = 0$, $\delta_\uparrow = \omega_\uparrow - (\omega_{p2} - \omega_{p1})/2$, $U_{0\uparrow} = \hbar g_0^2/\Delta_e$ and $U_{0\downarrow} = \hbar g_0^2/\Delta_{e'}$, and for the balanced case $\eta \equiv \Omega_1 g_0/\Delta_e = \Omega_2 g_0/\Delta_{e'}$.

The many-body Hamiltonian for non-interacting particles is

$$H = \int dz \left(\hat{\Psi}_\uparrow^\dagger(z), \hat{\Psi}_\downarrow^\dagger(z)\right) \tilde{H} \begin{pmatrix} \hat{\Psi}_\uparrow(z) \\ \hat{\Psi}_\downarrow(z) \end{pmatrix}, \tag{A5.5}$$

where $\hat{\Psi}_\sigma(z)$ are fermionic field operators fulfilling the anti-commutation relation $\{\hat{\Psi}_\sigma(z), \hat{\Psi}_{\sigma'}^\dagger(z')\} = \delta(z-z')\delta_{\sigma,\sigma'}$. Finally, by adding an external longitudinal magnetic field $\mathbf{B} = (0, 0, B_z)$ we obtain Hamiltonian (5.1) in the main text.

5.B Heisenberg equations of motion for the cavity fields

The Heisenberg equations of motion for the photonic field operators are

$$\begin{aligned} i\hbar\partial_t \hat{a}_+ &= [\hat{a}_+, H] \\ &= -\hbar(\Delta_c - U_0 N + i\kappa)\hat{a}_+ + U_0 \int dz e^{2ik_c z}\hat{n}(z)\hat{a}_- + \hbar\eta \int dz e^{ik_c z}\hat{S}_x(z), \end{aligned} \tag{A5.6a}$$

$$\begin{aligned} i\hbar\partial_t \hat{a}_- &= [\hat{a}_-, H] \\ &= -\hbar(\Delta_c - U_0 N + i\kappa)\hat{a}_- + U_0 \int dz e^{-2ik_c z}\hat{n}(z)\hat{a}_+ + \hbar\eta \int dz e^{-ik_c z}\hat{S}_x(z). \end{aligned} \tag{A5.6b}$$

Here, $\hat{n}(z) = \hat{\Psi}_\uparrow^\dagger(z)\hat{\Psi}_\uparrow(z) + \hat{\Psi}_\downarrow^\dagger(z)\hat{\Psi}_\downarrow(z)$ is the atomic density operator and $\hat{S}_x(z) = [\hat{\Psi}_\uparrow^\dagger(z)\hat{\Psi}_\downarrow(z) + \hat{\Psi}_\downarrow^\dagger(z)\hat{\Psi}_\uparrow(z)]/2$ is the local spin operator in the x-direction. When the photonic operators evolve on a faster timescale with respect to the atomic dynamics, we can consider the stationary value of the photonic operators and express the mean-field average $\langle \hat{a}_\pm \rangle = \alpha_\pm$ as a function of mean-field atomic averages. The former equations become

$$-\hbar(\Delta_c - U_0 N + i\kappa)\alpha_+ + U_0 \mathcal{N}_{2k_c}\alpha_- + \hbar\eta\Theta = 0, \tag{A5.7a}$$

$$-\hbar(\Delta_c - U_0 N + i\kappa)\alpha_- + U_0 \mathcal{N}_{2k_c}^*\alpha_+ + \hbar\eta\Theta^* = 0. \tag{A5.7b}$$

Here, $\mathcal{N}_{2k_c}$ and Θ are the atomic averages defined in the main text in Eq. (5.11) and Eq. (5.12), respectively. The spin order parameter Θ plays the fundamental role in the superradiant phase transition. Note that a macroscopic cavity field can only be induced by the emergence of a spin self-ordered state (non-vanishing Θ). In contrast, the density self-ordering (non-vanishing $\mathcal{N}_{2k_c}$) does not act as a source of cavity photons in Eqs. (A5.7) but only induces the mixing between the two modes $\alpha_\pm$. By solving the coupled Eqs. (A5.7) we obtain Eqs. (5.10) in the main text.

5.C Dependence of the transition threshold on the filling factor

The analysis presented in the main text was performed for half filling $k_F/k_c = 1/2$. Here we would like to show the effect of different filling on the phases presented above. This

can most easily be done by looking at the dependence of the critical pump strength on the filling factor (see 5.C.1). For finite temperature the threshold is suppressed at half-filling due to the nesting condition, as it was already mentioned in the main text. The presence of harmonic confinement introduces inhomogeneities, influencing the atomic susceptibility as already noticed in [5.32]. Despite harmonic confinement, commensurate effects are still visible in the critical pump-cavity detuning curve when the nesting condition holds in the trap center. From 5.C.1 it can be seen that despite the fact that the critical pump strength is higher at filling factors different from half-filling, the system will still undergo a superradiant phase transition at threshold. Therefore, the predicted phases can in general be observed for different filling factors. Similar characteristics were found in single component Fermi gases for both red and blue detuning with respect to the atomic transition frequency [5.26, 5.28].

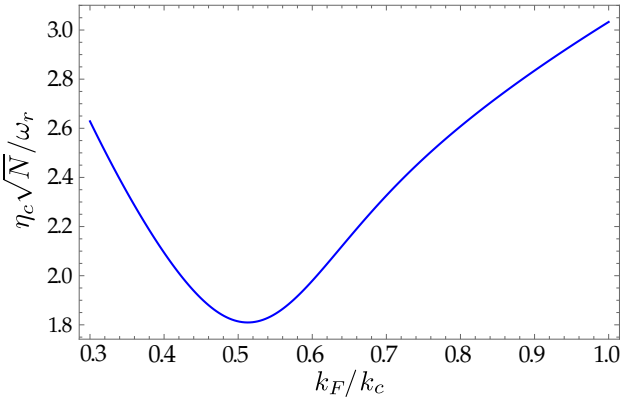

Figure 5.C.1: Critical threshold at fixed temperature for different filling factors, as obtained from Eq. (5.19).

6 The Hofstadter Butterfly in a Cavity-Induced Dynamic Synthetic Magnetic Field

Physical Review B, **100**, 224306 (2019)

The Hofstadter Butterfly in a Cavity-Induced Dynamic Synthetic Magnetic Field[†]

Elvia Colella[1], Farokh Mivehvar[1], Francesco Piazza[2] and Helmut Ritsch[1]

[1] *Institut für Theoretische Physik, Universität Innsbruck,*

Technikerstraße 21a, A-6020 Innsbruck, Austria

[2] *Max-Planck-Institut für Physik komplexer Systeme, D-01187 Dresden, Germany*

Energy bands of electrons in a square lattice potential threaded by a uniform magnetic field exhibit a fractal structure known as the Hofstadter butterfly. Here we study a Fermi gas in a 2D optical lattice within a linear cavity with a tilt along the cavity axis. The hopping along the cavity axis is only induced by resonant Raman scattering of transverse pump light into a standing wave cavity mode. Choosing a suitable pump geometry allows to realize the Hofstadter-Harper model with a cavity-induced dynamical synthetic magnetic field, which appears at the onset of the superradiant phase transition. The dynamical nature of this cavity-induced synthetic magnetic field arises from the delicate interplay between collective superradiant scattering and the underlying fractal band structure. Using a sixth-order expansion of the free energy as function of the order parameter and by numerical simulations we show that at low magnetic fluxes the superradiant ordering phase transition is first order, while it becomes second order for higher flux. The dynamic nature of the magnetic field induces a non-trivial deformation of the Hofstadter butterfly in the superradiant phase. At strong pump far above the self-ordering threshold we recover the Hofstadter butterfly one would obtain in a static magnetic field.

doi: 10.1103/PhysRevB.100.224306

[†]The author of this thesis performed all analytical and numerical calculations presented in this work. Farokh Mivehvar co-supervised this work, and Francesco Piazza provided helpful physical discussions in the interpretation of the data.

6.1 Introduction

In the last decade, advancements in the manipulation of cold atomic gases enabled to engineer Hamiltonians emulating the physics of effective gauge fields [6.1, 6.2]. The development of rotating traps [6.3, 6.4] allowed to overcome the challenge of coupling the external degrees of freedom of neutral atoms to an effective vector gauge potential as for charged particles. More sophisticated techniques based on light-matter interaction [6.5, 6.6] and lattice shaking [6.7, 6.8] were also developed to imprint a position-dependent geometric phase onto the atomic wave-function, analogous to the Aranov-Bohm phase of electrons in an external magnetic field [6.9]. The Hofstadter model [6.10, 6.11] was shortly after implemented for cold atoms in optical lattices by employing a laser-assisted tunneling scheme [6.12, 6.13, 6.18]. The realization of such an artificial magnetic field in lattice geometries [6.14, 6.15] allows one to explore the realm of topological many-body states of matter [6.16–6.18]. The most notable examples include measuring the Chern number of non-trivial topological bands [6.19] and realizing the Meissener phases for neutral atoms in ladder geometries [6.20]. More recently, new techniques exploiting internal degrees of freedom as synthetic dimension have been developed [6.21, 6.22] and are candidates for the observation of the quantum Hall effect even in four dimensions [6.23].

The experimental realization of lattice models with effective gauge potential is of great interest for engineering synthetic gauge theories [6.24]. Experimental realizations so far implemented static gauge fields which can be finely tuned by varying experimental parameters, but are not dynamically affected by the atomic back-action. However, in order to simulate a genuine gauge theory, quantum matter needs to be dynamically coupled to a gauge (bosonic) field and the back-action of the matter dynamics onto the gauge field should be accounted for. A first step in this direction is to use density-dependent synthetic gauge fields [6.25, 6.26], which were recently observed for a BEC in a shaken optical lattice [6.27, 6.28]. A Z_2 lattice gauge theory was also experimentally realized [6.29, 6.30].

Optomechanical systems [6.31, 6.32] as well as cold atoms in optical cavities [6.33] provide another natural route to the realization of a dynamical gauge theory in a controllable and accessible environment. This hinges on the non-linearity of these systems, where photons (phonons) feel the back-action of the atomic motion (photons). In view of the experimental realization of a strongly interacting Fermi gas coupled to a cavity [6.34] and the recent observation of a dynamical spin-orbit coupling in a BEC in a linear cavity [6.35–6.38] , theoretical proposals [6.39–6.47] for dynamical gauge fields are now in reach by experiments.

Here we study dynamical cavity-supported synthetic magnetic fields for fermions in an external optical lattice [6.12]. Atoms are driven by two transverse counter-propagating lasers and can scatter photons into the cavity. The hopping along the cavity axis is suppressed by a potential gradient. By choosing proper laser detunings, it can be activated by resonant Raman scattering of pump photons into a single resonant standing wave mode of the cavity [6.27]. Each pump laser here is responsible for a particular hopping direction. Above a critical pump strength, the collective buildup of the cavity

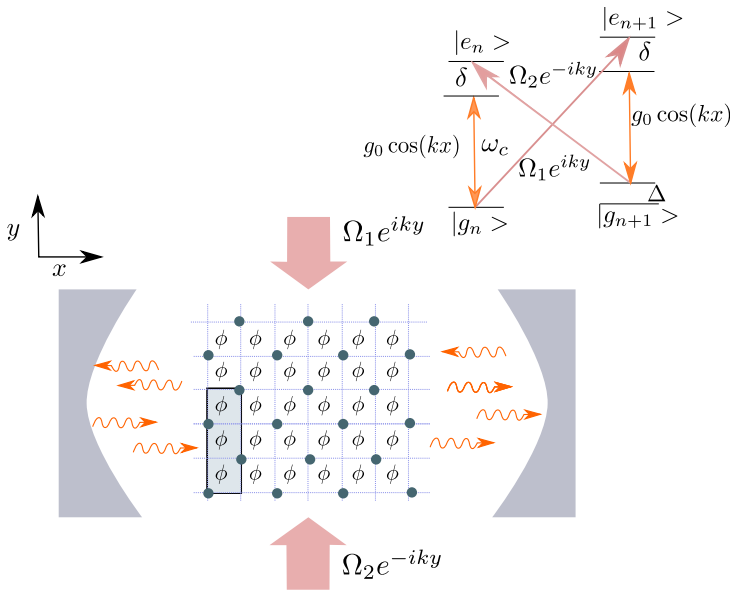

Figure 6.1: Geometry sketch to realize a dynamical version of the Harper-Hofstadter Hamiltonian: a 2D Fermi gas in a rectangular lattice within a single-mode optical cavity is transversely illuminated by two counter-propagating laser beams of orthogonal polarization. The shaded area in the lattice represents the unit cell for $\phi = 2\pi/3$.

field enables resonant coherent tunneling. In addition, for any closed loop in the atomic trajectory, a geometric phase proportional to the enclosed area is imprinted onto the atomic wave-function, in analogy to the phase acquired by electrons in a magnetic field.

The onset of the superradiant phase transition and the appearance of a synthetic magnetic field depends strongly on the phases imprinted, which can be tuned by setting the ratio between the lattice constant and the pump field wavelength $B \propto d_y/\lambda_c$. This is due to an intricate interplay between superradiant scattering generating the synthetic magnetic field and the emerging fractal energy bands corresponding to this field. Such cavity-induced atomic back-action on the effective gauge potential is very different to existing free-space implementations. Interestingly, as shown below, the onset of the superradiant phase transition (and hence appearance of the synthetic magnetic field) exhibits a first-order behavior at low fluxes, where the energy bands are Landau-like, while it becomes second-order for high flux. The energy spectrum itself carries the signs of the non-linearity of the atom-light interactions and the dynamical nature of the magnetic field, resulting in the emergence of peculiar structures compared to the commonly known energy spectrum, i.e., Hofstadter butterfly [6.11].

The paper is organized as follows. In section 6.2 we introduced the detailed system model. The physical results are summarized in section 6.3, where we focus on the bulk properties of the system at half-filling. Here the gas behaves as a metal or semi-metal depending on the value of the magnetic flux in a plaquette. We show the phase diagram,

the energy spectrum and we investigate the point of change of the phase transition from first to second order. Our final considerations are reported in section 6.4.

6.2 Model

We consider a Fermi gas confined in a two dimensional (2D) optical lattice of lattice constant, $\mathbf{d} = \{d_x, d_y\}$, in the tight binding regime. Hopping in the x-direction is suppressed by an additional energy gradient $\hbar\Delta$ between neighbouring sites. This can be realized by adding a constantly accelerated optical lattice, a magnetic field, or an electric field gradient along the x-direction. We consider only a single internal atomic transition $|g\rangle \leftrightarrow |e\rangle$ of frequency ω_0. The hopping in the x-direction is restored via two-photon resonant scattering processes mediated by cavity photons, where the resonance condition is $\omega_c \simeq \omega_1 + \Delta = \omega_2 - \Delta$ [6.12]. Here, ω_1 and ω_2 are the frequencies of the two transversal laser pumps; see Fig. 6.1.

Our model Hamiltonian in tight-binding approximation in a reference frame rotating at the average pump frequency $\omega_p = (\omega_1 + \omega_2)/2$ then reads: [6.27],

$$\begin{aligned} H = &- J_y \sum_{l,m} (f^\dagger_{l,m+1} f_{l,m} + \text{H.c.}) \\ &- \hbar\eta(a + a^\dagger) \sum_{l,m} (e^{2i\pi m\gamma} f^\dagger_{l+1,m} f_{l,m} + \text{H.c.}) \\ &- \hbar\Delta_c a^\dagger a. \end{aligned} \tag{6.1}$$

Here J_y is the hopping amplitude in the y-direction, $\eta = \Omega_1 g_0/\delta = \Omega_2 g_0/\delta$ is the two photon Rabi coupling with $\delta = \omega_p - \omega_0$ the atomic detuning with respect to the average pump frequency, g_0 is the bare coupling strength of the cavity mode to the atomic transition and $\Delta_c = \omega_p - \omega_c$ is the cavity detuning with respect to the average pump ω_p. Note that only resonant Raman scattering terms are retained in the Hamiltonian. Further details are presented in Appendix 6.A.

The spatial phase dependence of the pump lasers imprints a site-dependent tunneling phase $\gamma_m = m\gamma = mk_L/(2\pi/d_y)$. Hence, hopping around a plaquette, the wave-function acquires a total phase $\phi = 2\pi\gamma$, which can be related to an electron moving in a periodic potential threaded by a magnetic field of strength $|B| = 2\pi\gamma/(d_y^2 e)$.

The effective magnetic field breaks the translation symmetry of the original lattice and the Hamiltonian is invariant under a combination of discrete translation and a gauge transformation, i.e., magnetic translation. In particular, when $\gamma = p/q$ is a rational number with p and q being two integers, and the energy spectrum splits into q sub-bands, which cluster in a highly fractal structure known as Hofstadter butterfly [6.11].

In contrast to free space setups the hopping amplitude in the cavity-direction depends on the cavity field amplitude and the effective magnetic field appears only for non-zero cavity-field. Here the coherent amplitude $\langle a \rangle = \alpha$ is determined by the steady-state solution of the mean-field equation:

$$\frac{\partial \alpha}{\partial t} = -(\Delta_c - i\kappa)\alpha - \eta\Theta = 0, \tag{6.2}$$

where

$$\Theta = \sum_{l,m} \left(e^{-2i\pi\gamma m} \langle f^\dagger_{l,m} f_{l-1,m} \rangle + e^{2i\pi\gamma m} \langle f^\dagger_{l,m} f_{l+1,m} \rangle \right) \tag{6.3}$$

is the atomic order parameter, which reveals emergent currents of equal number of left and right moving atoms along the cavity axis. The order parameter Θ needs to be self-consistently determined by diagonalizing the Hamiltonian at fixed amplitude α,

$$\Theta = \frac{2}{N_k^2} \sum_m \sum_{s=1}^{q} \sum_{\mathbf{k} \in \text{B.Z.}} n_F(\epsilon_{s,\mathbf{k}}) \cos(2\pi m\gamma) |v_{s,\mathbf{k}}(m)|^2. \tag{6.4}$$

Here $\epsilon_{s,\mathbf{k}}$ and $v_{s,\mathbf{k}}(m)$ are the eigenvalues and eigenstates of the Harper equation [6.10]

$$\begin{aligned} &J_y[e^{ik_y} w_{\mathbf{k}}(m+1) + e^{-ik_y} w_{\mathbf{k}}(m-1)] + \\ &\quad 2\eta(\alpha + \alpha^*) \cos(k_x - 2\pi m\gamma) w_{\mathbf{k}}(m) = \epsilon w_{\mathbf{k}}(m). \end{aligned} \tag{6.5}$$

We use the following Ansatz for the atomic wave-function $\Psi(l,m) = e^{ik_x l} e^{ik_y m} w_{\mathbf{k}}(m)$, with $w_{\mathbf{k}} = \sum c_s v_{s,\mathbf{k}}(m)$ a linear superposition of the eigenstates of the Hamiltonian.

Equations (6.4) and (6.5) are solved self-consistently within the reduced Brillouin zone $k_x \in [-\pi, \pi]$ and $k_y \in [-\pi/q, \pi/q]$, for a magnetic unit cell with periodic boundary conditions in x and y directions. We focus on the contribution of the bulk to the superradiance, neglecting boundary effects which appear in a pair of chiral edge states [6.27].

6.3 Results

6.3.1 Phase diagram

For weak pump $\eta\sqrt{N}$ the system is in the uncoupled normal state (N), i.e., the atoms form a collection of independent chains in the y-direction and the cavity is empty. Increasing the effective pump strength the system exhibits a transition to a superradiant (SR) state, where photons are resonantly scattered into the cavity mode and the hopping in cavity (x)-direction builds up.

The stationary cavity-field amplitude is depicted in Fig. 6.1. It grows continuously above the superradiant threshold for large magnetic flux ($0.21 < \gamma < 0.5$) but displays a non-continuous jump at lower $\gamma < 0.21$. In order to better understand the change from a second to a first order phase transition, as presented in Appendix 6.B, we expand the free energy of the system in the Landau form up to sixth order in the atomic order parameter:

$$\begin{aligned} F \sim &(1 - \frac{4\Delta_c}{\Delta_c^2 + \kappa^2} \chi_1 \eta^2) |\Theta|^2 - \frac{8\Delta_c^3}{(\Delta_c^2 + \kappa^2)^3} \chi_3 \eta^6 |\Theta|^4 \\ &- \frac{64\Delta_c^5}{3(\Delta_c^2 + \kappa^2)^5} \chi_5 \eta^{10} |\Theta|^6. \end{aligned} \tag{6.6}$$

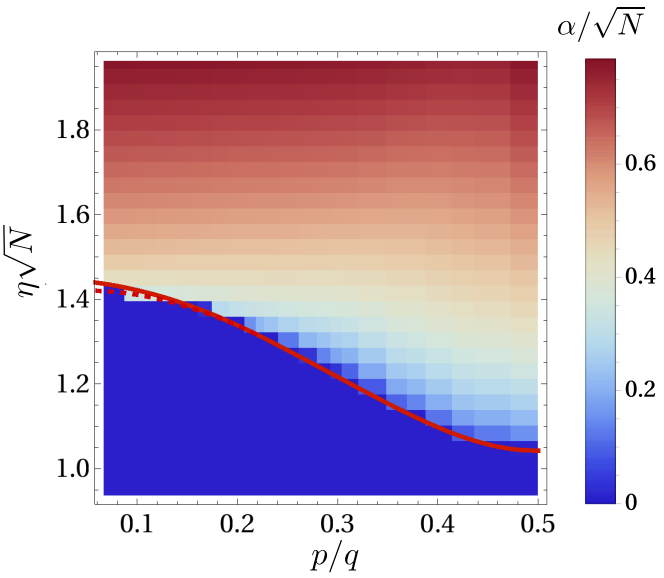

Figure 6.1: Phase boundary (red line) as function of effective flux $\gamma/2\pi = p/q$ and rescaled pump field $\eta\sqrt{N}$ using the field amplitude modulus $|\alpha|/\sqrt{N}$ as background color. Note that p/q is discrete and rational, with $1 < p < 7$ and $1 < q < 15$. The field amplitude is determined self-consistently for a Fermi gas at half-filling at fixed finite temperature $k_BT = 0.5E_R$, where $E_R = \hbar^2k_c^2/2m$ is the recoil energy. At small fluxes, $\gamma < 0.21$, the system exhibits a first-order phase transition, while for bigger fluxes it is of second order. The solid red line shows the analytical result for the critical threshold and the red dashed line the beginning of the region of hysteresis.

The effective optical response of the Fermi gas after cycles of absorption and emission of cavity photons is determined by the static susceptibilities, χ_i (Fig. 6.1). The linear susceptibility χ_1 determines the phase transition threshold

$$\sqrt{N}\eta_c = \sqrt{\frac{\Delta_c^2 + \kappa^2}{4\Delta_c\chi_1}N}, \tag{6.7}$$

which is shown as a red solid line in Fig. 6.1. The sign of χ_3 determines the order of the phase transition.

In particular, for strong magnetic fields we have $\chi_3 > 0$ and the transition is of the second order. The atoms then behave like a Kerr medium [6.48], inducing an intensity dependent shift of the refractive index, $n = n_0 + n_2 I$, with $n_2 = -8\chi_3\eta^2\Delta_c^3(\Delta_c^2 + \kappa^2)$. For decreasing magnetic field the third order susceptibility monotonically decreases becoming negative at $\gamma \simeq 0.21$, which renders the transition first order (bottom panel of Fig. 6.1). In this regime higher order susceptibilities only slightly depend on the magnetic flux γ. In fact the atomic orbit size significantly exceeds the unit cell of the original lattice,

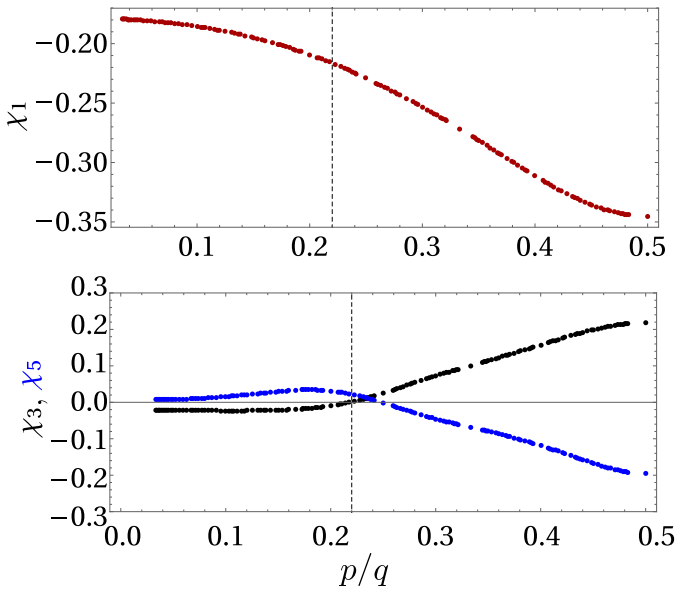

Figure 6.1: Atomic susceptibilities, χ_1 (red), χ_3 (black) and χ_5 (blue) at $k_bT = 0.5E_R$. The third order susceptibility χ_3 becomes negative below $p/q = 0.21$, signaled by the dashed black line.

making the lattice structure negligible. The system then exhibits a universal behaviour and the band structure corresponds to Landau levels in free space.

6.3.2 First-order transition

At low γ the emergent magnetic field has only little influence on the system dynamics. The temperature and the presence of an open Fermi surface then play a fundamental role in order to unravel the physical origin of the first order behaviour of the phase transition. By inspection of the temperature dependence of χ_3 for a Fermi gas at half-filling, we can identify an important change around $\gamma \approx k_F/k_L = 1/4$ (Fig. 6.2(a)). The susceptibility χ_3 is either positive at any temperature, or becomes negative at low temperature. The two regions are separated by the red solid line in Fig. 6.2(a).

In the latter case the phase transition becomes first order at low temperatures. This coincides with the regime where scattering one photon keeps the atomic momentum state within the same first Brillouin zone of the original lattice (normal scattering). In contrast, the transition becomes second order when the photon scattering is an Umklapp process (Fig. 6.2(b)), i.e., by inverting the direction of the atomic motion, a momentum transfer ($G = nk_L$) to the optical lattice is required. However, the occupation of higher energy states at higher temperature can favour the Umklapp processes at the expense of direct scattering enhancing the rate to scatter to the next Brillouin zone even for a small momentum transfer. This explains why at higher temperature a second order phase transition occurs and the critical temperature at which this happens increases for small

γ (Fig. 6.2(a)).

These results are confirmed by the numerical simulations at lower temperatures, $k_bT = 0.05E_R$. The re-scaled cavity amplitude as function of the pump strength either grows continuously around the threshold for $\gamma = 1/3$ (black line in Fig. 6.2(c)), or exhibits a jump at the critical point for $\gamma = 1/4$ (blue dashed line in Fig. 6.2(c)). For $\gamma = 1/3$ the rescaled amplitude shows an additional jump at higher pumps $\eta > \eta_c$, hinting that an additional first order transition inside the superradiant phase can appear. Such transition occurs when the cavity-induced hopping exceeds the hopping in the y-direction, $J_x/J_y = \eta(\alpha + \alpha^*) = 1$. The two superradiant states are characterized by the same order parameter but different isothermal compressibility, $\kappa_T = (1/\rho^2)\partial\rho/\partial\mu$, where ρ is the density of the Fermi gas. This divides the superradiant region into two phase zones: SRI

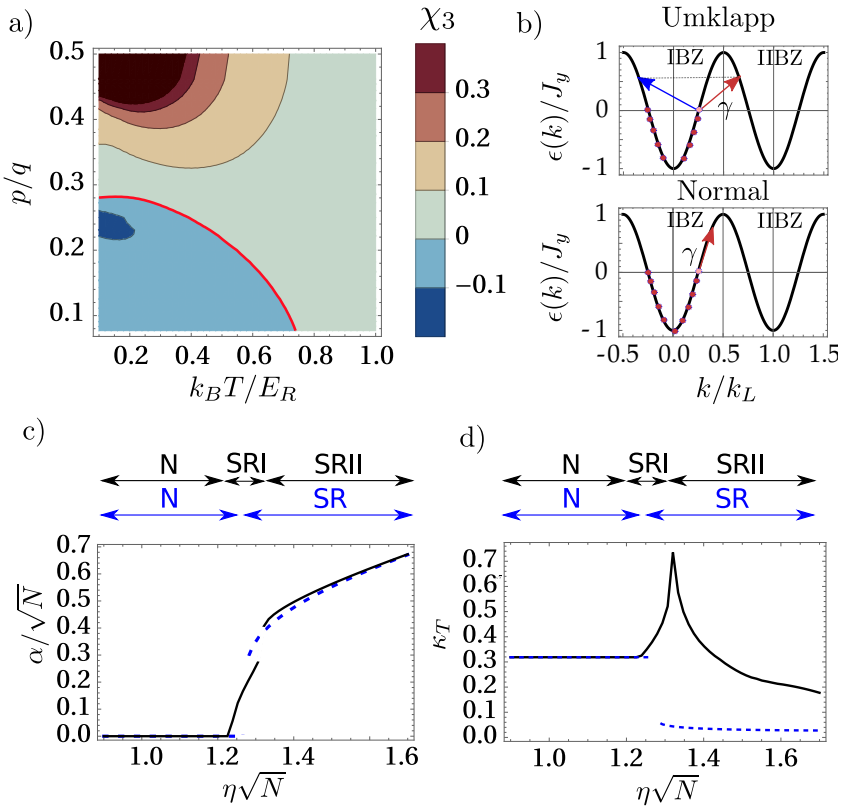

Figure 6.2: (a) Third order susceptibility, χ_3, as a function of the temperature and effective magnetic flux, $2\pi\gamma = 2\pi p/q$, with $1 < p < 6$ and $1 < q < 13$. The red line corresponds to zero susceptibility, separating positive and negative regions. (b) An atom at the Fermi surface is scattered after absorbing a photon to a higher energy state, via an Umklapp (top panel) or a normal process (bottom panel). The process is depicted using two Brilliouin zones of the original lattice. Cavity field amplitude (c) and isothermal compressibility (d) at $k_bT = 0.05E_R$, for $\gamma = 1/3$ (solid black) and $\gamma = 1/4$ (dashed blue).

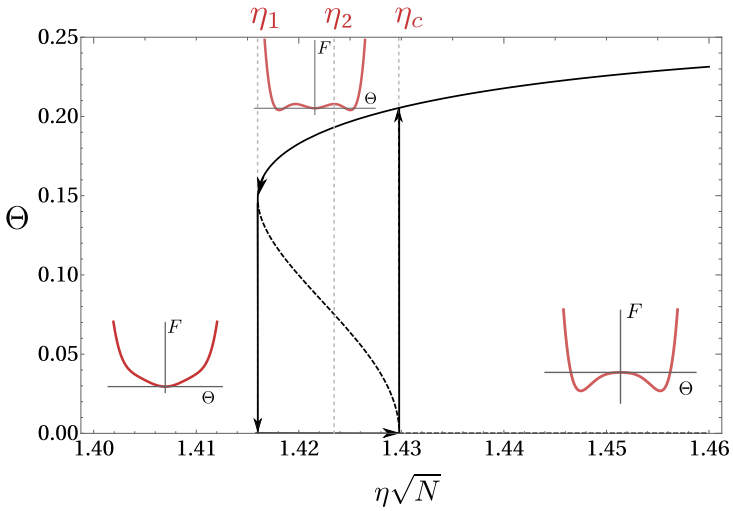

Figure 6.3: Atomic order parameter at $T = 0.5E_R$ for $\gamma = 1/12$ as a function of the effective pump $\eta\sqrt{N}$. The arrows shows the hysteresis loop and the dotted line represent the metastable solution. The insets show a qualitative picture of the free energy in the different regimes.

and SRII. In many respects this suggests a liquid-gas type of transition between the SRI and SRII phases, as confirmed by the rapid growth of density fluctuations that can be inferred from the divergence of the compressibility at the critical point (Fig. 6.2(d)). The transition is reminiscent of the case observed for fermions in linear cavities without external optical lattice [6.49]. In the latter case, however, the transition was driven by the coupling to an additional degree of freedom, in a process similar to the Larkin-Pimkin mechanism [6.50].

6.3.3 Hysteresis

For small magnetic flux the system exhibits a bi-stable hysteresis behaviour near the superradiant threshold η_c. The hysteresis loop and a qualitative picture of the free energy in the different regions are shown in Fig. 6.3. As can be seen in the insets, below the threshold

$$\eta_1 = \frac{\eta_c}{\sqrt{1 - \chi_3^2/(12\chi_1\chi_5)}}, \tag{6.8}$$

the solution with $\alpha = 0$ (empty cavity) is the only minimum of the free energy. Between $\eta_1 < \eta < \eta_c$ the free energy has three minima, either local or absolute. The solution for $\alpha \neq 0$ is metastable for $\eta_1 < \eta < \eta_2$, with

$$\eta_2 = \frac{\eta_c}{\sqrt{1 - 3\chi_3^2/(8\chi_1\chi_5)}}. \tag{6.9}$$

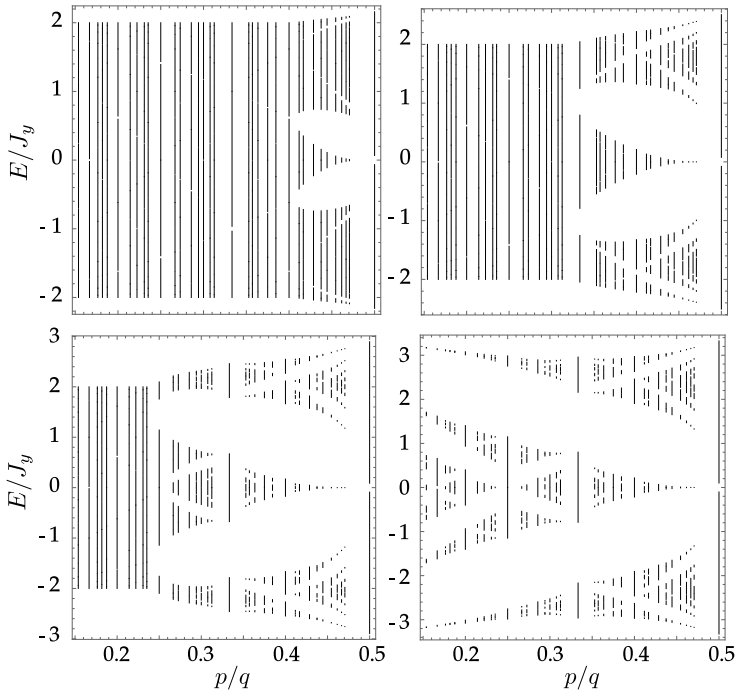

Figure 6.4: Energy spectrum as function of flux p/q for four different pump strength $\eta\sqrt{N} = \{1.1, 1.2, 1.3, 1.4\}E_R$ from top left to bottom right corner at $k_bT = 0.5E_R$. The spectrum initially shows singular shapes and reduces to the conventional Hofstadter butterfly at strong pump.

Between $\eta_2 < \eta < \eta_c$, the zero field solution $\alpha = 0$ is metastable and finally ceases to be a minimum at η_c, where the system becomes superradiant.

6.3.4 Dynamical Hofstadter Butterfly

Figure 6.4 shows the energy spectrum as a function of the magnetic flux p/q for increasing pump strength $\eta\sqrt{N}$. The magnetic field, $B \sim p/q$, emerges spontaneously with the cavity field amplitude and leads to the opening of $q-1$ gaps in the band structure. As the superradiant phase is entered already at lower pump power for stronger magnetic field, the gap opening progressively extends toward $p/q = 0$ as the pump is increased.

The different structures visible in the energy spectrum strongly depend on the pump strength. At low pump strength (top panels of Fig. 6.4) the gaps organize in the shape of a small butterfly confined in the region of large magnetic fields $0.21 < \gamma < 0.5$. The gaps close at the boundary of this region, where the amplitude of the cavity field is infinitesimally small. When the pump is increased the Hofstadter butterfly is entirely retrieved (right-bottom panel in Fig. 6.4) like in a static optical lattice. The gaps

will gradually close, generating a 1D tight-binding in the x-direction with bandwidth, $2J_x = 2\eta(\alpha + \alpha^*)$. In fact, the system evolves toward a regime of very weakly coupled 1D chains in the x-direction, for which the magnetic field can be gauged out.

The distortion of the energy spectrum, compared to the conventional Hofstadter butterfly [6.11], is due to the dynamical nature of the coupling between atoms and cavity photons. At a fixed magnetic field, the system spontaneously chooses the most favourable amplitude of the cavity field, i.e, the effective hopping parameter, $J_x = \eta(\alpha + \alpha^*)$. As the system becomes superradiant the effective Lorentz force exerted by the artificial magnetic field favours the tunneling in the x-direction, resulting in an asymmetry of the tunneling amplitudes. Therefore, the energy spectrum can be seen as the superposition of different Hofstadter butterflies with asymmetric hopping, $J_x - J_y$. While the fractal structure is preserved by the form of the Hamiltonian as the hopping phase is not cavity-dependent, the size of the gaps are set by the ratio of the hopping parameters and are characterized by a non-trivial dependence on the magnetic flux $2\pi p/q$.

This is illustrated in Fig. 6.5(a), where the hopping ratio J_x/J_y is shown as a function of the magnetic flux for different pump strengths. In the weak pump regime (black and dark blue lines) the dynamic butterfly is a superposition of static Hofstadter butterflies with very different effective hopping amplitudes. The hopping in the x-direction grows

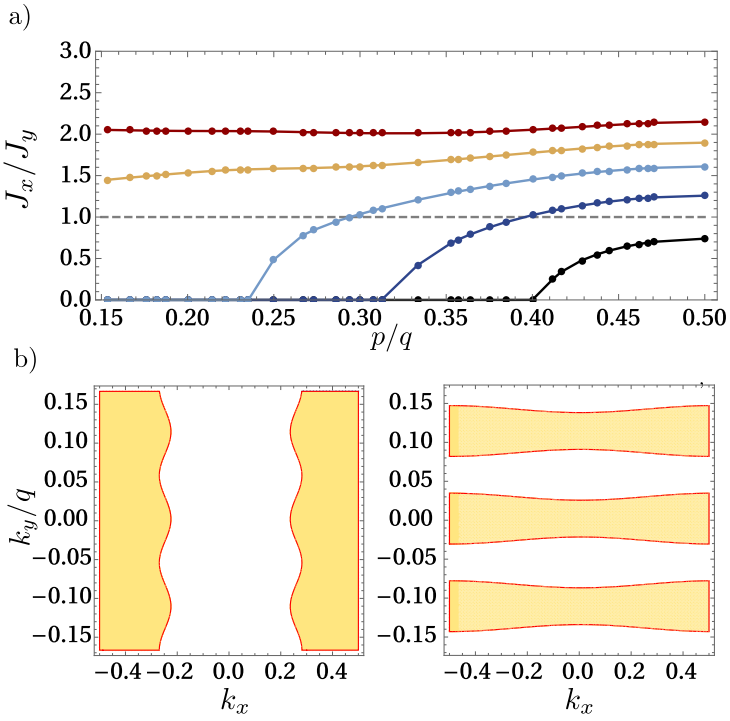

Figure 6.5: (a) Effective cavity induced hopping as a function of flux p/q at different pumping strengths. Parameters: $\eta\sqrt{N} = \{1.1, 1.2, 1.3, 1.4, 1.5\}E_R$ in black, dark blue, light blue, yellow and red respectively. (b) Fermi surface at $\gamma = 1/3$ for $k_bT = 0.5E_R$ for $\eta\sqrt{N} = 1.2E_R$ (left) and $\eta\sqrt{N} = 1.3E_R$ (right).

as the magnetic field is increased but remains rather small compared to the hopping in the other direction. As a consequence the curvature of the band structure and the Fermi surface align along y-direction, see left panel in Fig.6.5(b).

As the pump is increased, the field amplitude and the hopping in the x-direction become almost independent of the magnetic flux (red and yellow line in Fig 6.5(a)). In this regime the kinetic energy in the x-direction dominates and the Fermi surface aligns along the cavity axis. Note that at low temperature this is accompanied by the onset of a first order transition within the superradiant phase, SRI-SRII, as shown in the previous section.

6.4 Conclusions and Outlook

We have shown that non-linear coupling between atomic motion and a cavity field mode offers a new perspective on the generation of synthetic dynamical magnetic fields. In contrast to free space, the gauge field emerges spontaneously via maximizing the light scattered into the cavity and changing the atomic density configuration. The complex interplay between the fractal structure of the energy bands and the superradiant scattering thus generates new shapes for a dynamical Hofstadter butterfly.

Note that atoms are coupled only to a specific wave-length of the light field determined by the chosen cavity mode. As shown recently employing several distinct cavity modes the system gets more freedom and a global symmetry can "emerge" in a cavity-QED system [6.51]. Therefore, generalization of our studied system to multi-mode cavities and in particular a ring or fiber geometry [6.52] could allow to fully reproduce the minimal coupling of a charged particle to a local $U(1)$ gauge potential. Making use of the dynamical coupling between light and atoms in cavity systems is a promising route toward the experimental realization of synthetic dynamical gauge fields. Moreover, on a different level, the mediation of long-range two-body interactions due to the exchange of photons can lead to the observation of exotic states, as particles with anyonic statistics in fractional quantum Hall states.

Acknowledgments

F. M. is grateful to Nathan Goldman for fruitful discussions. F. M. is supported by the Lise-Meitner Fellowship M2438-NBL of the Austrian Science Fund (FWF), and the International Joint Project No. I3964-N27 of the FWF and the National Agency for Research (ANR) of France.

Appendices

6.A Effective Hamiltonian

Consider atoms loaded into a 2D optical lattice of lattice constant, $\mathbf{d} = [d_x, d_y]$. The hopping along x-direction is at first suppressed due to the potential offset Δ between adjacent lattice sites and then restored thanks to the cavity- and laser-assisted hoppings. The hopping along y-direction is due to the kinetic energy of the atoms. Let us just focus in the x-direction and consider three generic lattice sites labeled $n-1$, n, and n as in Fig. 6.A.1. First consider only transitions which involves the atomic excited state in site n, that is, $|e_n\rangle$. The Hamiltonian $H = H_0 + H_{\text{int}}$ reads ($\hbar = 1$),

$$H_0 = -(\omega_0 + \Delta)\sigma_{n-1} - \omega_0\sigma_n - (\omega_0 - \Delta)\sigma_{n+1} + \omega_c a^\dagger a, \tag{A6.1}$$

$$H_{\text{int}} = \Omega_2 e^{-iky} e^{-i\omega_2 t}\sigma_{n-1}^+ + g_0 \cos(kx_n) a\sigma_n^+ \Omega_1 e^{iky} e^{-i\omega_1 t}\sigma_{n+1}^+ + \text{H.c.}, \tag{A6.2}$$

where $\sigma_{n-1} = |g_{n-1}\rangle\langle g_{n-1}|$, $\sigma_n = |g_n\rangle\langle g_n|$, $\sigma_{n+1} = |g_{n+1}\rangle\langle g_{n+1}|$, $\sigma_{n-1}^+ = |e_n\rangle\langle g_{n-1}|$, $\sigma_n^+ = |e_n\rangle\langle g_n|$, $\sigma_{n+1}^+ = |e_n\rangle\langle g_{n+1}|$. For simplicity a two-photon resonance is assumed $\omega_c = \omega_1 + \Delta = \omega_2 - \Delta$ in the following and $k \equiv k_c \simeq k_1 \simeq k_2$.

Applying the unitary transformation $U = \exp\{-i[\omega_2\sigma_{n-1} + \omega_p(\sigma_n - a^\dagger a) + \omega_1\sigma_{n+1}]t\}$ to the Hamiltonian H yields,

$$\tilde{H} = \delta(\sigma_{n-1} + \sigma_n + \sigma_{n+1}) + [\Omega_2 e^{-iky}\sigma_{n-1}^+ g_0 \cos(kx_n) a\sigma_n^+ + \Omega_1 e^{iky}\sigma_{n+1}^+ + \text{H.c.}], \tag{A6.3}$$

where $\delta = \omega_c - \omega_0 \sim \omega_p - \omega_0$, with $\omega_p = (\omega_1 + \omega_2)/2$ the average pump frequency.Here we have made use of the relations $U\sigma_{n-1}^+ U^\dagger = e^{i\omega_2 t}\sigma_{n-1}^+$ etc. and $\tilde{H} = UHU^\dagger + i(\partial_t U)U^\dagger$. We find the stationary values of the operators σ_{n-1}^+, σ_n^+, σ_{n+1}^+ by setting to zero the the Heisenberg equation of motion $i\partial_t O = [O, \tilde{H}]$ upon assuming a large detuning δ

$$\begin{aligned}
\sigma_{n-1}^+ &\simeq \frac{1}{\delta}(\Omega_2^* e^{iky}\sigma_{n-1} + \Omega_1^* e^{-iky}\sigma_{n+1,n-1} + g_0 \cos(kx_n) a^\dagger \sigma_{n,n-1}), \\
\sigma_n^+ &\simeq \frac{1}{\delta}(\Omega_2^* e^{iky}\sigma_{n-1,n} + \Omega_1^* e^{-iky}\sigma_{n+1,n} + g_0 \cos(kx_n) a^\dagger \sigma_n), \\
\sigma_{n+1}^+ &\simeq \frac{1}{\delta}(\Omega_2^* e^{iky}\sigma_{n-1,n+1} + \Omega_1^* e^{-iky}\sigma_{n+1} + g_0 \cos(kx_n) a^\dagger \sigma_{n,n+1}),
\end{aligned} \tag{A6.4}$$

where $\sigma_{n,n-1} = |g_n\rangle\langle g_{n-1}|$, $\sigma_{n+1,n-1} = |g_{n+1}\rangle\langle g_{n-1}|$, $\sigma_{n+1,n} = |g_{n+1}\rangle\langle g_n|$, etc. Here we have also assumed a negligible population of the excited state, $|e_n\rangle\langle e_n| \simeq 0$, due to the large detuning δ.

Substituting Eq. (A6.4) back in the Hamiltonian (A6.3) yields the effective Hamiltonian,

$$\begin{aligned}
\tilde{H}_{\text{eff}}^{(n)} = \frac{2}{\delta}\{ & g_0^2 \cos^2(kx_n) a^\dagger a\sigma_n + [\Omega_2 g_0 e^{-iky} \cos(kx_n) a^\dagger \sigma_{n,n-1} \\
& + \Omega_1^* g_0 e^{-iky} \cos(kx_n) a\sigma_{n+1,n} + \text{H.c.}]\},
\end{aligned} \tag{A6.5}$$

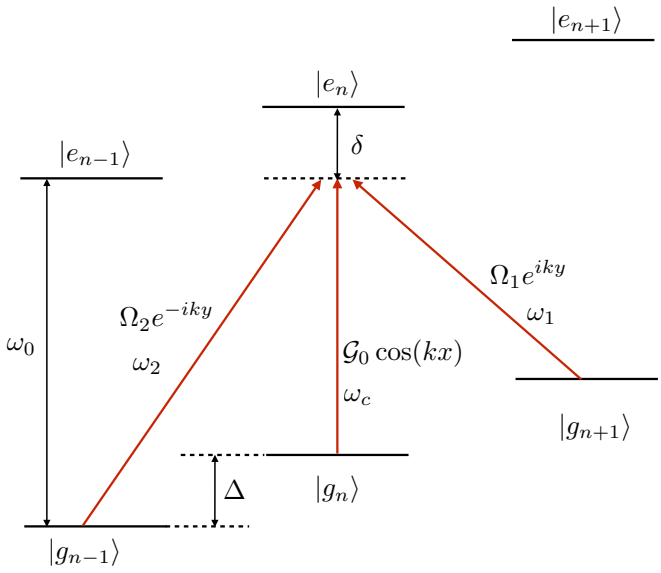

Figure 6.A.1: Three generic lattice sites along x direction.

where the constant terms proportional to Ω_1 and Ω_2, and terms involving next nearest neighbour scattering $\sigma_{n+1,n-1}$ have been omitted.

Considering now transitions which involve the states $|e_{n\pm1}\rangle$ results in the following contributions to the $\{n-1, n, n+1\}$ manifold,

$$\tilde{H}_{\text{eff}}^{(n-1)} \propto \frac{2}{\delta}\{g_0^2 \cos^2(kx_{n-1}) a^\dagger a \sigma_{n-1} + [\Omega_1^* g_0 e^{-iky} \cos(kx_{n-1}) a \sigma_{n,n-1} + \text{H.c.}]\},$$
$$\tilde{H}_{\text{eff}}^{(n+1)} \propto \frac{2}{\delta}\{g_0^2 \cos^2(kx_{n+1}) a^\dagger a \sigma_{n+1} + \left[\Omega_2 g_0 e^{-iky} \cos(kx_{n+1}) a^\dagger \sigma_{n1,n} + \text{H.c.}\right]\}. \quad \text{(A6.6)}$$

Assuming $\Omega_1 = \Omega_2 = \Omega \in \mathbf{R}$ and $\lambda_c = 2\pi/k = d_x$, the total effective Hamiltonian takes the form,

$$\tilde{H}_{\text{eff}} = \frac{2}{\delta}\sum_n \{g_0^2 \cos^2(kx_n) a^\dagger a \sigma_n + \Omega g_0 (a + a^\dagger)\left[e^{-iky} \cos(kx_n) \sigma_{n,n-1} + \text{H.c.}\right]\}, \quad \text{(A6.7)}$$

or in the second-quantized tight-binding formalism

$$\begin{aligned}\tilde{H}_{\text{eff}} &= a^\dagger a \sum_{n,m} \epsilon_{n,m} c_{n,m}^\dagger c_{n,m} \\ &+ (a + a^\dagger) \sum_{n,m} \left(J_{n,m}^x e^{-iky_m} c_{n,m}^\dagger c_{n-1,m} + \text{H.c.}\right) \\ &+ J^y \sum_{n,m} \left(c_{n,m}^\dagger c_{n,m-1} + \text{H.c.}\right), \end{aligned} \quad \text{(A6.8)}$$

where the hopping along the y direction is now also included. The matrix elements are given by,

$$\begin{aligned}
\epsilon_{n,m} &= \frac{2g_0^2}{\delta}\iint dxdy\cos^2(kx)|W(x-x_n)W(y-y_n)|^2 \\
&= \frac{2g_0^2}{\delta}\iint dx\cos^2(kx)|W(x-x_n)|^2, \\
J^x_{n,m}e^{-iky_m} &= \frac{2\Omega g_0}{\delta}\iint dxdyW^*(x-x_n)W^*(y-y_n)e^{-iky}\cos(kx)W(x-x_{n-1})W(y-y_m) \\
&= \frac{2\Omega g_0}{\delta}\int dx\cos(kx)W^*(x-x_n)W(x-x_{n-1}) \\
&\times \int dye^{-iky}W^*(y-y_m)W(y-y_m),
\end{aligned} \tag{A6.9}$$

where $W(\mathbf{X}-\mathbf{R}) = W(x-x_n)W(y-y_m)$ is the ground state Wannier function describing particles localized at the site $[n,m]$.

6.B Free energy expansion

In order to derive an effective Landau theory for the atomic order parameter Θ, as defined in the main text, we start from the the action of the system expressed in momentum space

$$S[\alpha,\alpha^*,c^\dagger_{k_x,k_y},c_{k_x,k_y}] = \Delta_c|\alpha|^2 + \frac{1}{\beta V}\sum_{n,k_x,k_y}\left(i\omega_n - 2J_y\cos(k_y)\right)c^\dagger_{n,k_x,k_y}c_{n,k_x,k_y} \tag{A6.10a}$$

$$-\eta(\alpha+\alpha^*)\frac{1}{\beta V}\sum_{k_x,k_y}\left(e^{-k_x}c^\dagger_{k_x,k_y}c_{k_x,k_y+\gamma} + e^{-k_x}c^\dagger_{k_x,k_y}c_{k_x,k_y-\gamma}\right).$$

Note that only the static component of the bosonic field α is retained, which is linearly related to the atomic order parameter by the equation of motion $\alpha = -\eta\Theta/(\Delta_c - i\kappa)$. We integrate out fermionic degrees of freedom, obtaining an effective action for the photonic field only, $S_{eff}[\alpha,\alpha^*] = \Delta_c|\alpha|^2 + \text{tr }\ln\hat{G}^{-1}$. The trace operator

$$\text{tr }\ln\hat{G}^{-1} = \text{tr }\ln G_0^{-1} - \sum_n \frac{1}{2n}tr(G_0\Gamma)^{2n} \tag{A6.11}$$

is obtained by perturbatively expanding the Green function $G(\mathbf{k},i\omega_n)$ around the zero order one

$$G_0^{-1} = \begin{bmatrix}
\ddots & 0 & 0 & 0 & 0 \\
0 & i\omega_n - 2J_y\cos(k_y-\gamma) & 0 & 0 & 0 \\
0 & 0 & i\omega_n - 2J_y\cos(k_y-\gamma) & 0 & 0 \\
0 & 0 & 0 & i\omega_n - 2J_y\cos(k_y-\gamma) & 0 \\
0 & 0 & 0 & 0 & \ddots
\end{bmatrix} \tag{A6.12}$$

where the perturbative term is given by the interaction matrix

$$\Gamma = -\eta(\alpha+\alpha^*)\begin{bmatrix} 0 & e^{-ik_x} & 0 & 0 & 0 \\ e^{ik_x} & 0 & e^{-ik_x} & 0 & 0 \\ 0 & e^{ik_x} & 0 & e^{-ik_x} & 0 \\ 0 & 0 & e^{ik_x} & 0 & e^{-ik_x} \\ 0 & 0 & 0 & e^{ik_x} & 0 \end{bmatrix} \tag{A6.13}$$

Here, $i\omega_n = \pi(2n+1)/\beta$ are fermionic Matsubara frequencies. By keeping up to the sixth order in α, the effective free energy is

$$F = \Delta_c|\alpha|^2 - \eta^2\chi_1(\alpha+\alpha^*)^2 - \frac{\eta^4}{2}\chi_3(\alpha+\alpha^*)^4 - \frac{\eta^6}{3}\chi_5(\alpha+\alpha^*)^6, \tag{A6.14}$$

or in powers of the atomic order parameter, Θ, reads

$$F \sim (1 - \frac{4\Delta_c}{\Delta_c^2+\kappa^2}\chi_1\eta^2)|\Theta|^2 - \frac{8\Delta_c^3}{(\Delta_c^2+\kappa^2)^3}\chi_3\eta^6|\Theta|^4 - \frac{64\Delta_c^5}{3(\Delta_c^2+\kappa^2)^5}\chi_5\eta^{10}|\Theta|^6 \tag{A6.15}$$

The free energy depends on the cavity properties and the coupling with the atoms is enclosed inside the susceptibilities

$$\chi_1 = \frac{1}{\beta}\sum_{n,k\in B.Z.} G_k(i\omega_n)G_{k+\gamma}(i\omega_n) \tag{A6.16a}$$

$$\chi_3 = \frac{1}{\beta}\sum_{n,k\in B.Z.} [G_k^2(i\omega_n)G_{k+\gamma}^2(i\omega_n) + 2G_{k-\gamma}(i\omega_n)G_k^2(i\omega_n)G_{k+\gamma}(i\omega_n)] \tag{A6.16b}$$

$$\begin{aligned}\chi_5 = \frac{1}{\beta}\sum_{n,k\in B.Z.} &[G_k^3(i\omega_n)G_{k+\gamma}^3(i\omega_n) + 3G_{k-\gamma}^2(i\omega_n)G_k^3(i\omega_n)G_{k+\gamma}(i\omega_n) \\ &+ 3G_{k-\gamma}(i\omega_n)G_k^3(i\omega_n)G_{k+\gamma}^2(i\omega_n) + 3G_k(i\omega_n)G_{k+\gamma}^2(i\omega_n)G_{k+2\gamma}^2(i\omega_n)G_{k+3\gamma}(i\omega_n)]\end{aligned} \tag{A6.16c}$$

The susceptibilities shown in the main text are numerically calculated by truncating the summation over the Matsubara frequencies until convergence with fixed chemical potential $\mu = 0$, same for the matrices $G_0(\mathbf{k}, \omega_n)$ and $\Gamma(\mathbf{k})$ which are summed in momentum space over the original Brillouin zone $[-\pi/d_x, \pi/d_y]$.

6.B.1 Expansion of the susceptibility for low magnetic fluxes

In order have a better understanding of the physics at low magnetic fluxes, we have analytically computed the expressions for the susceptibilities χ_1 and χ_3. The first order susceptibility is

$$\chi_1 = \sum_{k\in \mathrm{B.Z.}} \frac{n_F(\epsilon_{k+\gamma}) - n_F(\epsilon_k)}{\epsilon_{k+\gamma} - \epsilon_k}, \tag{A6.17}$$

with $\epsilon_k = J_y\cos(k)$, the tight binding energy along the y-direction where we set $\mu = 0$ for half filling. We expand χ_1 for small γ

$$\chi_1(\gamma \ll 1) = \sum_{k\in \mathrm{B.Z.}} \Big[-\beta n_F(\cos(k))\left[1 - n_F(\cos(k))\right]\Big] \tag{A6.18}$$

Note that the linear term vanishes and the main contribution to the linear susceptibility is a constant, which is proportional to the compressibility of a 1D chain of fermionic particles in the tight binding regime. As $n_F(\epsilon)$ is the probability that the state ϵ is occupied, while $1-n_F(\epsilon)$ is the probability that the state ϵ is not occupied, their product represent the scattering amplitude of a scattering process between two state of the same energy, which at very low temperature is only possible from one side to the other of the Fermi surface. The next contribution to χ_1 is quadratic and this behaviour can also be observed in the plot of the susceptibilty χ_1, see Fig 6.1 in the main text. Note that at the zero order, in γ we don't see the effect of the magnetic field but rather the temperature, dimensionality and filling play the fundamental role.

The third order χ_3 susceptibilty represents the response of the medium to three photon processes, through cycles of multiple emission and absorption. The full analytics expression is

$$\begin{aligned}\chi_3 = \sum_{k\in \text{B.Z.}} & -2\frac{n_F(\epsilon_{k+\gamma}) - n_F(\epsilon_k)}{(\epsilon_{k+\gamma}-\epsilon_k)^3} + \frac{n'_F(\epsilon_{k+\gamma}) - n'_F(\epsilon_k)}{(\epsilon_{k+\gamma}-\epsilon_k)^2} \\ & + 2\frac{n_F(\epsilon_{k-\gamma})}{(\epsilon_{k-\gamma}-\epsilon_k)^2(\epsilon_{k-\gamma}-\epsilon_{k+\gamma})} - 2\frac{n_F(\epsilon_{k+\gamma})}{(\epsilon_{k+\gamma}-\epsilon_k)^2(\epsilon_{k-\gamma}-\epsilon_{k+\gamma})} \\ & + 2\frac{n_F(\epsilon_k)}{(\epsilon_{k-\gamma}-\epsilon_k)(\epsilon_k-\epsilon_{k+\gamma})}\Big(\frac{1}{\epsilon_k-\epsilon_{k+\gamma}} + \frac{1}{\epsilon_k-\epsilon_{k-\gamma}}\Big) - 2\frac{n'_F(\epsilon_k)}{(\epsilon_{k-\gamma}-\epsilon_k)(\epsilon_k-\epsilon_{k+\gamma})}\end{aligned} \tag{A6.19}$$

In a linear cavity photons are in a superposition state of two conterpropagating momenta. The interaction with the cavity photons induces two type of processes. The first line refers to cycles of absorption and emission where the scattering processes always involve interactions with the same momentum component of the photon field. The other lines, refer to scattering processes in which a redistribution of photons between the two momentum component are involved. At the lowest order in γ, the susceptibility χ_3 becomes

$$\begin{aligned}\chi_3(\gamma \ll 1) = & \sum_{k\in \text{B.Z.}} \frac{\beta^3}{6} n_f(\epsilon_k)[1-n_f(\epsilon_k)] \\ & \times [1-6n_f(\epsilon_k)[1-n_f(\epsilon_k)]]\,.\end{aligned} \tag{A6.20}$$

7 Open Quantum-System Simulation of Faraday's Induction Law via Dynamical Instabilities

arXiv:2103.01979

Open Quantum-System Simulation of Faraday's Induction Law via Dynamical Instabilities[†]

Elvia Colella[1], Farokh Mivehvar[1], and Helmut Ritsch[1]

[1] *Institut für Theoretische Physik, Universität Innsbruck, Technikerstraße 21a, A-6020 Innsbruck, Austria*

We propose a novel type of a Bose-Hubbard ladder model based on an open quantum-gas–cavity-QED setup to study the physics of dynamical gauge potentials. Atomic tunneling along opposite directions in the two legs of the ladder is mediated by photon scattering from transverse pump lasers to two distinct cavity modes. The resulting interplay between cavity photon dissipation and the optomechanical atomic back-action then induces an average-density-dependent dynamical gauge field. The dissipation-stabilized steady-state atomic motion along the legs of the ladder leads either to a pure chiral current, screening the induced dynamical magnetic field as in the Meissner effect, or generates simultaneously chiral and particle currents. For sufficiently strong pump the system enters into a dynamically unstable regime exhibiting limit-cycle and period-doubled oscillations. Intriguingly, an electromotive force is induced in this dynamical regime as expected from an interpretation based on Faraday's law of induction for the time-dependent synthetic magnetic flux.

arXiv:2103.01979

[†]The author of this thesis performed all analytical and numerical calculations presented in this work. Farokh Mivehvar provided helpful discussion and support in the methodological problems and the physical interpretation of the results. The paper is currently under review process.

7.1 Introduction

Among alternative approaches to induce dynamical gauge potentials, quantum-gas–cavity-QED setups stand out owing to the intrinsic dynamical nature of cavity fields [6.1, 6.2]. Many interesting phenomena have been predicted to arise in systems with cavity-induced dynamical gauge potential, from the dynamical appearance of a vector potential at the onset of superradiance [6.3, 6.4] to a dissipation-induced dynamical Peierls phase [6.5] and the Meissner-like expulsion of a magnetic field [6.6]. The prediction of cavity-induced dynamic spin-orbit coupling [6.7–6.14] and its recent realization [6.15] has opened a new avenue for engineering dynamical gauge potentials alongside free-space schemes and experiments [6.16].

Motivated by the recent experimental realization of the dynamical spin-orbit coupling [6.15] and a two-mode Dicke model [6.17], here we propose a novel cavity-QED scheme for the implementation of an *average-density-dependent* dynamical gauge potential. In particular, we develop a ladder model [6.18] with cavity-assisted counterpropagating longitudinal atomic tunnelings as shown in Fig. 7.1. A dynamic gauge potential appears at the onset of the superradiant photon scattering from two transverse pump lasers into two cavity modes owing to dissipation-induced phase shifts of cavity photons. In contrast

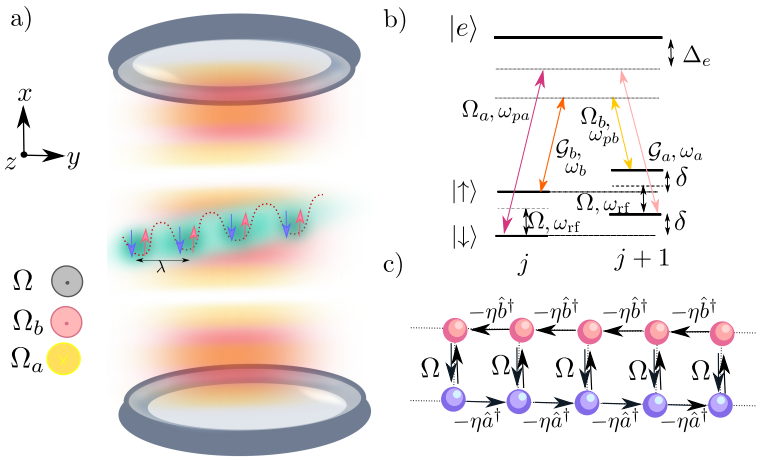

Figure 7.1: Sketch of the setup. (a) A spinor BEC is loaded into a 1D tilted external optical lattice perpendicular to the axis of a linear cavity. Neighbouring sites are Raman coupled via two cavity modes with strengths $\mathcal{G}_{a,b}$ and transversely applied laser fields with amplitudes $\Omega_{a,b}$. A microwave couples the two atomic states locally with strength Ω. (b) Sketch of the atomic level structure and of the two independent two-photon Raman transitions inducing directional atomic hopping between neighboring lattice sites. (c) Scheme of the effective mapping of the spinor BEC in the 1D lattice in panel (a) into a two-leg Bose-Hubbard ladder with cavity-assisted longitudinal hoppings and microwave-generated transverse tunneling.

to previous works [6.3–6.5], we take into account the optomechanical back-action of the atomic dynamics, leading to an average-density-dependent dynamical magnetic flux when the optomechanical back-action shifts significantly the cavity resonances and consequently the dissipation-induced photonic phases. The system exhibits three steady states: Photon-balanced Meissner (PB-M) and vortex (PB-V) states and a photon-imbalanced biased ladder (PI-BL) phase. In addition, the phase diagram of the system features a region of highly nonlinear dynamics with no steady state. Two stable dynamical phases are identified in this region with limit-cycle and period-doubled oscillations. Remarkably, an electromotive force is induced naturally in this regime, mimicking Faraday's law of induction.

7.2 Model

Consider a spinor Bose-Einstein condensate (BEC) inside a linear optical cavity. The BEC is strongly confined by a deep external optical lattice to a one dimension perpendicular to the cavity axis at anti-nodes of two distinct cavity electromagnetic modes, $\hat{a}$ and $\hat{b}$; see Fig. 7.1(a). The natural tunneling of atoms along the lattice is suppressed by applying an external potential gradient δ [6.19]. A directional hopping is restored by two independent resonant two-photon Raman transitions as shown schematically in Fig. 7.1(b): The ground pseudospin state $|\downarrow\rangle$ ($|\uparrow\rangle$) is coupled, respectively, by Rabi rates $\mathcal{G}_a$ ($\mathcal{G}_b$) and Ω_a (Ω_b) to a far detuned excited state $|e\rangle$ via the cavity mode $\hat{a}$ ($\hat{b}$) with resonance frequency ω_a (ω_b) and an out-of-plane transverse pump laser with frequency ω_{pa} (ω_{pb}). The two pseudospin ground states are coupled on-site with a rate Ω through a radio-frequency drive with frequency $\omega_{\rm rf}$.

For large atomic detuning, the excited state can be adiabatically eliminated. By only retaining resonant scattering terms, the effective Hamiltonian reads [6.20],

$$\begin{aligned}\hat{H} = &-\hbar\eta\sum_{j=1}^{L}(\hat{a}^\dagger\hat{c}^\dagger_{\downarrow,j+1}\hat{c}_{\downarrow,j} + \hat{b}\hat{c}^\dagger_{\uparrow,j+1}\hat{c}_{\uparrow,j} + \text{H.c.})\\ &- \hbar\Omega\sum_{j=1}^{L}(\hat{c}^\dagger_{\uparrow,j}\hat{c}_{\downarrow,j} + \text{H.c.})\\ &+ \frac{V}{2}\sum_{j=1}^{L}\sum_{\sigma=\uparrow,\downarrow}\hat{N}_{\sigma,j}(\hat{N}_{\sigma,j}-1) + \gamma V\sum_{j=1}^{L}\hat{N}_{\downarrow,j}\hat{N}_{\uparrow,j}\\ &- \hbar(\Delta_a - U\hat{N}_\downarrow)\hat{a}^\dagger\hat{a} - \hbar(\Delta_b - U\hat{N}_\uparrow)\hat{b}^\dagger\hat{b},\end{aligned} \tag{7.1}$$

where $\hat{c}_{\sigma,j}$ is the atomic bosonic annihilation operator for pseudospin σ at site j, and $\hat{N}_\sigma = \sum_j \hat{N}_{\sigma,j} = \sum_j \hat{c}^\dagger_{\sigma,j}\hat{c}_{\sigma,j}$. The effective model (7.1) constitutes a spinor Bose-Hubbard-type Hamiltonian with cavity-induced dynamical spin-orbit coupling. It can be effectively mapped into a two-leg Bose-Hubbard ladder of length L, with one of the two pseudospin states acting as a synthetic dimension [6.21]. In this spirit, the first row of the Hamiltonian corresponds to the motion of the atoms along the longitudinal direction (i.e., legs) of

the ladder. The forward tunneling amplitudes, $\hat{t}_{a(b)} \equiv \hbar\eta\hat{a}^\dagger(\hat{b})$, are restored by scattering photons from the pump (cavity) into the cavity (pump) at a rate $\eta = \mathcal{G}_a\Omega_a/\Delta_e = \mathcal{G}_b\Omega_b/\Delta_e$, with $\Delta_e = \omega_p - \omega_e$ being the effective atomic detuning from the average pump frequency $\omega_p = (\omega_{pa} + \omega_{pb})/2$. The second line can be interpreted as a transversal hopping along rungs of the ladder, with tunneling amplitude set by the radio-frequency coupling Ω. The third line takes into account repulsive two-body on-site atomic interactions, with V being the strength of intra-species interactions and γ parameterizing the ratio between the strength of inter- and intra-species interactions. The last two terms represent the free energy of the photon fields with the cavity detunings defined as $\Delta_{a(b)} = -\omega_p \pm \omega_{\rm rf}/2 - \omega_{a(b)}$, where in the following we assume $\Delta \equiv \Delta_a = \Delta_b$. The cavity resonances are shifted by the atomic medium $U\hat{N}_\sigma$, where $U = \mathcal{G}_a^2/\Delta_e = \mathcal{G}_b^2/\Delta_e$ is the dispersive shift per atom.

7.3 Average-density-dependent dynamical gauge potential and synthetic magnetic field

Let us now describe the mechanism by which a dynamical gauge potential can arise when the photon-assisted tunnelings $\hat{t}_{a,b}$ are restored. We recall that on a lattice, the coupling of a charged particle $\mathcal{Q}$ to a vector potential $\boldsymbol{\mathcal{A}}$ is approximately described by adding a phase to the tunneling amplitudes, known as the Peierls phase [6.22]. Peierls phase is fixed by the circulation of the vector potential along the path enclosing the unit cell of the lattice, and reduces to the Aharonov-Bohm phase in the continuum limit [6.23]. Therefore, the magnetic flux piercing a plaquette of the lattice is readily written as, $\Phi_B = \int_{\text{unit cell}} \boldsymbol{\mathcal{A}} \cdot d\mathbf{l}$

For neutral atoms the vector potential (or the Peierls phase) must be synthetically engineered via externally tailoring the atomic tunneling amplitudes. Here our scheme exploits the superradiant scattering of photons into the cavity to achieve this. In particular, in the superradiant phase the collective synchronized emission of photons results in a macroscopic occupation of the two cavity modes, which can be treated as classical electromagnetic fields. The cavity fields are thus described by coherent states [6.24], $\hat{a} \to \langle\hat{a}\rangle \equiv \alpha = |\alpha|e^{i\phi_\alpha}$ and $\hat{b} \to \langle\hat{b}\rangle \equiv \beta = |\beta|e^{i\phi_\beta}$, and the tunneling amplitudes for the lower and upper leg respectively reduce to *c-numbers* $t_a = \hbar\eta|\alpha|e^{i\phi_\alpha}$ and $t_b = \hbar\eta|\beta|e^{-i\phi_\beta}$. Note that the chosen pumping geometry is equivalent to make a well defined gauge choice where the the transverse component of the vector potential along the rungs $\mathcal{A}_j^\perp = 0$ vanishes, and its longitudinal component along the two legs coincide with the phases of the cavity fields $\mathcal{A}_{a,j}^\parallel \propto \phi_\alpha$ and $\mathcal{A}_{b,j}^\parallel \propto -\phi_\beta$. Hence, the total phase acquired by the atomic wavefunction around a closed loop along one plaquette is

$$\Phi = \phi_\alpha + \phi_\beta. \tag{7.2}$$

The dynamics of the atoms is equivalent to the one of charge particles $\mathcal{Q}$ threaded by the magnetic flux $\Phi_B = \hbar\Phi/\mathcal{Q} = \Phi_{0B}\Phi/2\pi$ with $\Phi_{0B} = h/\mathcal{Q}$.

In the adiabatic limit for the photonic dynamics [6.1, 6.2], the cavity fields can be slaved to the atomic degrees of freedom and be obtained from the stationary solution of

the Heisenberg equations of motion, $\alpha = -\eta\Theta_\downarrow/(\Delta_a - UN_\downarrow + i\kappa_a)$ and $\beta = -\eta\Theta^*_\uparrow/(\Delta_b - UN_\uparrow + i\kappa_b)$, where $\kappa_{a,b}$ are the decay rates of the cavity fields and $N_\sigma = \langle\hat{N}_\sigma\rangle$. This prescribes the phase locking between the photons and the average atomic hopping operators, $\Theta_\sigma = \sum_j \langle c^\dagger_{\sigma,j+1} c_{\sigma,j}\rangle$. Up to a global phase which can be gauged out, the phases of the cavity fields are uniquely determined [6.20],

$$\phi_{\alpha(\beta)} = \arctan\left(\frac{\kappa_{a(b)}}{\Delta_{a(b)} - UN_{\downarrow(\uparrow)}}\right). \tag{7.3}$$

The atomic ladder acts as a refractive medium for the light inside the resonator, and dispersively shifts the cavity resonances, i.e., $\Delta_{a(b)} - UN_{\downarrow(\uparrow)}$. Remarkably, the magnetic flux $\Phi_B \propto \phi_\alpha + \phi_\beta$ becomes non-linearly dependent on the atomic leg density via $UN_\sigma \propto N_\sigma/2L = \bar{n}_\sigma$.

In order to unveil the effect of the cavity-induced magnetic field, let us first consider the single-particle physics. The atomic part of the Hamiltonian (7.1) can be diagonalized to yield the single-particle atomic energy bands,

$$\frac{\epsilon_\pm(q)}{\hbar} = -\eta F_+ + \frac{U}{2} n_{\rm ph} \pm \sqrt{\Omega^2 + \left(\eta F_- - \frac{U}{2}\Delta n_{\rm ph}\right)^2}. \tag{7.4}$$

Here we have defined $F_\pm(q) = |\alpha|\cos(q+\phi_\alpha) \pm |\beta|\cos(q-\phi_\beta)$, $n_{\rm ph} = n_\alpha + n_\beta = |\alpha|^2 + |\beta|^2$ as the total number of photons, and $\Delta n_{\rm ph} = n_\alpha - n_\beta$ as the photon-number difference. The atomic quasi-momentum q is minimally-coupled to the phases $\phi_{\alpha,\beta}$ of photons, as expected. The system exhibits different behaviors depending on $\Delta n_{\rm ph}$. For the photon-balanced (PB) case, $\Delta n_{\rm ph} = 0$, the lowest energy band has either a single minimum at $q = 0$ or symmetric double minima at $q = \pm q_m \neq 0$. The atomic ground state corresponds to a Meissner (M) and a vortex (V) phase, respectively. For the photon-imbalanced (PI) case, $\Delta n_{\rm ph} \neq 0$, the energy bands become asymmetric, with the lowest band developing a single minimum at a nonzero quasi-momentum, $q = q_m \neq 0$. Consequently, the atomic ground state develops an atomic population imbalance in the two legs, which spontaneously breaks the $\mathbb{Z}_2$ reflection symmetry of the system corresponding to the invariance under the exchange of the cavity modes $\hat{a} \leftrightarrow \hat{b}^\dagger$ and ladder legs $\hat{c}_{\uparrow,j} \leftrightarrow \hat{c}_{\downarrow,j}$. We identify this state as the biased ladder (BL) phase [6.25–6.27].

We find the steady state of the system by looking at the long-time dynamics of the coupled Heisenberg equations of motion with periodic boundary conditions [6.20]. The steady-state phase diagram in the Δ–η parameter plane is mapped out in Fig. 7.1(a) for $N = 1$. Typical self-consistent energy bands are presented in Fig. 7.1(b), while Fig. 7.1(c) shows a horizontal cut through the phase diagram. In this non-interacting low-density regime $\bar{n} = \bar{n}_\downarrow + \bar{n}_\uparrow = 1/2L \ll 1$, the optomechanical back-action UN_σ of the atomic medium on the cavity resonances is negligible. Therefore, the magnetic flux Φ_B is almost density independent and can only be tuned by varying the cavity parameters Δ and κ; see the inset of Fig. 7.1(a).

By increasing the ladder density $\bar{n} = N/2L$, the dispersive shift UN_σ becomes significant, and hence the density dependence of the induced magnetic flux Φ_B becomes

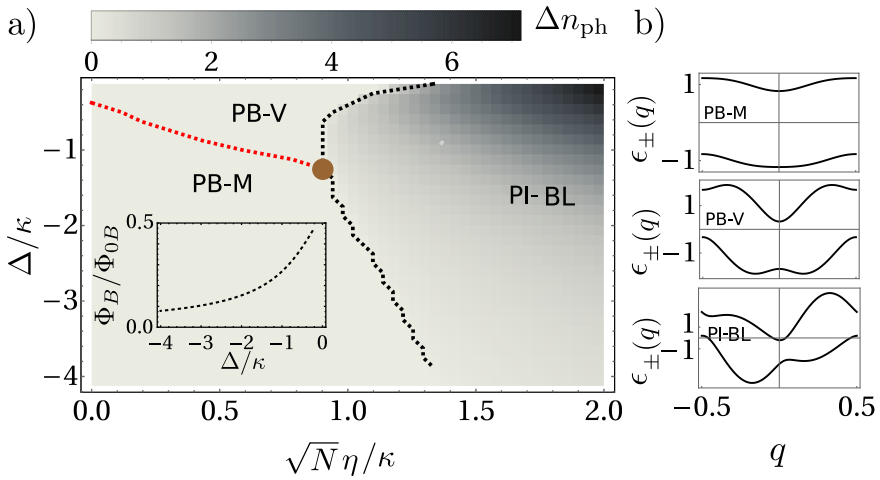

Figure 7.1: Single-particle phase diagram. (a) The steady-state phase diagram in the $\{\sqrt{N}\eta/\kappa, \Delta/\kappa\}$ parameter plane. The system exhibits three distinct phases: Photon-balanced Meissner (PB-M) and vortex (PB-V), and photon-imbalanced bias ladder (PI-BL) states. The color map indicates the photon imbalance $\Delta n_{\rm ph}$. The red dashed curve separating the PB-M and the PB-V states has been obtained analytically (see Supplementary Material). The three phases intersect in a tricritical point indicated by the brown dot. Inset: The synthetic magnetic flux Φ_B/Φ_{0B} as a function of Δ/κ. For $\Delta/\kappa = -0.5$, (b) typical band structure $\epsilon_\pm(q)$ in each phase corresponding to $\sqrt{N}\eta/\kappa = \{0.08, 0.50, 1.00\}$, respectively, and (c) photon amplitudes as a function of the pump strength. Other parameters are set to $L = 51$, $U = \Delta/2L$, $\Omega = 1$, and $V = \gamma = 0$.

apparent. Figure 7.1(a) shows for weak on-site interactions the stationary value of the magnetic flux Φ_B/Φ_{0B} as a function of the average atomic density $\bar{n} = N/2L$ and the pump strength $\sqrt{N}\eta$ for cavity detuning, $\Delta = -6\kappa$. The gray color indicates a dynamical region with no steady-state solution, which will be discussed in more detail later. Figure 7.1(a) shows that density effects become relevant for higher fillings, where the two cavity modes are dispersively shifted closer to resonance. The total photon number $n_{\rm ph}$ and the relative photon number difference $|\Delta n_{\rm ph}|/n_{\rm ph}$ are shown in Figure 7.1(b) and (c), respectively. The system exhibit phase transition from a photon balanced to a photon imbalanced phase when the pumping strength is increased (white solid line in Figure 7.1). Note that for large cavity detunings only weak magnetic fields can be stabilized in the system $\Phi_B/\Phi_{0B} < 0.15$, which do not support a PB-V phase-transition at weak pumping.

7.4 Superradiance and persistent currents

Since each photon scattering process is accompanied by a directional atomic tunneling along the legs of the ladder, stationary currents flowing in opposite directions are generated in the superradiant phase; see the sketch in Fig. 7.1(c). Dissipation plays an essential role in the generation of these currents [6.5]. By inspection of the leg currents, $J_\downarrow = -i\eta \sum_j \langle a^\dagger \hat{c}^\dagger_{\downarrow,j+1} \hat{c}_{\downarrow,j} - \text{H.c.}\rangle$ and $J_\uparrow = -i\eta \sum_j \langle \hat{b}\hat{c}^\dagger_{\uparrow,j+1} \hat{c}_{\uparrow,j} - \text{H.c.}\rangle$, one sees that for the steady state the leg currents are proportional to the photon number of the respective coupled modes, $J_\downarrow = -2\kappa|\alpha|^2$ and $J_\uparrow = 2\kappa|\beta|^2$. The chiral current is, therefore, determined by the total number of photons leaked out of the cavity, $J_c = J_\downarrow - J_\uparrow = -2\kappa n_{\text{ph}}$, while the photon number difference identifies the net particle current, $J_p = J_\downarrow + J_\uparrow = -2\kappa \Delta n_{\text{ph}}$. The current patterns are illustrated schematically in Fig. 7.1(d). At weak pumpings, a Meissner phase is stabilized with a pair of equal, counterpropagating currents flowing along the two legs. At stronger pump strengths a net particle current is driven by the photon imbalance in the biased ladder phase [6.25–6.27].

7.5 Dynamical instabilities and Faraday's induction law

We now take a closer look into the grey region of Fig. 7.1, where the system exhibits a highly nonlinear dynamics (NLD). A full characterization of the dynamical phases and their stability will be presented elsewhere. When the long-time dynamics is characterized by periodic oscillation of the cavity field amplitudes [see Fig. 7.2(a) III and (b) III], the system behaves like a limit-cycle oscillator. Self-sustained periodic oscillations of the cavity modes spontaneously emerge in the absence of an external periodic drive, breaking the continuous time-translational symmetry [6.28]. The time-translational symmetry breaking in driven-dissipative systems has been recently interpreted as a dissipative time crystal [6.29, 6.30]. The system also exhibits a period-doubling bifurcation at stronger pumping, that can be traced back into the appearance of an additional halved frequency component above the main limit-cycle oscillation frequency, possibly leading to chaos [6.31].

The nontrivial dynamics of the photonic phases shown in Fig. 7.2 leads to a time-dependent magnetic flux $\Phi_B(t)$. This in turn induces an electromotive force $\mathcal{E}(t) = -\partial\Phi_B(t)/\partial t = -(\Phi_{0B}/2\pi)\partial\Phi(t)/\partial t$, with

$$\frac{\partial \Phi(t)}{\partial t} = 2\Delta - UN - \frac{K_\downarrow}{2|\alpha|^2} - \frac{K_\uparrow}{2|\beta|^2}, \tag{7.5}$$

and the average longitudinal kinetic energies, $K_\downarrow = -2\eta \text{Re}(\alpha^* \Theta_\downarrow)$ and $K_\uparrow = -2\eta \text{Re}(\beta^* \Theta^*_\uparrow)$. The time evolution of the magnetic flux and the induced electromotive force are shown in the insets of Fig. 7.2(a) I and (b) I. The time-dependent electromotive force drives periodically the atomic population between the two legs, apparent from the oscillating chiral J_c and particle J_p currents as well as the emergent oscillating rung current $J_\perp = -i\Omega \sum_j \langle \hat{c}^\dagger_{\uparrow,j} \hat{c}_{\downarrow,j} - \text{H.c.}\rangle$; see Fig. 7.2(a) II and (b) II. In contrast to the steady-state results the photon-number counts are no longer an exact measurement of the leg currents

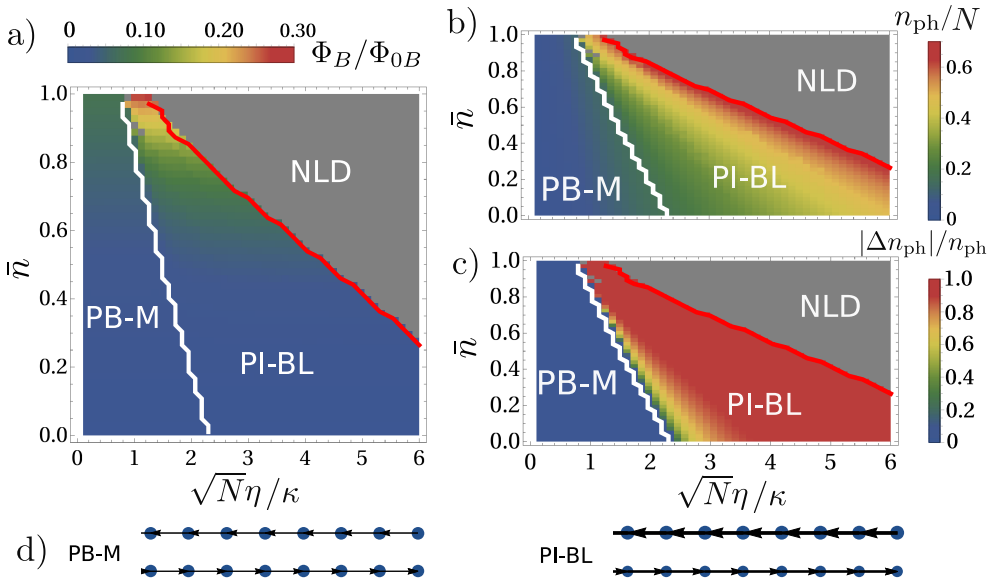

Figure 7.1: Many-body phase diagram. (a) The non-equilibrium phase diagram in the $\{\sqrt{N}\eta/\kappa, \bar{n}\}$ parameter plane. For the chosen cavity detuning $\Delta/\kappa = -6$, the system exhibits only two of the steady-state phases of Fig. 7.1(a): the PB-M and the PI-BL states. The two phases are separated by the solid white line. The gray area indicates a region of dynamical instability with no steady state [cf. Fig. 7.2]. The color map indicates the steady-state synthetic magnetic flux Φ_B, clearly showing average-density dependence. The total photon number $n_{\rm ph}$ (b) and the photon number difference $\Delta n_{\rm ph}/n_{\rm ph}$ (c) are shown in the same parameter plane. Photon number saturates the scale in the bright blue region in (b). (d) Typical current patterns in the PB-M and the PI-BL states. The parameters are the same as Fig. 7.1, except $VN = 1$, $\gamma = 0.1$.

(cf. panels II and III in Fig. 7.2). One can think of the residual currents as induction currents which oppose the variation of the magnetic flux, thus mimicking Faraday's law of induction with neutral particles [6.32].

7.6 Experimental considerations.

Our proposal can be realized by driving two optical transitions of ^{87}Rb atoms as in Ref. [6.15]. In an experiment, several atomic ladders can be isolated from single rows of a 2D optical lattice in the plane intercepted by the cavity axis and the y direction. The size of the ladder in the y direction is strictly limited by the cavity waist w_0. Assuming a transversal size of $2w_0 \sim 150$ μm, an atomic cloud of $\ell_y \sim 70$ μm, and an optical lattice with the lattice constant $a = \lambda_{851\rm nm}/2 = 0.426$ μm, the ladder would have $N_{\rm u.c} = \ell_y/a \sim 160$ unit cells. Upon redistribution of the cloud into the 2D lattice, and

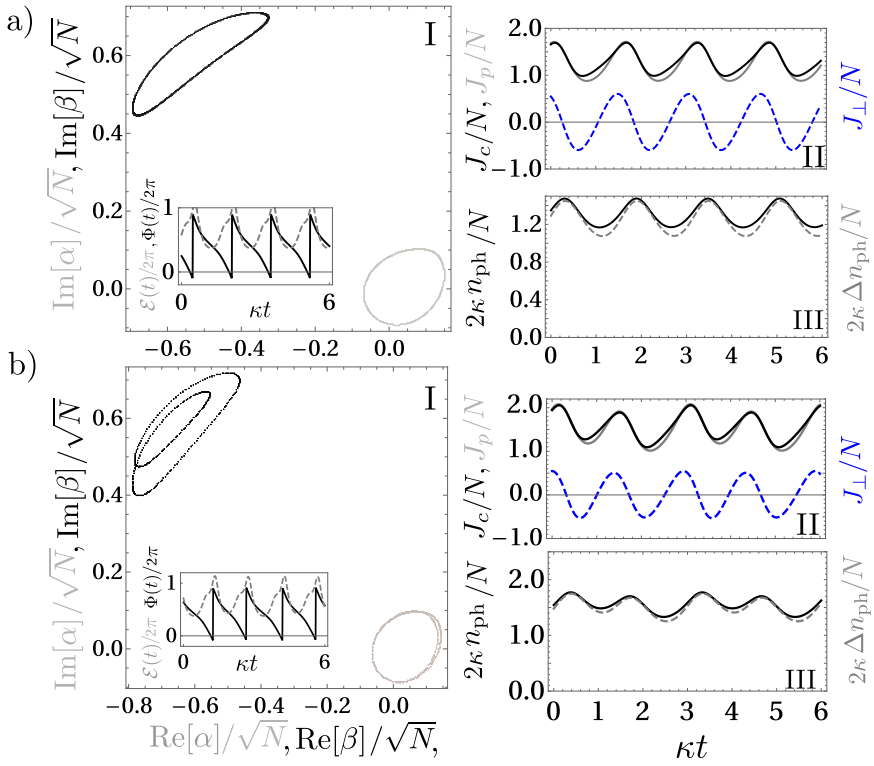

Figure 7.2: Periodic nonlinear dynamics in the unstable parameter regime (NLD), for high densities $\bar{n} = 1.42$. The phase space trajectories of the two cavity-mode amplitudes α (gray) and β (black) for long-time dynamics with $\sqrt{N}\eta/\kappa = 1.3$ (a) and 1.55 (b) [outside of the phase diagram of Fig. 7.1]. Insets in panels (I): Time evolution of the magnetic flux (black) and e.m.f (dashed gray). Time evolution of the induced chiral J_c (black), particle J_p (dashed gray), and rung $J_\perp$ (dotted blue) currents (II), and of the total photon number n_{ph} (black) and the photon number difference Δn_{ph} (dashed gray) (III). Panel (a) exhibits stable limit-cycle oscillations, while panel (b) shows period-doubled oscillations. Other parameters are same as Fig. 7.1 for $N = 140$.

assuming a longitudinal cloud size of $\ell_x \sim 2\ell_y$, the filling of the 2D lattice can be varied in a range of $\nu = N/(\ell_x \ell_y) \in [0.1, 2]$ for an atomic cloud of $N \sim 0.05 - 1.1 \times 10^5$ atoms, respectively. A lattice filling $\nu = 2$ would correspond to a ladder density $\bar{n} = 1$. The impact of the dispersive shifts UN_σ on the cavity resonances is significant in the strong light-matter coupling limit. A good measure of the coupling strength is provided by the parameter UN/κ, expressing the ratio between the coherent and incoherent processes in the system. For a high-finesse cavity with a linewidth of $2\kappa = 17$ kHz, $U = 91$ kHz as in Ref. [6.33], and $N = 4 \times 10^5$ atoms, the optomechanical back-action would be of the order of $UN/\kappa \sim 2.5 > 1$, a desired range to observe the predicted phenomena. The critical

advantage of our scheme is that the phase diagram can be non-destructively measured by monitoring photons leaking out of the cavity. The steady-state atomic currents can be obtained from the population count of the two cavity modes at the detector. The magnetic flux can be inferred through homodyne detection by measuring the phase of the two mode with respect to a probe laser.

7.7 Conclusions

We studied the emergence of an average-density-dependent dynamical U(1) gauge potential when the motion of neutral atoms is strongly coupled to two high-Q cavity modes. The gauge potential stems from the delicate interplay between the optomechanical atomic back-action on the cavity fields and photon dissipation into the environment. It differs from previously studied cavity-induced gauge potentials which do not feature any atomic-density dependence [6.3–6.5, 6.7–6.13, 6.13–6.15, 6.34]. The resulting complex interplay of atomic currents and the induced gauge potential can create dynamical instabilities with stable limit-cycle and period-doubled oscillations. This behaviour can be interpreted as an effective oscillating electromotive force according to Faraday's law of induction. Our proposed scheme offers a unique possibility to explore these exotic nonequilibrium phenomena in state-of-the-art quantum-gas–cavity-QED experiments.

7.8 Acknowledgments

E. C. is especially thankful to Arkadiusz Kosior for his critical reading of the manuscript and his insightful comments, as well as to Stefan Ostermann and Lluis Hernandez-Mula for fruitful discussions. E. C. is a recipient of a DOC Fellowship of the Austrian Academy of Sciences and acknowledges a support from the Austrian Science Fund (FWF) within the DK-ALM (W1259-N27). F. M. is supported by the Lise-Meitner Fellowship M2438-NBL of the FWF, and the International Joint Project No. I3964-N27 of the FWF and the National Agency for Research (ANR) of France.

Appendices

7.A Effective Hamiltonian

Internal level structure and pumping configuration.—Le us consider a three-level atom $\{\langle\downarrow|, \langle\uparrow|, \langle e|\}$ with frequencies, $\omega_\downarrow < \omega_\uparrow < \omega_e$, placed in a multi-mode linear cavity with the cavity axis oriented along the $\hat{x}$ direction. The atom interacts with two distinct cavity modes, $\hat{a}$ and $\hat{b}$, with frequencies ω_a and ω_b, and is transversally pumped in the $\hat{z}$ direction by two independent lasers of frequencies ω_{pa} and ω_{pb}, and intensities Ω_a and Ω_b. The two atomic pseudospin ground states, $\{\langle\downarrow|, \langle\uparrow|\}$, are coupled by a radio-frequency laser with frequency $\omega_{\rm rf}$ and intensity Ω. Note that we consider the atom located at a fixed position at one of the shared maxima of intensity of the cavity fields, $\cos(k_a x_j) = \cos(k_b x_j) = 1$. Hence, any space-dependence along the cavity axis due to the mode function of light fields is dropped out in the discussion below. The total Hamiltonian of the internal degrees of freedom only reads

$$H(t) = \hbar\omega_\downarrow |\downarrow\rangle\langle\downarrow| + \hbar\omega_\uparrow |\uparrow\rangle\langle\uparrow| + \hbar\omega_e |e\rangle\langle e| + \hbar\omega_a \hat{a}^\dagger\hat{a} + \hbar\omega_b \hat{b}^\dagger\hat{b} \tag{A7.1}$$

$$+ \left[-\hbar\Omega e^{-i\omega_{\rm rf}t} |\uparrow\rangle\langle\downarrow| + \left(\hbar\Omega_a e^{-i\omega_{pa}t} + \hbar\mathcal{G}_a\hat{a}\right)|e\rangle\langle\downarrow| + \left(\hbar\Omega_b e^{-i\omega_{pb}t} + \hbar\mathcal{G}_b\hat{b}\right)|e\rangle\langle\uparrow| + \text{H.c.}\right]. \tag{A7.2}$$

Introducing the average pump frequency $\omega_p = (\omega_{pa} + \omega_{pb})/2$, we recast the Hamiltonian in a time-independent form by applying a unitary transformation to an appropriate co-rotating frame,

$$U(t) = \exp\left\{i\left[-\frac{\omega_{\rm rf}}{2}|\downarrow\rangle\langle\downarrow| + \frac{\omega_{\rm rf}}{2}|\uparrow\rangle\langle\uparrow| + \omega_p|e\rangle\langle e| + \left(\omega_p + \frac{\omega_{\rm rf}}{2}\right)\hat{a}^\dagger\hat{a} + \left(\omega_p - \frac{\omega_{\rm rf}}{2}\right)\hat{b}^\dagger\hat{b}\right]t\right\}. \tag{A7.3}$$

Upon the satisfaction of the resonance condition $(\omega_{pa} - \omega_{pb}) = \omega_{\rm rf}$, the time-independent Hamiltonian, $\tilde{H} = UH(t)U^\dagger + i\hbar(dU/dt)U^\dagger$, reads as

$$\begin{aligned}\tilde{H} = &-\hbar\Delta_\downarrow|\downarrow\rangle\langle\downarrow| - \hbar\Delta_\uparrow|\uparrow\rangle\langle\uparrow| - \hbar\Delta_e|e\rangle\langle e| - \hbar\Delta_a\hat{a}^\dagger\hat{a} - \hbar\Delta_b\hat{b}^\dagger\hat{b}\\ &+ \hbar\left(\Omega_a + \mathcal{G}_a\hat{a}\right)|e\rangle\langle\downarrow| + \hbar\left(\Omega_b + \mathcal{G}_b\hat{b}\right)|e\rangle\langle\uparrow| + \text{H.c.}\end{aligned}$$

Here the atomic detunings are defined as $\Delta_\downarrow = -\omega_{\rm rf}/2 - \omega_\downarrow$, $\Delta_\uparrow = \omega_{\rm rf}/2 - \omega_\uparrow$, $\Delta_e = \omega_p - \omega_e$, and the cavity detunings as $\Delta_a = \omega_p + \omega_{\rm rf}/2 - \omega_a$ and $\Delta_b = \omega_p - \omega_{\rm rf}/2 - \omega_b$. For large detuning Δ_e, the excited state can be adiabatically eliminated and an effective Hamiltonian is obtained for the two pseudospin ground state manifold

$$H_{\{\langle\downarrow|,\langle\uparrow|\}} = H_c + H_d + H_s. \tag{A7.4}$$

The first term of the Hamiltonian accounts for the bare energies of the photon fields, $\Delta_{a(b)}$,

$$H_c = -\hbar\Delta_a\hat{a}^\dagger\hat{a} - \hbar\Delta_b\hat{b}^\dagger\hat{b}. \tag{A7.5}$$

The second term of the Hamiltonian

$$H_d = \left[-\hbar\Delta_\downarrow + \frac{\hbar\Omega_a^2}{\Delta_e} + \frac{\hbar\mathcal{G}_a^2}{\Delta_e}\hat{a}^\dagger\hat{a} + \frac{\hbar\Omega_a g_a}{\Delta_e}(\hat{a}+\hat{a}^\dagger)\right]|\downarrow\rangle\langle\downarrow| \tag{A7.6}$$

$$+ \left[-\hbar\Delta_\uparrow + \frac{\hbar\Omega_b^2}{\Delta_e} + \frac{\hbar\mathcal{G}_b^2}{\Delta_e}\hat{b}^\dagger\hat{b} + \frac{\hbar\Omega_b g_b}{\Delta_e}(\hat{b}+\hat{b}^\dagger)\right]|\uparrow\rangle\langle\uparrow| \tag{A7.7}$$

describes the light-shifts of the two pseudo-spin energy levels induced by the interaction of the atom with the pumping lasers and the cavity modes. In particular, $\Delta_{\downarrow(\uparrow)}$ represent the detunings of the bare atomic energies in the co-rotating frame defined by Eq.(A7.3), and $\Omega_{a(b)}^2/\Delta_e$ are the light shifts induced by the pump. The third terms arise from consecutive absorption and emission processes of cavity photons from the same mode $\sim \hbar\mathcal{G}_{a(b)}^2/\Delta_e$. The fourth terms pump the cavity by scattering photons from the pump inside the optical resonators, shifting the atomic energy levels by $\sim \mathcal{G}_{a(b)}\Omega_{a(b)}/\Delta_e$.

The last term of the Hamiltonian

$$H_s = \hbar\left[\Omega + \frac{\Omega_a\Omega_b}{\Delta_e} + \frac{\Omega_a g_b}{\Delta_e}\hat{b} + \frac{\Omega_b g_a}{\Delta_e}\hat{a}^\dagger + \frac{g_a g_b}{\Delta_e}\hat{a}^\dagger\hat{b}\right]|\downarrow\rangle\langle\uparrow| + \text{H.c.}, \tag{A7.8}$$

includes all the spin-flip processes that can take place either because they are externally driven (as in the case of the radiofrequency Ω in the first term), or because they result from two-photon scattering processes. In particular, the second term is a classical Raman transition induced by the two pumps, the third term is a cavity-mediated Raman transition determined by exchange between the pump and cavity fields, and the fourth term is a Raman transition solely induced by the cavity fields which redistributes photons between the two modes.

From here on, for the sake of simplicity we consider $-\Delta_\downarrow + \Omega_a^2/\Delta_e = -\Delta_\uparrow + \Omega_b^2/\Delta_e$, and use a symmetric configuration of the following parameters: $\eta \equiv \Omega_a g_a/\Delta_e = \Omega_b g_b/\Delta_e$ and $U \equiv g_a^2/\Delta_e = g_b^2/\Delta_e$.

Tight-binding model.—Now that all the relevant transitions are made explicit, we turn to describe the setup for the realization of a two-component Bose-Hubbard model with cavity mediated hopping. Consider an ensemble of many atoms placed in a linear optical cavity with the same configuration pumping described in the previous section, with the internal level structure adiabatically following the center of mass motion of the particles. The atoms are strongly confined to one dimension at one of the shared maxima of intensity of the cavity fields, $\cos(k_a x_j) = \cos(k_b x_j) = 1$. We can thus neglect the motion along the cavity axis (x-direction) and along the pump direction (z-direction), and focus solely on the one-dimensional motion along the y-direction. An accelerated optical lattice with lattice constant λ is placed perpendicularly to the cavity axis (i.e., along y-direction) and strongly confines the atoms at the lattice sites. The acceleration of the optical lattice induces a constant energy gradient, δ, between neighbouring sites which prevents the natural hopping of particles along the lattice direction. By carefully tuning to resonance the frequencies of the pumping lasers, it is possible to tune out of resonance the cavity mediated spin-mixing transitions and considerably simplify the model. In particular, with the resonance conditions, $\omega_{pa} - \omega_a = \delta$ and $\omega_b - \omega_{pb} = \delta$,

only the externally driven first term of Hamiltonian H_s become relevant. Besides, the backward and forward tunneling along the lattice are directionally decoupled for the two pseudo-spin ground states in H_d. For the lower (upper) spin state only the forward (backward) directional tunneling is tuned to resonance with the condition, $\omega_{pa} - \omega_a = \delta$ ($\omega_b - \omega_{pb} = \delta$).

The Hamiltonian in the tight-binding limit reduces to

$$H = -\hbar(\Delta_a - UN_\downarrow)\hat{a}^\dagger\hat{a} - \hbar(\Delta_b - UN_\uparrow)\hat{b}^\dagger\hat{b} - \eta\sum_j(\hat{a}^\dagger\hat{c}^\dagger_{\downarrow,j+1}\hat{c}_{\downarrow,j} + \hat{b}\hat{c}^\dagger_{\uparrow,j+1}\hat{c}_{\uparrow,j} + \text{h.c.}) - \Omega\sum_j(\hat{c}^\dagger_{\downarrow,j}\hat{c}_{\uparrow,j} + \hat{c}^\dagger_{\uparrow,j}\hat{c}_{\downarrow,j}). \tag{A7.9}$$

The second internal ground states of the atoms effectively acts as a synthetic dimension, and the system can be treated as a ladder where the longitudinal tunneling is mediated by the photons, $\hat{a}$ and $\hat{b}$, and the transversal hopping is set by the radiofrequency Ω.

Origin of the synthetic magnetic field.—Consider now the total phase acquired by the atomic-wavefunction of an atom travelling on a closed trajectory along one plaquette of the ladder. The phase of the cavity photon $\hat{a}^\dagger$ is first imprinted on the atom by hopping between neighbouring sites of the lower leg, $|j,\downarrow\rangle$ to $|j+1,\downarrow\rangle$. Hopping along the synthetic direction does not imprint any phase, $|j+1,\downarrow\rangle$ to $|j+1,\uparrow\rangle$. In the reverse direction on the upper leg, $|j+1,\uparrow\rangle$ to $|j,\uparrow\rangle$, the atom will acquire the phase mediated by the second cavity field, $\hat{b}^\dagger$. Finally, the atom comes back to the initial site without acquiring any phase, $|j,\uparrow\rangle$ to $|j,\downarrow\rangle$. It is clear that the total phase acquired by the wave-function in the loop depends on the phases of the two modes, $\hat{a}^\dagger$ and $\hat{b}^\dagger$. This cavity-imprinted phase is responsible for the emergence of a synthetic magnetic field piercing the ladder plaquette.

7.B Derivation of Equations 3 and 4

Derivation of the single-particle energy bands.—From here on, the photon fields will be treated as classical coherent states, $\alpha \equiv \langle a\rangle = |\alpha|e^{i\phi_a}$ and $\beta \equiv \langle b\rangle = |\beta|e^{i\phi_b}$. Within this approximation the non-interacting atomic Hamiltonian can be easily diagonalized in momentum space in the thermodynamic limit, $\hat{c}_{\sigma,j} = \sum_q e^{iqj}\hat{c}_{\sigma,q}$. The Hamiltonian in momentum space reads as

$$H = \sum_q +\hbar U|\alpha|^2\hat{c}^\dagger_{\downarrow,q}\hat{c}_{\downarrow,q} + \hbar U|\beta|^2\hat{c}^\dagger_{\uparrow,q}\hat{c}_{\uparrow,q} - (\hbar\eta|\alpha|e^{-i(q+\phi_\alpha)}\hat{c}^\dagger_{\downarrow,q}\hat{c}_{\downarrow,q} + \hbar\eta|\beta|e^{-i(q-\phi_\beta)}\hat{c}^\dagger_{\uparrow,q}\hat{c}_{\uparrow,q} + \hbar\Omega\hat{c}^\dagger_{\downarrow,q}\hat{c}_{\uparrow,q} + \text{H.c.}), \tag{A7.10}$$

and can be cast in diagonal form, $H = \sum_{q=\pm}\epsilon_{\pm,q}\gamma^\dagger_{\pm,q}\gamma_{\pm,q}$, where the two energy bands are parametrised in terms of the photon amplitudes α and β as

$$\frac{\epsilon_{\pm,q}}{\hbar} = +\frac{U}{2}\left(|\alpha|^2 + |\beta|^2\right) - \eta|\alpha|\cos(q+\phi_\alpha) - \eta|\beta|\cos(q-\phi_\beta) \pm \sqrt{\Omega^2 + \left[\eta\left(|\alpha|\cos(q+\phi_\alpha) - |\beta|\cos(q-\phi_\beta)\right) - \frac{U}{2}\left(|\alpha|^2 - |\beta|^2\right)\right]^2}. \tag{A7.11}$$

By inspection of the band structure, it can be noted that the phases of the cavity fields, ϕ_a and ϕ_b, couple to the atomic momentum as a vector potential and relatively shift the minimum of the original uncoupled tight-binding bands by the value of the magnetic flux piercing one plaquette, $\Phi_B/\Phi_{0B} = \phi_a + \phi_b$, with $\Phi_{0B} = \hbar/\mathcal{Q}$ being the mangnetic flux quantum and $\mathcal{Q}$ the synthetic charge of atom. The presence of a transversal hopping along the ladder rungs hybridizes the two bands, opens a gap and shifts the minima of the band structure. For $|\alpha| = |\beta| = \sqrt{n_{\rm ph}/2}$, in analogy to spin-orbit-coupled BEC the band structure is characterized by a single or double minima, which for a ladder correspond, respectively, to the Meissner and vortex phase. The transition point from the Meissner to the vortex phase is thus expected at the splitting of the single minima of the band structure into two-degenerate minima. Assuming the magnetic flux $\Phi_B/\Phi_{0B} = \phi_a + \phi_b$ is piercing a plaquette of the ladder, the well known threshold from the Meissner to the vortex transition can be cast in terms of the photon number, the pump strength and the magnetic flux as,

$$\eta_c = \frac{\sqrt{2}\Omega}{\left[\sqrt{n_{ph}}\sin(\frac{\Phi_B}{2\Phi_{0B}})\tan(\frac{\Phi_B}{2\Phi_{0B}})\right]_{\eta=\eta_c}}. \tag{A7.12}$$

In our case this is a nonlinear, non-analytical equation, as the photon number intrinsically depends on the pump strength $n_{\rm ph} = n_{\rm ph}(\eta)$. In order to obtain the transition threshold shown in the main text as a dashed red line in Fig. 7.1a, we have compared our numerical results for the effective hopping, $J_{\rm eff} = \eta n_{\rm ph}(\eta)$ with the critical hopping $J_c = \eta_c\sqrt{n_{\rm ph}(\eta_c)}$ – note that the product $\eta_c\sqrt{n_{\rm ph}(\eta_c)}$ is independent of the pump strength and is thus well defined –. The critical threshold is then obtained as the first numerical point for which the tunneling $J_{\rm eff}$ exceed the critical hopping $J > J_{crit}$. The critical pump strength η_c can be then readily extracted back.

Phase locking.—We now derive the steady state value of the photonic phases $\phi_{a(b)}$, from which we show that the induced magnetic flux $\Phi = \phi_a + \phi_b$ acquires a dynamical dependence on the atomic occupation of the two legs. In the adiabatic approximation for cavity field dynamics, the photonic degrees of freedom can be cast in terms of the atomic operators by imposing the steady-state condition on the equations of motion for the cavity amplitudes

$$i\frac{\partial\alpha}{\partial t} = -(\Delta + i\kappa - UN_\downarrow)\alpha - \eta\Theta_\downarrow = 0, \tag{A7.13}$$

$$i\frac{\partial\beta}{\partial t} = -(\Delta + i\kappa - UN_\uparrow)\beta - \eta\Theta_\uparrow^* = 0, \tag{A7.14}$$

where we have defined $\Theta_\sigma = \sum_i \langle c^\dagger_{\sigma,i+1} c_{\sigma,i}\rangle = |\Theta_\sigma| e^{i\phi_\sigma}$ as the average of the spin resolved

hopping operator. By only considering the steady-state solution of these equations,

$$|\alpha| = \frac{\eta}{\sqrt{(\Delta - UN_\downarrow)^2 + \kappa^2}}|\Theta_\downarrow|, \tag{A7.15}$$

$$\phi_a = \arctan\left(\frac{\kappa}{\Delta - UN_\downarrow}\right) + \phi_\downarrow, \tag{A7.16}$$

$$|\beta| = \frac{\eta}{\sqrt{(\Delta - UN_\uparrow)^2 + \kappa^2}}|\Theta_\uparrow|, \tag{A7.17}$$

$$\phi_b = \arctan\left(\frac{\kappa}{\Delta - UN_\uparrow}\right) - \phi_\uparrow, \tag{A7.18}$$

we observe that the phase of the photons $\phi_{a(b)}$ and the phase of the hopping operator $\phi_{\downarrow(\uparrow)}$ are mutually dependent. Due to momentum conservation the initial state population in momentum state is conserved. Then if particles are equally distributed among the legs and prepared in the same momentum state k_0 at $t = 0$, the phase of the translation operator, $\Theta_\sigma(t = 0) = N/2e^{ik_0}$ exactly coincides with the initial momentum state k_0 and will not evolve in time due to the momentum conservation of the non-interacting system.

If we use a uniform momentum distribution, $k_0 = 0$, the stationary phases $\phi_{a(b)}$ are then fixed as we have reported in the main text

$$\phi_a = \arctan\left(\frac{\kappa_a}{\Delta_a - UN_\downarrow}\right), \tag{A7.19}$$

$$\phi_b = \arctan\left(\frac{\kappa_a}{\Delta_b - UN_\uparrow}\right). \tag{A7.20}$$

Note that these phases do not evolve arbitrarily but are fixed by the dissipation constants and the detuning of the cavity fields. The effective detuning of the two cavity modes is shifted by the number of atoms in each leg, which self-consistently adapts to the state of the system. The induced effective gauge potential is therefore entirely dynamical.

7.C Weakly interacting regime

If we focus on the weakly interacting regime of two-body repulsive interactions, the many-body atomic wave-function can be approximated as a product state of single particle wave-functions. We can therefore substitute the atomic operators with their mean-field amplitude $\hat{c}_{i,\sigma} \leftrightarrow \langle \hat{c}_{i,\sigma} \rangle = \psi_{i,\sigma}$, which satisfy the normalization condition $\sum_{i,\sigma} |\psi_{i,\sigma}|^2 = N$. The dynamics of the system is then described by a set of non-linear

equations coupled to the Heisenberg equations of motions for the cavity fields,

$$
\begin{aligned}
i\frac{\partial\psi_{i,\downarrow}}{\partial t} &= U|\alpha|^2\psi_{i,\downarrow} - \eta\alpha\psi_{i+1,\downarrow} - \eta\alpha^*\psi_{i-1,\downarrow} - \Omega\psi_{i\uparrow} + \frac{V}{\hbar}|\psi_{i,\downarrow}|^2\psi_{i,\downarrow} + \frac{\gamma V}{\hbar}|\psi_{i,\uparrow}|^2\psi_{i,\downarrow},\\
i\frac{\partial\psi_{i,\uparrow}}{\partial t} &= U|\beta|^2\psi_{i,\uparrow} - \eta(\beta^*\psi_{i+1,\uparrow} + \beta\psi_{i-1,\uparrow}) - \Omega\psi_{i\downarrow} + \frac{V}{\hbar}|\psi_{i,\uparrow}|^2\psi_{i,\uparrow} + \frac{\gamma V}{\hbar}|\psi_{i,\downarrow}|^2\psi_{i,\uparrow},\\
i\frac{\partial\alpha}{\partial t} &= -(\Delta + i\kappa - UN_\downarrow)\alpha - \eta\sum_i \psi^*_{i+1,\downarrow}\psi_{i,\downarrow},\\
i\frac{\partial\beta}{\partial t} &= -(\Delta + i\kappa - UN_\uparrow)\beta - \eta\sum_i \psi^*_{i,\uparrow}\psi_{i+1,\uparrow}.
\end{aligned}
\tag{A7.21}
$$

In the main text we solved these equations for $V = 1$ and $\gamma = 0.1$ and looked at the long-time dynamics of the atomic and photonic states. As an initial condition we used a uniform density distribution with an equal number of particles distributed in the two legs for the atomic wave-function, and a random initial seed for the photon amplitude α and β. Interspecies contact interactions do not qualitatively change the physics of the system but rather push to higher energies the transition threshold for the photon-imbalanced state and for the onset of the nonlinear dynamical regime. In contrast intraspecies interactions do not affect the transition to the nonlinear dynamical regime, but affect the transition threshold to the photon imbalanced regime.

7.D Derivation of Equation 5

We provide here additional insight on the dynamics of the system at strong pump and for high densities, where the system fails to reach a stationary state. In this region the adiabatic approximation for the cavity modes breaks down and the full time dynamics of the coupled Heisenberg equations of motion must be taken into account. The Heisenberg equations of motion are a set of complex equations and can be cast in terms of the amplitudes $|\alpha|, |\beta|$ and the phases ϕ_a, ϕ_b of the cavity fields:

$$
\frac{\partial|\alpha|}{\partial t} = -\kappa|\alpha| - \frac{J_\downarrow}{2|\alpha|}, \qquad \frac{\partial|\beta|}{\partial t} = -\kappa|\beta| + \frac{J_\uparrow}{2|\beta|}; \tag{A7.22}
$$

$$
\frac{\partial\phi_a}{\partial t} = (\Delta - UN_\downarrow) - \frac{K_\downarrow}{2|\alpha|^2}, \qquad \frac{\partial\phi_b}{\partial t} = (\Delta - UN_\uparrow) - \frac{K_\uparrow}{2|\beta|^2}. \tag{A7.23}
$$

Above we have defined the mean-field average longitudinal kinetic energy for the upper leg, $K_\uparrow = -2\mathrm{Re}(\eta\beta^*\Theta^*_\uparrow)$, and lower leg, $K_\downarrow = -2\mathrm{Re}(\eta\alpha^*\Theta_\downarrow)$, and the mean-field average longitudinal currents on the upper leg, $J_\uparrow = -2\eta\mathrm{Im}(\Theta^*_\uparrow\beta^*)$, and lower leg, $J_\downarrow = 2\eta\mathrm{Im}(\Theta_\downarrow\alpha^*)$, obtained from the current operators defined in the main text.

The equations of motion for the total number of photon, the photon number difference

and the magnetic flux piercing the plaquette can be derived as follows,

$$\frac{\partial n_{\rm ph}}{\partial t} = -2\kappa n_{\rm ph} - J_\downarrow + J_\uparrow, \tag{A7.24}$$

$$\frac{\partial \Delta n_{\rm ph}}{\partial t} = -2\kappa \Delta n_{\rm ph} - J_\downarrow - J_\uparrow, \tag{A7.25}$$

$$\frac{\partial \Phi}{\partial t} = 2\Delta - UN - \frac{n_{\rm ph}\left(K_\uparrow + K_\downarrow\right) + \Delta n_{\rm ph}\left(K_\uparrow - K_\downarrow\right)}{n_{\rm ph}^2 - \Delta n_{\rm ph}^2}. \tag{A7.26}$$

From inspection of the Eqs. (A7.24) and (A7.25) it can be directly seen that the chiral current $J_c = J_\downarrow - J_\uparrow$ and the particle current $J_p = J_\uparrow + J_\downarrow$ act as a source term for the photon number and the photon number difference. The dissipation constant κ is responsible for the decay of their amplitude inside the cavity, as expected. The non-trivial dynamics of the photon number induces a time-dependent leg current and a time-dependent magnetic flux according to Eq. (A7.26). Such phenomena is therefore reminiscent of the behaviour of charged particles in a time-dependent magnetic field where the appearance of an electromotive force (e.m.f), $\mathcal{E} = -\partial\Phi_B(t)/\partial t$, opposes to the time variation of the magnetic flux, $\Phi_B(t)$. The self-emerging electric field generating the e.m.f is oriented along the lattice direction $\hat{y}$ and is given for each leg by the variation of the phase of the corresponding coupled photon field,

$$\frac{\mathcal{Q}}{\hbar}\boldsymbol{\mathcal{E}} = -\frac{\mathcal{Q}}{\hbar}\frac{\partial \boldsymbol{\mathcal{A}}}{\partial t} = -\begin{pmatrix}\dot{\phi}_b \\ \dot{\phi}_a\end{pmatrix}\hat{e}_y, \tag{A7.27}$$

with $\mathcal{A}$ being the vector potential on links between longitudinal lattice sites.

7.E Mesoscopic ladders

In this section, we solve the few-body problem with a self-consistent exact diagonalization method (SC-ED). We assume that the entanglement between atoms and photons is negligible, and treat the photonic degrees of freedom semiclassically, $\hat{a} \to \langle\hat{a}\rangle \to \alpha$ and $\hat{b} \to \langle\hat{b}\rangle \to \beta$. The atomic Hamiltonian $H_{\alpha,\beta}$ is parametrized in terms of the cavity amplitudes and is exactly solved, giving full access to the effects of correlations induced by two-body interactions. Throughout the section we will work with ladders of finite size L and with conserved number of particles N.

Mesoscopic ladders.—We now briefly comment on the role of density correlations for weak pumps, where the physics is dominated by onsite interactions. We study the few particle physics in mesoscopic ladders using a self-consistent exact diagonalization method with periodic boundary conditions [6.20]. Notably, two-particle correlations give rise to a pump-strength threshold at half-filling for the onset of superradiance and appearance of the gauge potential. We identify a transition between a PB-M and a PI-BL state by increasing the pump strength, in agreement with the mean-field results.

For open boundary conditions on the other hand, the current conservation forces the two cavity modes to be populated equally, thus hindering the transition to the photon-

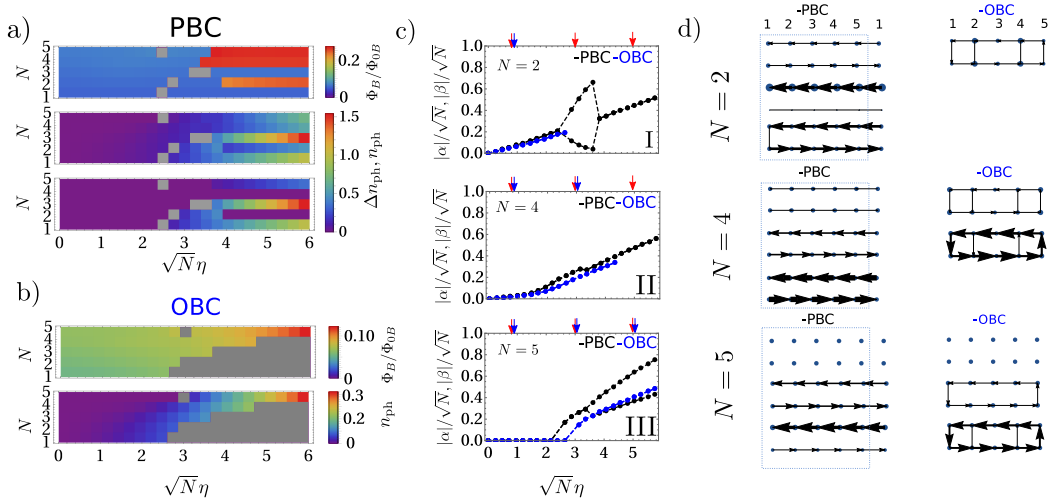

Figure 7.E.1: (a) Converged magnetic flux, total photon number and photon number difference from top to bottom panel, for a ladder of length $L = 5$ and increasing number of particles $N = 1, 2, 3, 4, 5$. (PBC). (b) Converged magnetic flux and total photon number from top to bottom for a ladder of length $L = 5$ (OBC). The photon number difference is not reported for OBC as it vanishes identically in the parameter space. In gray regions of dynamical instability for (a) and (b). (c) Direct comparison of the rescaled photon amplitude of the two modes, $|\alpha|/\sqrt{N}$ and $|\beta|/\sqrt{N}$, for PBC (black) and OBC (blue) for $N = 2, 4, 5$ in I, II and III respectively. The red (blue) arrows on top of each panel show the pumping strengths for which the PBC (OBC) currents are obtained in (d). Other parameters are same as Fig. 7.1 of the main text.

imbalanced regime. However, in contrast to Ref. [6.5], the system is characterized by a steady-state superradiant phase with loop current of the size of the whole system [6.20].

Algorithm.— The SC-ED algorithm searches self-consistent solutions of the atomic ground state by optimizing the values of the light field amplitudes, α and β, which act as variational parameters. The matrix elements of the atomic Hamiltonian, $\mathcal{H}_{nm}(\alpha, \beta) = \langle n| H_{\alpha,\beta} |m\rangle$, are parametrized in terms of the cavity amplitudes, and written in the many-body basis of Fock states $\{|n\rangle\} = |n_{1\downarrow}, n_{2\downarrow}, ..., n_{L\downarrow}, n_{1\uparrow}, n_{2\uparrow}, ..., n_{L\uparrow}\rangle$. Here, each $n_{i\sigma}$ represents the occupation of the lattice site, i, on the upper ($\sigma = \uparrow$) or lower ($\sigma = \downarrow$) leg of the ladder. The algorithm is based on two fundamental steps which are repeated until convergence: diagonalization and calculation of the variational parameters α and β.

The algoritm starts with the initialization of the cavity amplitudes to a random guess, α_0 and β_0. The diagonalization step determines the lowest energy many-body state, $\Psi_{GS}(\alpha_0, \beta_0)$, which corresponds to the atomic Hamiltonian, H_{α_0,β_0}. As a second step, the cavity fields α_{new} and β_{new} are up-dated according to the stationary equations

(A7.13) and (A7.14), which are averaged over the ground state, $\Psi_{GS}(\alpha_0, \beta_0)$. The convergence criteria measures the distance of the new solution to the old one, $c = 1/2\sqrt{(\alpha_{\rm new} - \alpha_0)^2 + (\beta_{\rm new} - \beta_0)^2}$. If the criteria is less than a certain tolerance $t = 10^{-7}$, the algorithm output is given by the converged values of the cavity amplitudes and atomic ground state. If the criteria exceeds the tolerance, new matrix elements $\mathcal{H}_{nm}(\alpha_{\rm new}, \beta_{\rm new})$ are calculated based on the new averages of the cavity amplitudes, $\alpha_{\rm new}$ and $\beta_{\rm new}$. The procedure is repeated until convergence.

Phase diagram.— In Fig. 7.E.1 we report results for a mesoscopic ladder of size $L = 5$ for both periodic (PBC) and open boundary conditions (OBC). The phase diagram is shown in Fig. 7.E.1(a) for PBC and in Fig. 7.E.1(b) for OBC for increasing pumping strength $\sqrt{N}\eta$ and number of particles $1 < N < 5$. Note that, given the small system size and discrete number of particles, the phase diagram obtained in this section can only be compared to longitudinal cuts of Fig. 7.1 in the main text corresponding to densities $n = \{0.1, 0.2, 0.3, 0.4, 0.5\}$. Overall we find good qualitative agreement between the mean field results obtained via time evolution of the Schrodinger equations and the behaviour of the system predicted by SC-ED. In the top panels of Fig. 7.E.1(a) and (b), the converged magnetic flux $\Phi_B/(\Phi_{0B}\pi)$ shows a prominent density dependence in agreement with the mean-field results. In the middle panels, the total photon number $n_{\rm ph}$ gradually increases confirming the absence of a superradiant threshold with the exception of $N = 5$. This is shown in Fig. 7.E.1(c) where the photon amplitudes $|\alpha|/\sqrt{N}$ and $|\beta|/\sqrt{N}$ for $N = 5$ are reported in full (bottom panel). The strong suppression of the photon amplitude at half-filling implies a reduction of the kinetic energy along the ladder direction, thus characterizing a Mott insulating state for the atoms. The bottom panel in Fig. 7.E.1(a) shows the photon number difference $\Delta n_{\rm ph}$ for PBC. We identify a transition from a photon balanced regime ($\Delta n_{\rm ph} = 0$) at weak pumping to a photon imbalanced regime ($\Delta n_{\rm ph} \neq 0$) at strong pumping. The two regimes are characterized by the current patterns shown in Fig. 7.E.1(d), and correspond to the Meissner and biased ladder current pattern also discussed in the main text. Results of $\Delta n_{\rm ph}$ for OBC are not reported in Fig. 7.E.1(b) because the photon number difference vanishes identically. With OBC the boundary enforces current conservation between the two legs, resulting in an equal photon number for the two modes and loop currents of the size of the whole system Fig. 7.E.1(d).

Finite size effect.— We come now to describe some effects that arise due to the finite size of the system. We identify an unusual behavior of the converged ground state for commensurate filling $N = 2$ and $N = 4$: anomalous photon-balanced states are stabilized and exhibit counter-propagating currents similarly to the Meissner phase [Fig. 7.E.1(d)]. For incummensurate filling $N = 1$, $N = 3$ and $N = 5$, the usual photon-balanced vs photon-imbalanced transition is retrieved instead. The unusual behaviour distinguishing odd (incommensurate) to even (commensurate) filling could depend on the finite size of the system and the survival of such phases is thus not guaranteed in the thermodynamic limit.

8 Conclusions and Outlook

This Thesis studied the emergent phenomena arising in ultra-cold cold atomic ensembles coupled to quantized light fields in optical resonators. After introducing the main conceptual and methodological tools which fundamentally build this Thesis, we turned to the describe the properties of the superradiant self-organization of ultra-cold atomic gases coupled to a single cavity mode. This illustrative example not only allowed to introduce powerful numerical and field-integral approaches to study such complex problems, but provided a better understanding of the cooperative phenomena arising from the non-linear coupling of the photons fields and atomic dynamics in a cavity.

Next, we extended the theory for the superradiant self-organization to spinor quantum gases and introduced a generalized multi-level transition scheme that allows to generate long-range photon-mediated interactions that are sensitive to the internal state of the atoms. In such set-ups the interplay between the atomic external and internal degrees of freedom lead to emergence of spin structures which drive the system into the superradiant phase. We have seen an example of the formation of such spin textures for a spinor Fermi gas coupled to two degenerate modes of a ring cavity. Here, the emerging self-ordered state adopts an antiferromangetic character with spin and density waves propagating at a wave-length commensurate with the cavity.

The possibility of controlling both the center of mass motion and the internal state of the atoms provides the opportunity of simulating synthetic dynamic spin-orbit coupling, and artificial gauge fields. To this extent we have thoroughly reviewed the fundamental advantages of cavity-mediated schemes compared to their free space counterpart in the simulation of gauge theories. In these systems the gauge field spontaneously arise in the superradiant phase by the means of the coherent photon build-up, and the non-linear atom-photon coupling allows to generate gauge fields which feel the back-action of the matter they are coupled to, and are therefore fully dynamical.

A first step toward the simulation of a dynamical gauge theory has been addressed by studying the physics of a Fermi gas confined in a two dimensional lattice with cavity induced hopping. The spatial phase profile of the pumping lasers is imprinted onto the atomic wave-function effectively simulating an Aharonov-Bohm phase. In the superradiant regime the interplay between the fractalization of the band structure and the typical threshold behaviour of the phase transition, result in a non-trivial deformation of the energy spectrum compared to the well known Hofstadter spectrum.

By extending the model to a multi-mode cavity for a spinor quantum gas confined in one dimension we were able to render the emerging gauge field density dependent and fully dynamical. The dissipative nature of the cavity is responsible for the stabilization of persistent particle currents. Limit-cycle oscillations of the photon field result in a time-dependent synthetic magnetic flux which in turn induces a synthetic electromotive

force, in a mechanism reminiscent of Faraday's law of induction.

In summary we have shown that the non-linearity of the atom-photon coupling and the intrinsic dissipative nature of the cavity environment lead to new phenomena that cannot be achieved in standard laser generated potentials in free space. Therefore cavity-generated optical potentials are a powerful tool for the quantum simulation of exotic many-body Hamiltonians, leading to emergence of non-trivial states of light and matter.

This Thesis motivates further studies for the development of generalized quantum simulations adopting light-fields in optical resonators. As a potential extension, one could explore the role of interactions for the superradiant self-organization for degenerate strongly interacting Fermi gases. This intriguing problem is also motivated the recent advancement in the experimental community, as the first experiments adopting fermionic species have only recently been brought forward. On this line, the realization of two-body correlations via single photon coupling in fermions could provide a platform for the realization of exotic pairing mechanisms in analogy to high-Tc superconductivity. This could for instance be achieved by dispersively coupling a two particles bound state to a molecular state through a cavity induced photo-association transition. On a more general level similar photo-association transitions could be used to realize a superradiant quantum chemistry simulator. Finally, new pathways are opened for the study of cavity mediated gauge fields: an index of refraction which locally changes throughout the medium would render the dispersive shift of the cavity inhomogeneous, and realize a local density-dependent gauge field. This could be of particular interest for the realization of anionic states in condensed matter systems, and in the quantum simulation of lattice gauge theories. At last turning to non-adiabatic regimes, the exploration of the dynamics of these non-linear quantum systems is an intriguing problem which could lead to the discovery of new stable limit cycles regimes, which could be interpreted as time crystals, or of relevant quantum chaotic regimes.

References for Chapter 1

[1.1] H. K. Onnes, "The condensation of Helium," *Nature*, vol. 77, no. 2008, pp. 581–581, 1908.

[1.2] H. Kamerlingh Onnes, "The superconductivity of mercury," *Comm. Phys. Lab. Univ. Leiden*, vol. 122, pp. 122–124, 1911.

[1.3] A. Einstein, "Quantentheorie des einatomigen idealen Gases. Zweite Abhandlung," Dec. 2005.

[1.4] E. Fermi, "Sulla quantizzazione del gas perfetto monoatomico," *Rendiconti Lincei*, vol. 145, 1926.

[1.5] P. Dirac, "On the theory of quantum mechanics," *Proc. R. Soc. Lond.*, vol. 112, pp. 661–677, Oct. 1926.

[1.6] W. Keesom, "On the jump in the expansion coefficient of liquid helium in passing the lambda point," *Verhandlingen der Koninklijke Akademie van Wetenschappen (Amsterdam)*, vol. 36, pp. 147–152, 1933.

[1.7] P. Kapitza, "Viscosity of liquid Helium below the λ-point," *Nature*, vol. 141, no. 3558, pp. 74–74, 1938.

[1.8] F. London, "The λ-phenomenon of liquid Helium and the Bose-Einstein degeneracy," *Nature*, vol. 141, no. 3571, pp. 643–644, 1938.

[1.9] C. E. Hecht, "The possible superfluid behaviour of hydrogen atom gases and liquids," *Physica*, vol. 25, 1959.

[1.10] M. H. Anderson, J. R. Ensher, M. R. Matthews, C. E. Wieman, and E. A. Cornell, "Observation of Bose-Einstein Condensation in a dilute atomic vapor," *Science*, vol. 269, pp. 198–201, Jul. 1995.

[1.11] K. B. Davis, M.-O. Mewes, M. R. Andrews, N. Van Druten, D. Durfee, D. Kurn, and W. Ketterle, "Bose-Einstein condensation in a gas of sodium atoms," *Phys. Rev. Lett*, vol. 75, no. 22, p. 3969, 1995.

[1.12] B. DeMarco and D. S. Jin, "Onset of Fermi degeneracy in a trapped atomic gas," *Science*, vol. 285, pp. 1703–1706, Sep. 1999.

[1.13] S. Giorgini, L. P. Pitaevskii, and S. Stringari, "Theory of ultracold atomic Fermi gases," *Rev. Mod. Phys.*, vol. 80, no. 4, p. 1215, 2008.

[1.14] I. Bloch, J. Dalibard, and W. Zwerger, "Many-body physics with ultracold gases," *Rev. Mod. Phys.*, vol. 80, no. 3, p. 885, 2008.

[1.15] I. Bloch, J. Dalibard, and S. Nascimbène, "Quantum simulations with ultracold quantum gases," *Nat. Phys.*, vol. 8, pp. 267–276, apr 2012.

[1.16] R. P. Feynman, "Simulating physics with computers," in *Feynman and computation*, pp. 133–153, CRC Press, 2018.

[1.17] S. Inouye, M. Andrews, J. Stenger, H.-J. Miesner, D. M. Stamper-Kurn, and W. Ketterle, "Observation of Feshbach resonances in a Bose-Einstein condensate," *Nature*, vol. 392, no. 6672, pp. 151–154, 1998.

[1.18] T. Loftus, C. A. Regal, C. Ticknor, J. L. Bohn, and D. S. Jin, "Resonant control of elastic collisions in an optically trapped Fermi gas of atoms," *Phys. Rev. Lett*, vol. 88, no. 17, p. 173201, 2002.

[1.19] M. Greiner, O. Mandel, T. Esslinger, T. W. Hänsch, and I. Bloch, "Quantum phase transition from a superfluid to a mott insulator in a gas of ultracold atoms," *Nature*, vol. 415, no. 6867, pp. 39–44, 2002.

[1.20] M. Greiner, C. A. Regal, and D. S. Jin, "Emergence of a molecular Bose–Einstein condensate from a Fermi gas," *Nature*, vol. 426, no. 6966, pp. 537–540, 2003.

[1.21] M. W. Zwierlein, J. R. Abo-Shaeer, A. Schirotzek, C. H. Schunck, and W. Ketterle, "Vortices and superfluidity in a strongly interacting Fermi gas," *Nature*, vol. 435, no. 7045, pp. 1047–1051, 2005.

[1.22] M. Holland, S. Kokkelmans, M. L. Chiofalo, and R. Walser, "Resonance superfluidity in a quantum degenerate Fermi gas," *Phys. Rev. Lett*, vol. 87, no. 12, p. 120406, 2001.

[1.23] I. Bloch, "Ultracold quantum gases in optical lattices," *Nature*, vol. 1, pp. 23–30, Oct 2005.

[1.24] C. Cohen-Tannoudji and D. Guéry-Odelin, *Advances in Atomic Physics*. World Scientific, sep 2011.

[1.25] H. Tanji-Suzuki, I. D. Leroux, M. H. Schleier-Smith, M. Cetina, A. T. Grier, J. Simon, and V. Vuletić, "Interaction between atomic ensembles and optical resonators," in *Advances In Atomic, Molecular, and Optical Physics*, pp. 201–237, Elsevier, 2011.

[1.26] H. Ritsch, P. Domokos, F. Brennecke, and T. Esslinger, "Cold atoms in cavity-generated dynamical optical potentials," *Rev. Mod. Phys.*, vol. 85, pp. 553–601, Apr 2013.

[1.27] P. Domokos and H. Ritsch, "Mechanical effects of light in optical resonators," *J. Opt. Soc. Am. B*, vol. 20, no. 5, pp. 1098–1130, 2003.

[1.28] R. H. Dicke, "Coherence in spontaneous radiation processes," *Phys. Rev.*, vol. 93, pp. 99–110, Jan 1954.

[1.29] F. Brennecke, T. Donner, S. Ritter, T. Bourdel, M. Köhl, and T. Esslinger, "Cavity QED with a Bose–Einstein condensate," *Nature*, vol. 450, no. 7167, pp. 268–271, 2007.

[1.30] K. Baumann, C. Guerlin, F. Brennecke, and T. Esslinger, "Dicke quantum phase transition with a superfluid gas in an optical cavity," *Nature*, vol. 464, pp. 1301–1306, apr 2010.

[1.31] K. Baumann, R. Mottl, F. Brennecke, and T. Esslinger, "Exploring symmetry breaking at the Dicke quantum phase transition," *Phys. Rev. Lett.*, vol. 107, p. 140402, Sep 2011.

[1.32] J. Keeling, M. Bhaseen, and B. Simons, "Fermionic superradiance in a transversely pumped optical cavity," *Phys. Rev. Lett*, vol. 112, no. 14, p. 143002, 2014.

[1.33] F. Piazza and P. Strack, "Umklapp superradiance with a collisionless quantum degenerate Fermi gas," *Phys. Rev. Lett.*, vol. 112, p. 143003, Apr 2014.

[1.34] Y. Chen, Z. Yu, and H. Zhai, "Superradiance of degenerate Fermi gases in a cavity," *Phys. Rev. Lett*, vol. 112, no. 14, p. 143004, 2014.

[1.35] R. E. Peierls, *Quantum Theory of Solids*. Oxford University Press, Feb. 2001.

[1.36] J. Léonard, A. Morales, P. Zupancic, T. Esslinger, and T. Donner, "Supersolid formation in a quantum gas breaking a continuous translational symmetry," *Nature*, vol. 543, pp. 87–90, Mar 2017.

[1.37] J. Léonard, A. Morales, P. Zupancic, T. Donner, and T. Esslinger, "Monitoring and manipulating Higgs and Goldstone modes in a supersolid quantum gas," *Science*, vol. 358, pp. 1415–1418, Dec. 2017.

[1.38] J. Lang, F. Piazza, and W. Zwerger, "Collective excitations and supersolid behavior of bosonic atoms inside two crossed optical cavities," *New J. Phys.*, vol. 19, no. 12, p. 123027, 2017.

[1.39] F. Mivehvar, S. Ostermann, F. Piazza, and H. Ritsch, "Driven-dissipative supersolid in a ring cavity," *Phys. Rev. Lett.*, vol. 120, p. 123601, Mar 2018.

[1.40] S. C. Schuster, P. Wolf, D. Schmidt, S. Slama, and C. Zimmermann, "Pinning transition of Bose-Einstein condensates in optical ring resonators," *Phys. Rev. Lett.*, vol. 121, p. 223601, Nov 2018.

[1.41] M. Landini, N. Dogra, K. Kroeger, L. Hruby, T. Donner, and T. Esslinger, "Formation of a spin texture in a quantum gas coupled to a cavity," *Phys. Rev. Lett.*, vol. 120, p. 223602, May 2018.

[1.42] R. M. Kroeze, Y. Guo, V. D. Vaidya, J. Keeling, and B. L. Lev, "Spinor self-ordering of a quantum gas in a cavity," *Phys. Rev. Lett.*, vol. 121, p. 163601, Oct 2018.

[1.43] F. Mivehvar, F. Piazza, and H. Ritsch, "Disorder-driven density and spin self-ordering of a Bose-Einstein condensate in a cavity," *Phys. Rev. Lett.*, vol. 119, p. 063602, Aug 2017.

[1.44] J.-S. Pan, X.-J. Liu, W. Zhang, W. Yi, and G.-C. Guo, "Topological superradiant states in a degenerate Fermi gas," *Phys. Rev. Lett.*, vol. 115, p. 045303, Jul 2015.

[1.45] D. Yu, J.-S. Pan, X.-J. Liu, W. Zhang, and W. Yi, "Topological superradiant state in Fermi gases with cavity induced spin–orbit coupling," *Front. Phys.*, vol. 13, Jul 2017.

[1.46] E. Colella, R. Citro, M. Barsanti, D. Rossini, and M.-L. Chiofalo, "Quantum phases of spinful Fermi gases in optical cavities," *Phys. Rev. B*, vol. 97, p. 134502, Apr 2018.

[1.47] E. Colella, M. Chiofalo, M. Barsanti, D. Rossini, and R. Citro, "Fluid structure of 1d spinful Fermi gases with long-range interactions," *J. Phys. B: At. Mol. Opt. Phys.*, vol. 52, no. 21, p. 215301, 2019.

[1.48] F. Schlawin and D. Jaksch, "Cavity-mediated unconventional pairing in ultracold fermionic atoms," *Phys. Rev. Lett*, vol. 123, no. 13, p. 133601, 2019.

[1.49] A. Chakraborty and F. Piazza, "Long-range photon fluctuations enhance photon-mediated electron pairing and superconductivity," *Phys. Rev. Lett.*, vol. 127, p. 177002, Oct 2021.

[1.50] X. Zhang, Y. Chen, Z. Wu, J. Wang, J. Fan, S. Deng, and H. Wu, "Observation of a superradiant quantum phase transition in an intracavity degenerate Fermi gas," vol. 373, pp. 1359–1362, Sept. 2021.

[1.51] K. Roux, H. Konishi, V. Helson, and J.-P. Brantut, "Strongly correlated fermions strongly coupled to light," *Nat. Comm.*, vol. 11, Jun 2020.

[1.52] K. Roux, V. Helson, H. Konishi, and J. P. Brantut, "Cavity-assisted preparation and detection of a unitary Fermi gas," *New J. Phys.*, vol. 23, p. 043029, Apr. 2021.

[1.53] H. Konishi, K. Roux, V. Helson, and J.-P. Brantut, "Universal pair polaritons in a strongly interacting Fermi gas," *Nature*, vol. 596, pp. 509–513, Aug. 2021.

[1.54] A. Sheikhan, F. Brennecke, and C. Kollath, "Cavity-induced generation of non-trivial topological states in a two-dimensional Fermi gas," *Phys. Rev. A*, vol. 94, p. 061603, Dec. 2016.

References for Chapter 2

[2.1] J. Maxwell, *A treatise on electricity and magnetism*. New York: Dover Publications, 1954.

[2.2] E. F. Nichols and G. F. Hull, "The pressure due to radiation," *Proc. Am. Acad. Arts Sci.*, vol. 38, no. 20, p. 559, 1903.

[2.3] R. Frisch, "Experimenteller nachweis des einsteinschen strahlungsrückstoßes," *Z. Phys.*, vol. 86, pp. 42–48, Jan. 1933.

[2.4] T. H. Maiman, "Stimulated optical radiation in Ruby," *Nature*, vol. 187, pp. 493–494, Aug. 1960.

[2.5] H. Tanji-Suzuki, I. D. Leroux, M. H. Schleier-Smith, M. Cetina, A. T. Grier, J. Simon, and V. Vuletić, "Interaction between atomic ensembles and optical resonators," in *Advances in atomic, molecular, and optical physics*, pp. 201–237, Elsevier, 2011.

[2.6] H. Ritsch, P. Domokos, F. Brennecke, and T. Esslinger, "Cold atoms in cavity-generated dynamical optical potentials," *Rev. Mod. Phys.*, vol. 85, pp. 553–601, Apr 2013.

[2.7] Feynman, Leighton, and Sands, *Feynman lectures on physics, volume 2 (the new millennium edition*. New York: Basic Books, 2013.

[2.8] A. E. Siegman, *Lasers*. Mill Valley, Calif: University Science Books, 1986.

[2.9] Y. Guo, V. D. Vaidya, R. M. Kroeze, R. A. Lunney, B. L. Lev, and J. Keeling, "Emergent and broken symmetries of atomic self-organization arising from Gouy phase shifts in multimode cavity QED," *Phys. Rev. A*, vol. 99, May 2019.

[2.10] F. Mivehvar, F. Piazza, T. Donner, and H. Ritsch, "Cavity qed with quantum gases: new paradigms in many-body physics," *Ad. Phys.*, vol. 70, no. 1, pp. 1–153, 2021.

[2.11] W. Keesom, "On the jump in the expansion coefficient of liquid helium in passing the lambda point," *Verhandlingen der Koninklijke Akademie van Wetenschappen (Amsterdam)*, vol. 36, pp. 147–152, 1933.

[2.12] G. Jaeger, "The Ehrenfest classification of phase transitions: introduction and evolution," *Archive for history of exact sciences*, vol. 53, no. 1, pp. 51–81, 1998.

[2.13] A. Altland and B. D. Simons, *Condensed matter field theory*. Cambridge university press, 2010.

[2.14] G. Mahan, *Many-Particle Physics*. Boston, MA: Springer US, 2000.

[2.15] R. H. Dicke, "Coherence in spontaneous radiation processes," *Phys. Rev.*, vol. 93, pp. 99–110, Jan 1954.

[2.16] P. Kirton, M. M. Roses, J. Keeling, and E. G. D. Torre, "Introduction to the Dicke model: From equilibrium to nonequilibrium, and vice versa," *Advanced Quantum Technologies*, vol. 2, p. 1800043, Oct. 2018.

[2.17] F. Piazza and P. Strack, "Umklapp superradiance with a collisionless quantum degenerate fermi gas," *Phys. Rev. Lett.*, vol. 112, p. 143003, Apr 2014.

[2.18] J. Lindhard, "On the properties of a gas of charged particles," *Kgl. Danske Videnskab. Selskab Mat.-fys. Medd.*

[2.19] B. Mihaila, "Lindhard function of a d-dimensional fermi gas," *arXiv preprint arXiv:1111.5337*, 2011.

[2.20] J. Keeling, M. Bhaseen, and B. Simons, "Fermionic superradiance in a transversely pumped optical cavity," *Phys. Rev. Lett*, vol. 112, no. 14, p. 143002, 2014.

[2.21] A. T. Black, H. W. Chan, and V. Vuletić, "Observation of collective friction forces due to spatial self-organization of atoms: From Rayleigh to Bragg scattering," *Phys. Rev. Lett.*, vol. 91, p. 203001, Nov 2003.

[2.22] K. Baumann, C. Guerlin, F. Brennecke, and T. Esslinger, "Dicke quantum phase transition with a superfluid gas in an optical cavity," *Nature*, vol. 464, pp. 1301–1306, apr 2010.

[2.23] K. Baumann, R. Mottl, F. Brennecke, and T. Esslinger, "Exploring symmetry breaking at the Dicke quantum phase transition," *Phys. Rev. Lett.*, vol. 107, p. 140402, Sep 2011.

[2.24] R. Mottl, F. Brennecke, K. Baumann, R. Landig, T. Donner, and T. Esslinger, "Roton-type mode softening in a quantum gas with cavity-mediated long-range interactions," *Science*, vol. 336, pp. 1570–1573, Jun 2012.

References for Chapter 3

[3.1] C. Cohen-Tannoudji and D. Guéry-Odelin, *Advances in Atomic Physics*. World Scientific, Sep. 2011.

[3.2] F. Mivehvar, F. Piazza, T. Donner, and H. Ritsch, "Cavity qed with quantum gases: new paradigms in many-body physics," *Advances in Physics*, vol. 70, no. 1, pp. 1–153, 2021.

[3.3] F. Mivehvar, H. Ritsch, and F. Piazza, "Cavity-quantum-electrodynamical toolbox for quantum magnetism," *Phys. Rev. Lett.*, vol. 122, p. 113603, Mar. 2019.

[3.4] S. Safaei, O. E. Müstecaplıoğlu, and B. Tanatar, "Raman superradiance and spin lattice of ultracold atoms in optical cavities," vol. 15, p. 083037, Aug. 2013.

[3.5] E. Colella, S. Ostermann, W. Niedenzu, F. Mivehvar, and H. Ritsch, "Antiferromagnetic self-ordering of a fermi gas in a ring cavity," *New J. Phys.*, vol. 21, no. 4, p. 043019, 2019.

[3.6] S. Ostermann, H.-W. Lau, H. Ritsch, and F. Mivehvar, "Cavity-induced emergent topological spin textures in a Bose–Einstein condensate," *New J. Phys*, vol. 21, p. 013029, Jan. 2019.

[3.7] S. Ostermann, H. Ritsch, and F. Mivehvar, "Many-body phases of a planar Bose-Einstein condensate with cavity-induced spin-orbit coupling," *Phys. Rev. A*, vol. 103, p. 023302, Feb 2021.

[3.8] N. Masalaeva, W. Niedenzu, F. Mivehvar, and H. Ritsch, "Spin and density self-ordering in dynamic polarization gradients fields," *Phys. Rev. R*, vol. 3, Feb. 2021.

[3.9] A. Chiocchetta, D. Kiese, C. P. Zelle, F. Piazza, and S. Diehl, "Cavity-induced quantum spin liquids," *Nat. Comm.*, vol. 12, Oct. 2021.

[3.10] M. P. Baden, K. J. Arnold, A. L. Grimsmo, S. Parkins, and M. D. Barrett, "Realization of the Dicke model using cavity-assisted Raman transitions," *Phys. Rev. Lett.*, vol. 113, p. 020408, Jul 2014.

[3.11] R. M. Kroeze, Y. Guo, V. D. Vaidya, J. Keeling, and B. L. Lev, "Spinor self-ordering of a quantum gas in a cavity," *Phys. Rev. Lett.*, vol. 121, p. 163601, Oct 2018.

References for Chapter 4

[4.1] E. Noether, "Invariante variationsprobleme," *Nachrichten von der Gesellschaft der Wissenschaften zu Göttingen, Mathematisch-Physikalische Klasse*, vol. 1918, pp. 235–257, 1918.

[4.2] A. Beekman, L. Rademaker, and J. van Wezel, "An introduction to spontaneous symmetry breaking," *SciPost Phys. Lect. Notes*, Dec. 2019.

[4.3] J. D. Jackson and L. B. Okun, "Historical roots of gauge invariance," *Rev. Mod. Phys.*, vol. 73, pp. 663–680, Sept. 2001.

[4.4] E. Schrödinger, "Quantisierung als eigenwertproblem," *Ann. Phys.*, vol. 385, no. 13, pp. 437–490, 1926.

[4.5] V. Fock, "Über die invariante form der wellen- und der bewegungsgleichungen für einen geladenen massenpunkt," *Z. Phys.*, vol. 39, pp. 226–232, Feb. 1926.

[4.6] J. Dalibard, F. Gerbier, G. Juzeliūnas, and P. Öhberg, "Colloquium: Artificial gauge potentials for neutral atoms," *Rev. Mod. Phys.*, vol. 83, pp. 1523–1543, Nov 2011.

[4.7] Y. Aharonov and D. Bohm, "Significance of electromagnetic potentials in the quantum theory," *Phys. Rev.*, vol. 115, pp. 485–491, Aug 1959.

[4.8] A. Tonomura, T. Matsuda, R. Suzuki, A. Fukuhara, N. Osakabe, H. Umezaki, J. Endo, K. Shinagawa, Y. Sugita, and H. Fujiwara, "Observation of Aharonov-Bohm effect by electron holography," *Phys. Rev. Lett.*, vol. 48, pp. 1443–1446, May 1982.

[4.9] I. Bloch, J. Dalibard, and S. Nascimbène, "Quantum simulations with ultracold quantum gases," *Nat. Phys.*, vol. 8, pp. 267–276, apr 2012.

[4.10] J. Hubbard, "Electron correlations in narrow energy bands," *Proc. R. Soc. Lond. A*, vol. 276, pp. 238–257, Nov. 1963.

[4.11] R. Peierls, "Zur theorie des diamagnetismus von leitungselektronen," *Z. Phys.*, vol. 80, pp. 763–791, Nov. 1933.

[4.12] D. R. Hofstadter, "Energy levels and wave functions of bloch electrons in rational and irrational magnetic fields," *Phys. Rev. B*, vol. 14, pp. 2239–2249, Sep 1976.

[4.13] L. Landau, "Diamagnetismus der metalle," *Z. Phys.*, vol. 64, pp. 629–637, Sept. 1930.

[4.14] X. Ni, K. Chen, M. Weiner, D. J. Apigo, C. Prodan, A. Alù, E. Prodan, and A. B. Khanikaev, "Hofstadter butterfly and topological edge states in reconfigurable quasi-periodic acoustic crystals," *Nature*, vol. 2, June 2019.

[4.15] A. L. Fetter, "Rotating trapped Bose-Einstein condensates," *Rev. Mod. Phys.*, vol. 81, no. 2, p. 647, 2009.

[4.16] V. Schweikhard, I. Coddington, P. Engels, V. P. Mogendorff, and E. A. Cornell, "Rapidly rotating Bose-Einstein condensates in and near the lowest Landau level," *Phys. Rev. Lett*, vol. 92, no. 4, p. 040404, 2004.

[4.17] M. Andersen, C. Ryu, P. Cladé, V. Natarajan, A. Vaziri, K. Helmerson, and W. D. Phillips, "Quantized rotation of atoms from photons with orbital angular momentum," *Phys. Rev. Lett*, vol. 97, no. 17, p. 170406, 2006.

[4.18] M. Aidelsburger, M. Atala, S. Nascimbène, S. Trotzky, Y.-A. Chen, and I. Bloch, "Experimental realization of strong effective magnetic fields in an optical lattice," *Phys. Rev. Lett.*, vol. 107, p. 255301, Dec 2011.

[4.19] M. Aidelsburger, M. Atala, M. Lohse, J. T. Barreiro, B. Paredes, and I. Bloch, "Realization of the Hofstadter hamiltonian with ultracold atoms in optical lattices," *Phys. Rev. Lett.*, vol. 111, p. 185301, Oct 2013.

[4.20] M. Aidelsburger, M. Lohse, C. Schweizer, M. Atala, J. T. Barreiro, S. Nascimbène, N. R. Cooper, I. Bloch, and N. Goldman, "Measuring the Chern number of Hofstadter bands with ultracold bosonic atoms," *Nat. Phys.*, vol. 11, pp. 162–166, Dec. 2014.

[4.21] M. Atala, M. Aidelsburger, M. Lohse, J. T. Barreiro, B. Paredes, and I. Bloch, "Observation of chiral currents with ultracold atoms in bosonic ladders," vol. 10, pp. 588–593, July 2014.

[4.22] S. Greschner, G. Sun, D. Poletti, and L. Santos, "Density-dependent synthetic gauge fields using periodically modulated interactions," *Phys. Rev. Lett.*, vol. 113, p. 215303, Nov 2014.

[4.23] F. Görg, K. Sandholzer, J. Minguzzi, R. Desbuquois, M. Messer, and T. Esslinger, "Realization of density-dependent Peierls phases to engineer quantized gauge fields coupled to ultracold matter," *Nat. Phys.*, vol. 15, pp. 1161–1167, Nov 2019.

[4.24] C. Schweizer, F. Grusdt, M. Berngruber, L. Barbiero, E. Demler, N. Goldman, I. Bloch, and M. Aidelsburger, "Floquet approach to $\mathbb{Z}2$ lattice gauge theories with ultracold atoms in optical lattices," *Nat. Phys.*, vol. 15, pp. 1168–1173, Sept. 2019.

[4.25] V. Lienhard, P. Scholl, S. Weber, D. Barredo, S. de Léséleuc, R. Bai, N. Lang, M. Fleischhauer, H. P. Büchler, T. Lahaye, and A. Browaeys, "Realization of a density-dependent Peierls phase in a synthetic, spin-orbit coupled Rydberg system," *Phys. Rev. X*, vol. 10, p. 021031, May 2020.

[4.26] C. Kollath, A. Sheikhan, S. Wolff, and F. Brennecke, "Ultracold Fermions in a Cavity-Induced Artificial Magnetic Field," *Phys. Rev. Lett.*, vol. 116, p. 060401, Feb 2016.

[4.27] A. Sheikhan, F. Brennecke, and C. Kollath, "Cavity-induced generation of non-trivial topological states in a two-dimensional fermi gas," *Phys. Rev. A*, vol. 94, p. 061603, Dec 2016.

[4.28] E. Colella, F. Mivehvar, F. Piazza, and H. Ritsch, "Hofstadter butterfly in a cavity-induced dynamic synthetic magnetic field," *Phys. Rev. B*, vol. 100, p. 224306, Dec 2019.

[4.29] W. Zheng and N. R. Cooper, "Superradiance induced particle flow via dynamical gauge coupling," *Phys. Rev. Lett.*, vol. 117, p. 175302, Oct 2016.

[4.30] K. E. Ballantine, B. L. Lev, and J. Keeling, "Meissner-like effect for a synthetic gauge field in multimode cavity QED," *Phys. Rev. Lett.*, vol. 118, p. 045302, Jan 2017.

References for Chapter 5

[5.1] I. Bloch, J. Dalibard, and S. Nascimbène, "Quantum simulations with ultracold quantum gases," *Nat. Phys.*, vol. 8, pp. 267–276, apr 2012.

[5.2] C. Cohen-Tannoudji and D. Guéry-Odelin, *Advances in Atomic Physics*. World Scientific, sep 2011.

[5.3] M. Lewenstein, A. Sanpera, and V. Ahufinger, *Ultracold Atoms in Optical Lattices*. Oxford University Press, mar 2012.

[5.4] N. Goldman, J. C. Budich, and P. Zoller, "Topological quantum matter with ultracold gases in optical lattices," *Nat. Phys.*, vol. 12, pp. 639–645, jul 2016.

[5.5] H. Zhai, "Degenerate quantum gases with spin–orbit coupling: a review," *Rep. Prog. Phys.*, vol. 78, p. 026001, feb 2015.

[5.6] D. Kruse, M. Ruder, J. Benhelm, C. von Cube, C. Zimmermann, P. W. Courteille, T. Elsässer, B. Nagorny, and A. Hemmerich, "Cold atoms in a high-Q ring cavity," *Phys. Rev. A*, vol. 67, p. 051802, May 2003.

[5.7] H. Ritsch, P. Domokos, F. Brennecke, and T. Esslinger, "Cold atoms in cavity-generated dynamical optical potentials," *Rev. Mod. Phys.*, vol. 85, pp. 553–601, Apr 2013.

[5.8] P. Wang, Z.-Q. Yu, Z. Fu, J. Miao, L. Huang, S. Chai, H. Zhai, and J. Zhang, "Spin-orbit coupled degenerate Fermi gases," *Phys. Rev. Lett.*, vol. 109, p. 095301, Aug 2012.

[5.9] I. B. Mekhov and H. Ritsch, "Quantum optics with ultracold quantum gases: towards the full quantum regime of the light–matter interaction," *J. Phys. B: At. Mol. Opt. Phys.*, vol. 45, no. 10, p. 102001, 2012.

[5.10] J. Léonard, A. Morales, P. Zupancic, T. Esslinger, and T. Donner, "Supersolid formation in a quantum gas breaking a continuous translational symmetry," *Nature*, vol. 543, pp. 87–90, mar 2017.

[5.11] J. Kohler, J. A. Gerber, E. Dowd, and D. M. Stamper-Kurn, "Negative-mass instability of the spin and motion of an atomic gas driven by optical cavity backaction," *Phys. Rev. Lett.*, vol. 120, p. 013601, Jan 2018.

[5.12] E. J. Davis, G. Bentsen, L. Homeier, T. Li, and M. H. Schleier-Smith, "Photon-mediated spin-exchange dynamics of spin-1 atoms," *Phys. Rev. Lett.*, vol. 122, p. 010405, Jan 2019.

[5.13] R. M. Kroeze, Y. Guo, V. D. Vaidya, J. Keeling, and B. L. Lev, "Spinor self-ordering of a quantum gas in a cavity," *Phys. Rev. Lett.*, vol. 121, p. 163601, Oct 2018.

[5.14] M. Landini, N. Dogra, K. Kroeger, L. Hruby, T. Donner, and T. Esslinger, "Formation of a spin texture in a quantum gas coupled to a cavity," *Phys. Rev. Lett.*, vol. 120, p. 223602, May 2018.

[5.15] M. Wolke, J. Klinner, H. Kessler, and A. Hemmerich, "Cavity cooling below the recoil limit," *Science*, vol. 337, pp. 75–78, jul 2012.

[5.16] R. M. Sandner, W. Niedenzu, and H. Ritsch, "Subrecoil cavity cooling towards degeneracy: A numerical study," *EPL (Europhys. Lett.)*, vol. 104, p. 43001, nov 2013.

[5.17] V. D. Vaidya, Y. Guo, R. M. Kroeze, K. E. Ballantine, A. J. Kollár, J. Keeling, and B. L. Lev, "Tunable-range, photon-mediated atomic interactions in multimode cavity QED," *Phys. Rev. X*, vol. 8, p. 011002, Jan 2018.

[5.18] F. Mivehvar and D. L. Feder, "Synthetic spin-orbit interactions and magnetic fields in ring-cavity QED," *Phys. Rev. A*, vol. 89, p. 013803, Jan 2014.

[5.19] K. E. Ballantine, B. L. Lev, and J. Keeling, "Meissner-like effect for a synthetic gauge field in multimode cavity QED," *Phys. Rev. Lett.*, vol. 118, p. 045302, Jan 2017.

[5.20] C.-M. Halati, A. Sheikhan, and C. Kollath, "Cavity-induced artificial gauge field in a Bose-Hubbard ladder," *Phys. Rev. A*, vol. 96, p. 063621, Dec 2017.

[5.21] J. Léonard, A. Morales, P. Zupancic, T. Donner, and T. Esslinger, "Monitoring and manipulating higgs and goldstone modes in a supersolid quantum gas," *Science*, vol. 358, pp. 1415–1418, dec 2017.

[5.22] C. Georges, J. G. Cosme, L. Mathey, and A. Hemmerich, "Light-induced coherence in an atom-cavity system," *Phys. Rev. Lett.*, vol. 121, p. 220405, Nov 2018.

[5.23] F. Mivehvar, F. , and H. Ritsch, "Disorder-driven density and spin self-ordering of a Bose-Einstein condensate in a cavity," *Phys. Rev. Lett.*, vol. 119, p. 063602, Aug 2017.

[5.24] S. Ostermann, H.-W. Lau, H. Ritsch, and F. Mivehvar, "Cavity-induced emergent topological spin textures in a Bose–Einstein condensate," *New J. Phys.*, vol. 21, p. 013029, Jan. 2019.

[5.25] V. Torggler, S. Krämer, and H. Ritsch, "Quantum annealing with ultracold atoms in a multimode optical resonator," *Phys. Rev. A*, vol. 95, p. 032310, Mar 2017.

[5.26] F. Piazza and P. Strack, "Umklapp superradiance with a collisionless quantum degenerate Fermi gas," *Phys. Rev. Lett.*, vol. 112, p. 143003, Apr 2014.

[5.27] Y. Chen, Z. Yu, and H. Zhai, "Superradiance of degenerate Fermi gases in a cavity," *Phys. Rev. Lett.*, vol. 112, p. 143004, Apr 2014.

[5.28] F. Mivehvar, H. Ritsch, and F. Piazza, "Superradiant topological Peierlsinsulator inside an optical cavity," *Phys. Rev. Lett.*, vol. 118, p. 073602, Feb 2017.

[5.29] A. Sheikhan, F. Brennecke, and C. Kollath, "Cavity-induced generation of non-trivial topological states in a two-dimensional Fermi gas," *Phys. Rev. A*, vol. 94, p. 061603, Dec 2016.

[5.30] E. Colella, R. Citro, M. Barsanti, D. Rossini, and M.-L. Chiofalo, "Quantum phases of spinful Fermi gases in optical cavities," *Phys. Rev. B*, vol. 97, p. 134502, Apr 2018.

[5.31] A. Sheikhan and C. Kollath, "Cavity-induced superconducting and $4k_F$ charge-density-wave states," *Phys. Rev. A*, vol. 99, p. 053611, May 2019.

[5.32] J. Fan, X. Zhou, W. Zheng, W. Yi, G. Chen, and S. Jia, "Magnetic order in a Fermi gas induced by cavity-field fluctuations," *Phys. Rev. A*, vol. 98, p. 043613, Oct 2018.

[5.33] Y. Feng, K. Zhang, J. Fan, F. Mei, G. Chen, and S. Jia, "Quantum mixed phases of a two-dimensional polarized degenerate fermi gas in an optical cavity," *Sci. Rep.*, vol. 7, no. 1, pp. 1–13, 2017.

[5.34] R. M. Sandner, W. Niedenzu, F. Piazza, and H. Ritsch, "Self-ordered stationary states of driven quantum degenerate gases in optical resonators," *EPL (Europhys. Lett.)*, vol. 111, p. 53001, sep 2015.

[5.35] Y. Chen, H. Zhai, and Z. Yu, "Superradiant phase transition of Fermi gases in a cavity across a feshbach resonance," *Phys. Rev. A*, vol. 91, p. 021602, Feb 2015.

[5.36] D. Kruse, C. von Cube, C. Zimmermann, and P. W. Courteille, "Observation of lasing mediated by collective atomic recoil," *Phys. Rev. Lett.*, vol. 91, p. 183601, Oct 2003.

[5.37] S. Slama, G. Krenz, S. Bux, C. Zimmermann, and P. W. Courteille, "Cavity-enhanced superradiant Rayleigh scattering with ultracold and Bose-Einstein condensed atoms," *Phys. Rev. A*, vol. 75, p. 063620, Jun 2007.

[5.38] S. Slama, S. Bux, G. Krenz, C. Zimmermann, and P. W. Courteille, "Superradiant Rayleigh scattering and collective atomic recoil lasing in a ring cavity," *Phys. Rev. Lett.*, vol. 98, p. 053603, Feb 2007.

[5.39] S. Bux, H. Tomczyk, D. Schmidt, P. W. Courteille, N. Piovella, and C. Zimmermann, "Control of matter-wave superradiance with a high-finesse ring cavity," *Phys. Rev. A*, vol. 87, p. 023607, Feb 2013.

[5.40] D. Schmidt, H. Tomczyk, S. Slama, and C. Zimmermann, "Dynamical instability of a Bose-Einstein condensate in an optical ring resonator," *Phys. Rev. Lett.*, vol. 112, p. 115302, Mar 2014.

[5.41] R. Culver, A. Lampis, B. Megyeri, K. Pahwa, L. Mudarikwa, M. Holynski, P. W. Courteille, and J. Goldwin, "Collective strong coupling of cold potassium atoms in a ring cavity," *New J. Phys.*, vol. 18, p. 113043, nov 2016.

[5.42] D. S. Naik, G. Kuyumjyan, D. Pandey, P. Bouyer, and A. Bertoldi, "Bose–Einstein condensate array in a malleable optical trap formed in a traveling wave cavity," *Quantum Science and Technology*, vol. 3, p. 045009, aug 2018.

[5.43] S. C. Schuster, P. Wolf, D. Schmidt, S. Slama, and C. Zimmermann, "Pinning transition of Bose-Einstein condensates in optical ring resonators," *Phys. Rev. Lett.*, vol. 121, p. 223601, Nov 2018.

[5.44] P. Wolf, S. C. Schuster, D. Schmidt, S. Slama, and C. Zimmermann, "Observation of subradiant atomic momentum states with Bose-Einstein condensates in a recoil resolving optical ring resonator," *Phys. Rev. Lett.*, vol. 121, p. 173602, Oct 2018.

[5.45] F. Mivehvar, H. Ritsch, and F. Piazza, "Cavity-Quantum-Electrodynamical Toolbox for Quantum Magnetism," *Phys. Rev. Lett.*, vol. 122, p. 113603, Mar 2019.

[5.46] D. F. Walls and G. J. Milburn, *Quantum Optics*. Berlin: Springer-Verlag, first ed., 1994.

[5.47] F. Mivehvar, S. Ostermann, F. Piazza, and H. Ritsch, "Driven-dissipative supersolid in a ring cavity," *Phys. Rev. Lett.*, vol. 120, p. 123601, Mar 2018.

[5.48] K. Baumann, C. Guerlin, F. Brennecke, and T. Esslinger, "Dicke quantum phase transition with a superfluid gas in an optical cavity," *Nature*, vol. 464, pp. 1301–1306, apr 2010.

[5.49] K. Baumann, R. Mottl, F. Brennecke, and T. Esslinger, "Exploring symmetry breaking at the dicke quantum phase transition," *Phys. Rev. Lett.*, vol. 107, p. 140402, Sep 2011.

[5.50] D. Yu, J.-S. Pan, X.-J. Liu, W. Zhang, and W. Yi, "Topological superradiant state in Fermi gases with cavity induced spin–orbit coupling," *Front. Phys.*, vol. 13, jul 2017.

[5.51] J.-S. Pan, X.-J. Liu, W. Zhang, W. Yi, and G.-C. Guo, "Topological superradiant states in a degenerate Fermi gas," *Phys. Rev. Lett.*, vol. 115, p. 045303, Jul 2015.

[5.52] P. Domokos, P. Horak, and H. Ritsch, "Semiclassical theory of cavity-assisted atom cooling," *J. Phys. B: At. Mol. Opt. Phys.*, vol. 34, no. 2, p. 187, 2001.

[5.53] C. Kittel and P. B. Kahn, "Quantum theory of solids," *Am. J. Phys.*, vol. 33, pp. 517–518, jun 1965.

[5.54] J. K. Asbóth, P. Domokos, H. Ritsch, and A. Vukics, "Self-organization of atoms in a cavity field: Threshold, bistability, and scaling laws," *Phys. Rev. A*, vol. 72, p. 053417, Nov 2005.

[5.55] W. Niedenzu, T. Grießer, and H. Ritsch, "Kinetic theory of cavity cooling and self-organisation of a cold gas," *EPL (Europhys. Lett.)*, vol. 96, p. 43001, nov 2011.

[5.56] "29 - on the theory of phase transitions," in *Collected Papers of L.D. Landau* (D. T. Haar, ed.), pp. 193 – 216, Pergamon, 1965.

[5.57] E. Fawcett, H. L. Alberts, V. Y. Galkin, D. R. Noakes, and J. V. Yakhmi, "Spin-density-wave antiferromagnetism in chromium alloys," *Rev. Mod. Phys.*, vol. 66, pp. 25–127, Jan 1994.

[5.58] E. Fawcett, "Spin-density-wave antiferromagnetism in chromium," *Rev. Mod. Phys.*, vol. 60, pp. 209–283, Jan 1988.

[5.59] A. W. Overhauser, "New mechanism of antiferromagnetism," *Phys. Rev. Lett.*, vol. 3, pp. 414–416, Nov 1959.

[5.60] M. Gangl and H. Ritsch, "Cold atoms in a high-Q ring cavity," *Phys. Rev. A*, vol. 61, p. 043405, Mar 2000.

[5.61] W. Niedenzu, R. M. Sandner, C. Genes, and H. Ritsch, "Quantum-correlated motion and heralded entanglement of distant optomechanically coupled objects," *J. Phys. B: At. Mol. Opt. Phys.*, vol. 45, p. 245501, nov 2012.

[5.62] A. Bergschneider, V. M. Klinkhamer, J. H. Becher, R. Klemt, L. Palm, G. Zürn, S. Jochim, and P. M. Preiss, "Correlations and entanglement in an itinerant quantum system," *arXiv preprint arXiv:1807.06405*, 2018.

[5.63] J. Bardeen, L. N. Cooper, and J. R. Schrieffer, "Microscopic theory of superconductivity," *Phys. Rev.*, vol. 106, pp. 162–164, apr 1957.

[5.64] J. Bardeen, L. N. Cooper, and J. R. Schrieffer, "Theory of superconductivity," *Phys. Rev.*, vol. 108, pp. 1175–1204, dec 1957.

[5.65] L. N. Cooper, "Bound electron pairs in a degenerate Fermi gas," *Phys. Rev.*, vol. 104, pp. 1189–1190, nov 1956.

[5.66] D. Fausti, R. I. Tobey, N. Dean, S. Kaiser, A. Dienst, M. C. Hoffmann, S. Pyon, T. Takayama, H. Takagi, and A. Cavalleri, "Light-induced superconductivity in a stripe-ordered cuprate," *Science*, vol. 331, pp. 189–191, jan 2011.

[5.67] J. Demsar, "Light-induced superconductivity," *Nat. Phys.*, vol. 12, pp. 202–203, mar 2016.

[5.68] M. Mitrano, A. Cantaluppi, D. Nicoletti, S. Kaiser, A. Perucchi, S. Lupi, P. D. Pietro, D. Pontiroli, M. Riccò, S. R. Clark, D. Jaksch, and A. Cavalleri, "Possible light-induced superconductivity in k3c60 at high temperature," *Nature*, vol. 530, pp. 461–464, feb 2016.

References for Chapter 6

[6.1] N. Goldman, G. Juzeliūnas, P. Öhberg, and I. B. Spielman, "Light-induced gauge fields for ultracold atoms," *Rep. Prog. Phys.*, vol. 77, p. 126401, dec 2014.

[6.2] J. Dalibard, F. Gerbier, G. Juzeliūnas, and P. Öhberg, "Colloquium: Artificial gauge potentials for neutral atoms," *Rev. Mod. Phys.*, vol. 83, pp. 1523–1543, Nov 2011.

[6.3] P. Engels, I. Coddington, P. C. Haljan, V. Schweikhard, and E. A. Cornell, "Observation of long-lived vortex aggregates in rapidly rotating Bose-Einstein condensates," *Phys. Rev. Lett.*, vol. 90, p. 170405, May 2003.

[6.4] V. Schweikhard, I. Coddington, P. Engels, V. P. Mogendorff, and E. A. Cornell, "Rapidly rotating Bose-Einstein condensates in and near the lowest Landau level," *Phys. Rev. Lett*, vol. 92, no. 4, p. 040404, 2004.

[6.5] Y.-J. Lin, R. L. Compton, A. R. Perry, W. D. Phillips, J. V. Porto, and I. B. Spielman, "Bose-Einstein condensate in a uniform light-induced vector potential," *Phys. Rev. Lett.*, vol. 102, p. 130401, Mar 2009.

[6.6] Y.-A. Chen, S. Nascimbène, M. Aidelsburger, M. Atala, S. Trotzky, and I. Bloch, "Controlling correlated tunneling and superexchange interactions with AC-driven optical lattices," *Phys. Rev. Lett.*, vol. 107, p. 210405, Nov 2011.

[6.7] P. Hauke, O. Tieleman, A. Celi, C. Ölschläger, J. Simonet, J. Struck, M. Weinberg, P. Windpassinger, K. Sengstock, M. Lewenstein, and A. Eckardt, "Non-abelian gauge fields and topological insulators in shaken optical lattices," *Phys. Rev. Lett.*, vol. 109, p. 145301, Oct 2012.

[6.8] N. Goldman and J. Dalibard, "Periodically driven quantum systems: Effective Hamiltonians and engineered gauge fields," *Phys. Rev. X*, vol. 4, p. 031027, Aug 2014.

[6.9] Y. Aharonov and D. Bohm, "Significance of electromagnetic potentials in the quantum theory," *Phys. Rev.*, vol. 115, pp. 485–491, Aug 1959.

[6.10] P. G. Harper, "Single band motion of conduction electrons in a uniform magnetic field," *Proc. Phys. Soc. A*, vol. 68, pp. 874–878, Oct. 1955.

[6.11] D. R. Hofstadter, "Energy levels and wave functions of Bloch electrons in rational and irrational magnetic fields," *Phys. Rev. B*, vol. 14, pp. 2239–2249, Sep 1976.

[6.12] D. Jaksch and P. Zoller, "Creation of effective magnetic fields in optical lattices: the Hofstadter butterfly for cold neutral atoms," *New J. Phys.*, vol. 5, pp. 56–56, May 2003.

[6.13] K. Osterloh, M. Baig, L. Santos, P. Zoller, and M. Lewenstein, "Cold atoms in non-abelian gauge potentials: From the Hofstadter "moth" to lattice gauge theory," *Phys. Rev. Lett.*, vol. 95, p. 010403, Jun 2005.

[6.14] M. Aidelsburger, M. Atala, M. Lohse, J. T. Barreiro, B. Paredes, and I. Bloch, "Realization of the Hofstadter hamiltonian with ultracold atoms in optical lattices," *Phys. Rev. Lett.*, vol. 111, p. 185301, Oct 2013.

[6.15] G. Jotzu, M. Messer, R. Desbuquois, M. Lebrat, T. Uehlinger, D. Greif, and T. Esslinger, "Experimental realization of the topological haldane model with ultracold fermions," *Nature*, vol. 515, pp. 237–240, Nov. 2014.

[6.16] N. Goldman, J. C. Budich, and P. Zoller, "Topological quantum matter with ultracold gases in optical lattices," *Nat. Phys.*, vol. 12, pp. 639–645, Jul 2016.

[6.17] D.-W. Zhang, Y.-Q. Zhu, Y. X. Zhao, H. Yan, and S.-L. Zhu, "Topological quantum matter with cold atoms," *Adv. Phys.*, vol. 67, no. 4, pp. 253–402, 2018.

[6.18] N. R. Cooper, J. Dalibard, and I. B. Spielman, "Topological bands for ultracold atoms," *Rev. Mod. Phys.*, vol. 91, p. 015005, Mar 2019.

[6.19] M. Aidelsburger, M. Lohse, C. Schweizer, M. Atala, J. T. Barreiro, S. Nascimbène, N. R. Cooper, I. Bloch, and N. Goldman, "Measuring the Chern number of Hofstadter bands with ultracold bosonic atoms," *Nat. Phys.*, vol. 11, pp. 162–166, Dec. 2014.

[6.20] M. Atala, M. Aidelsburger, M. Lohse, J. T. Barreiro, B. Paredes, and I. Bloch, "Observation of chiral currents with ultracold atoms in bosonic ladders," vol. 10, pp. 588–593, July 2014.

[6.21] O. Boada, A. Celi, J. I. Latorre, and M. Lewenstein, "Quantum simulation of an extra dimension," *Phys. Rev. Lett.*, vol. 108, p. 133001, Mar 2012.

[6.22] A. Celi, P. Massignan, J. Ruseckas, N. Goldman, I. B. Spielman, G. Juzeliūnas, and M. Lewenstein, "Synthetic gauge fields in synthetic dimensions," *Phys. Rev. Lett.*, vol. 112, p. 043001, Jan 2014.

[6.23] H. M. Price, O. Zilberberg, T. Ozawa, I. Carusotto, and N. Goldman, "Four-dimensional quantum Hall effect with ultracold atoms," *Phys. Rev. Lett.*, vol. 115, p. 195303, Nov 2015.

[6.24] U.-J. Wiese, "Ultracold quantum gases and lattice systems: quantum simulation of lattice gauge theories," *Ann. Phys.*, vol. 525, pp. 777–796, July 2013.

[6.25] M. J. Edmonds, M. Valiente, G. Juzeliūnas, L. Santos, and P. Öhberg, "Simulating an interacting gauge theory with ultracold bose gases," *Phys. Rev. Lett.*, vol. 110, p. 085301, Feb 2013.

[6.26] T. Keilmann, S. Lanzmich, I. McCulloch, and M. Roncaglia, "Statistically induced phase transitions and anyons in 1d optical lattices," *Nat. Commun.*, vol. 2, p. 361, 2011.

[6.27] L. W. Clark, B. M. Anderson, L. Feng, A. Gaj, K. Levin, and C. Chin, "Observation of density-dependent gauge fields in a Bose-Einstein condensate based on micromotion control in a shaken two-dimensional lattice," *Phys. Rev. Lett.*, vol. 121, p. 030402, Jul 2018.

[6.28] F. Görg, K. Sandholzer, J. Minguzzi, R. Desbuquois, M. Messer, and T. Esslinger, "Realization of density-dependent Peierls phases to engineer quantized gauge fields coupled to ultracold matter," *Nat. Phys.*, vol. 15, pp. 1161–1167, Nov 2019.

[6.29] L. Barbiero, C. Schweizer, M. Aidelsburger, E. Demler, N. Goldman, and F. Grusdt, "Coupling ultracold matter to dynamical gauge fields in optical lattices: From flux attachment to $\mathbb{Z}_2$ lattice gauge theories," *Science Advances*, vol. 5, no. 10, p. eaav7444, 2019.

[6.30] C. Schweizer, F. Grusdt, M. Berngruber, L. Barbiero, E. Demler, N. Goldman, I. Bloch, and M. Aidelsburger, "Floquet approach to $\mathbb{Z}2$ lattice gauge theories with ultracold atoms in optical lattices," *Nat. Phys.*, vol. 15, pp. 1168–1173, Sept. 2019.

[6.31] R. Lauter, C. Brendel, S. J. M. Habraken, and F. Marquardt, "Pattern phase diagram for two-dimensional arrays of coupled limit-cycle oscillators," *Phys. Rev. E*, vol. 92, p. 012902, Jul 2015.

[6.32] S. Walter and F. Marquardt, "Classical dynamical gauge fields in optomechanics," *New J. Phys.*, vol. 18, no. 11, p. 113029, 2016.

[6.33] H. Ritsch, P. Domokos, F. Brennecke, and T. Esslinger, "Cold atoms in cavity-generated dynamical optical potentials," *Rev. Mod. Phys.*, vol. 85, pp. 553–601, Apr 2013.

[6.34] K. Roux, H. Konishi, V. Helson, and J.-P. Brantut, "Strongly correlated fermions strongly coupled to light," June 2020.

[6.35] R. M. Kroeze, Y. Guo, V. D. Vaidya, J. Keeling, and B. L. Lev, "Spinor self-ordering of a quantum gas in a cavity," *Phys. Rev. Lett.*, vol. 121, p. 163601, Oct 2018.

[6.36] Y. Guo, R. M. Kroeze, V. D. Vaidya, J. Keeling, and B. L. Lev, "Sign-changing photon-mediated atom interactions in multimode cavity quantum electrodynamics," *Phys. Rev. Lett.*, vol. 122, p. 193601, May 2019.

[6.37] R. M. Kroeze, Y. Guo, and B. L. Lev, "Dynamical spin-orbit coupling of a quantum gas," *Phys. Rev. Lett.*, vol. 123, p. 160404, Oct 2019.

[6.38] F. Mivehvar, H. Ritsch, and F. Piazza, "Cavity-quantum-electrodynamical toolbox for quantum magnetism," *Phys. Rev. Lett.*, vol. 122, p. 113603, Mar 2019.

[6.39] F. Mivehvar and D. L. Feder, "Synthetic spin-orbit interactions and magnetic fields in ring-cavity QED," *Phys. Rev. A*, vol. 89, p. 013803, Jan 2014.

[6.40] L. Dong, L. Zhou, B. Wu, B. Ramachandhran, and H. Pu, "Cavity-assisted dynamical spin-orbit coupling in cold atoms," *Phys. Rev. A*, vol. 89, p. 011602, Jan 2014.

[6.41] Y. Deng, J. Cheng, H. Jing, and S. Yi, "Bose-Einstein condensates with cavity-mediated spin-orbit coupling," *Phys. Rev. Lett.*, vol. 112, p. 143007, Apr 2014.

[6.42] F. Mivehvar and D. L. Feder, "Enhanced stripe phases in spin-orbit-coupled Bose-Einstein condensates in ring cavities," *Phys. Rev. A*, vol. 92, p. 023611, Aug 2015.

[6.43] K. E. Ballantine, B. L. Lev, and J. Keeling, "Meissner-like effect for a synthetic gauge field in multimode cavity QED," *Phys. Rev. Lett.*, vol. 118, p. 045302, Jan 2017.

[6.44] W. Zheng and N. R. Cooper, "Superradiance induced particle flow via dynamical gauge coupling," *Phys. Rev. Lett.*, vol. 117, p. 175302, Oct 2016.

[6.45] C.-M. Halati, A. Sheikhan, and C. Kollath, "Cavity-induced artificial gauge field in a Bose-Hubbard ladder," *Phys. Rev. A*, vol. 96, p. 063621, Dec 2017.

[6.46] A. Sheikhan, F. Brennecke, and C. Kollath, "Cavity-induced generation of non-trivial topological states in a two-dimensional Fermi gsa," *Phys. Rev. A*, vol. 94, p. 061603, Dec 2016.

[6.47] C.-M. Halati, A. Sheikhan, and C. Kollath, "Cavity-induced spin-orbit coupling in an interacting bosonic wire," *Phys. Rev. A*, vol. 99, p. 033604, Mar 2019.

[6.48] I. Carusotto and C. Ciuti, "Quantum fluids of light," *Rev. Mod. Phys.*, vol. 85, pp. 299–366, Feb 2013.

[6.49] J. Keeling, M. Bhaseen, and B. Simons, "Fermionic superradiance in a transversely pumped optical cavity," *Phys. Rev. Lett*, vol. 112, no. 14, p. 143002, 2014.

[6.50] A. Larkin and S. Pikin, "Phase transitions of the first order but nearly of the second," *Sov Phys JETP*, vol. 29, pp. 891–896, 1969.

[6.51] F. Mivehvar, H. Ritsch, and F. Piazza, "Emergent quasicrystalline symmetry in light-induced quantum phase transitions," *Phys. Rev. Lett.*, vol. 123, p. 210604, Nov 2019.

[6.52] D. Holzmann, M. Sonnleitner, and H. Ritsch, "Synthesizing variable particle interaction potentials via spectrally shaped spatially coherent illumination," *New J. Phys.*, vol. 20, no. 10, p. 103009, 2018.

References for Chapter 7

[7.1] H. Ritsch, P. Domokos, F. Brennecke, and T. Esslinger, "Cold atoms in cavity-generated dynamical optical potentials," *Rev. Mod. Phys.*, vol. 85, pp. 553–601, Apr 2013.

[7.2] F. Mivehvar, F. Piazza, T. Donner, and H. Ritsch, "Cavity QED with quantum gases: new paradigms in many-body physics," *Ad. Phys.*, vol. 70, no. 1, pp. 1–153, 2021.

[7.3] C. Kollath, A. Sheikhan, S. Wolff, and F. Brennecke, "Ultracold Fermions in a Cavity-Induced Artificial Magnetic Field," *Phys. Rev. Lett.*, vol. 116, p. 060401, Feb 2016.

[7.4] E. Colella, F. Mivehvar, F. Piazza, and H. Ritsch, "Hofstadter butterfly in a cavity-induced dynamic synthetic magnetic field," *Phys. Rev. B*, vol. 100, p. 224306, Dec 2019.

[7.5] W. Zheng and N. R. Cooper, "Superradiance induced particle flow via dynamical gauge coupling," *Phys. Rev. Lett.*, vol. 117, p. 175302, Oct 2016.

[7.6] K. E. Ballantine, B. L. Lev, and J. Keeling, "Meissner-like effect for a synthetic gauge field in multimode cavity QED," *Phys. Rev. Lett.*, vol. 118, p. 045302, Jan 2017.

[7.7] F. Mivehvar and D. L. Feder, "Synthetic spin-orbit interactions and magnetic fields in ring-cavity QED," *Phys. Rev. A*, vol. 89, p. 013803, Jan 2014.

[7.8] L. Dong, L. Zhou, B. Wu, B. Ramachandhran, and H. Pu, "Cavity-assisted dynamical spin-orbit coupling in cold atoms," *Phys. Rev. A*, vol. 89, p. 011602, Jan 2014.

[7.9] Y. Deng, J. Cheng, H. Jing, and S. Yi, "Bose-Einstein condensates with cavity-mediated spin-orbit coupling," *Phys. Rev. Lett.*, vol. 112, p. 143007, Apr 2014.

[7.10] F. Mivehvar and D. L. Feder, "Enhanced stripe phases in spin-orbit-coupled Bose-Einstein condensates in ring cavities," *Phys. Rev. A*, vol. 92, p. 023611, Aug 2015.

[7.11] S. Ostermann, H.-W. Lau, H. Ritsch, and F. Mivehvar, "Cavity-induced emergent topological spin textures in a Bose–Einstein condensate," *New J. Phys.*, vol. 21, p. 013029, Jan 2019.

[7.12] F. Mivehvar, H. Ritsch, and F. Piazza, "Cavity-Quantum-Electrodynamical Toolbox for Quantum Magnetism," *Phys. Rev. Lett.*, vol. 122, p. 113603, Mar 2019.

[7.13] C.-M. Halati, A. Sheikhan, and C. Kollath, "Cavity-induced spin-orbit coupling in an interacting bosonic wire," *Phys. Rev. A*, vol. 99, p. 033604, Mar 2019.

[7.14] S. Ostermann, H. Ritsch, and F. Mivehvar, "Many-body phases of a planar Bose-Einstein condensate with cavity-induced spin-orbit coupling," *Phys. Rev. A*, vol. 103, p. 023302, Feb 2021.

[7.15] R. M. Kroeze, Y. Guo, and B. L. Lev, "Dynamical spin-orbit coupling of a quantum gas," *Phys. Rev. Lett.*, vol. 123, p. 160404, Oct 2019.

[7.16] V. Lienhard, P. Scholl, S. Weber, D. Barredo, S. de Léséleuc, R. Bai, N. Lang, M. Fleischhauer, H. P. Büchler, T. Lahaye, and A. Browaeys, "Realization of a density-dependent peierls phase in a synthetic, spin-orbit coupled rydberg system," *Phys. Rev. X*, vol. 10, p. 021031, May 2020.

[7.17] A. Morales, D. Dreon, X. Li, A. Baumgärtner, P. Zupancic, T. Donner, and T. Esslinger, "Two-mode Dicke model from nondegenerate polarization modes," *Phys. Rev. A*, vol. 100, p. 013816, Jul 2019.

[7.18] E. Orignac and T. Giamarchi, "Meissner effect in a bosonic ladder," *Phys. Rev. B*, vol. 64, p. 144515, Sep 2001.

[7.19] D. Jaksch and P. Zoller, "Creation of effective magnetic fields in optical lattices: the Hofstadter butterfly for cold neutral atoms," *New J. Phys.*, vol. 5, pp. 56–56, May 2003.

[7.20] "See Supplementary Material for further details.,"

[7.21] A. Celi, P. Massignan, J. Ruseckas, N. Goldman, I. B. Spielman, G. Juzeliūnas, and M. Lewenstein, "Synthetic gauge fields in synthetic dimensions," *Phys. Rev. Lett.*, vol. 112, p. 043001, Jan 2014.

[7.22] R. Peierls, "Zur theorie des diamagnetismus von leitungselektronen," *Z. Phys.*, vol. 80, pp. 763–791, Nov. 1933.

[7.23] Y. Aharonov and D. Bohm, "Significance of electromagnetic potentials in the quantum theory," *Phys. Rev.*, vol. 115, pp. 485–491, Aug 1959.

[7.24] F. Piazza, P. Strack, and W. Zwerger, "Bose–Einstein condensation versus Dicke–Hepp–Lieb transition in an optical cavity," *Ann. Phys.*, vol. 339, pp. 135 – 159, 2013.

[7.25] R. Wei and E. J. Mueller, "Theory of bosons in two-leg ladders with large magnetic fields," *Phys. Rev. A*, vol. 89, p. 063617, Jun 2014.

[7.26] S. Uchino and A. Tokuno, "Population-imbalance instability in a Bose-Hubbard ladder in the presence of a magnetic flux," *Phys. Rev. A*, vol. 92, p. 013625, Jul 2015.

[7.27] S. Greschner, M. Piraud, F. Heidrich-Meisner, I. P. McCulloch, U. Schollwöck, and T. Vekua, "Symmetry-broken states in a system of interacting bosons on a two-leg ladder with a uniform abelian gauge field," *Phys. Rev. A*, vol. 94, p. 063628, Dec 2016.

[7.28] K. Sacha and J. Zakrzewski, "Time crystals: a review," *Reports on Progress in Physics*, vol. 81, p. 016401, Nov. 2017.

[7.29] H. Keßler, J. G. Cosme, M. Hemmerling, L. Mathey, and A. Hemmerich, "Emergent limit cycles and time crystal dynamics in an atom-cavity system," *Phys. Rev. A*, vol. 99, p. 053605, May 2019.

[7.30] H. Keßler, P. Kongkhambut, C. Georges, L. Mathey, J. G. Cosme, and A. Hemmerich, "Observation of a dissipative time crystal," *Phys. Rev. Lett.*, vol. 127, p. 043602, Jul 2021.

[7.31] F. Piazza and H. Ritsch, "Self-ordered limit cycles, chaos, and phase slippage with a superfluid inside an optical resonator," *Phys. Rev. Lett.*, vol. 115, p. 163601, Oct 2015.

[7.32] J. Maxwell, *A treatise on electricity and magnetism*. New York: Dover Publications, 1954.

[7.33] T. Elsässer, B. Nagorny, and A. Hemmerich, "Optical bistability and collective behavior of atoms trapped in a high-Q ring cavity," *Phys. Rev. A*, vol. 69, p. 033403, Mar 2004.

[7.34] C.-M. Halati, A. Sheikhan, and C. Kollath, "Cavity-induced artificial gauge field in a Bose-Hubbard ladder," *Phys. Rev. A*, vol. 96, p. 063621, Dec 2017.

List of Publications

Publications from master Thesis

- Colella, E., Citro, R., Barsanti, M., Rossini, D., and Chiofalo, M. L. (2018). Quantum phases of spinful Fermi gases in optical cavities. Physical Review B, 97(13), 134502.
- Colella, E., Chiofalo, M. L., Barsanti, M., Rossini, D., and Citro, R. (2019). Fluid structure of 1D spinful Fermi gases with long-range interactions. Journal of Physics B: Atomic, Molecular and Optical Physics, 52(21), 215301.

Publications from Phd Thesis

- Colella, E., Ostermann, S., Niedenzu, W., Mivehvar, F., and Ritsch, H. (2019). Antiferromagnetic self-ordering of a Fermi gas in a ring cavity. New Journal of Physics, 21(4), 043019.
- Colella, E., Mivehvar, F., Piazza, F., and Ritsch, H. (2019). Hofstadter butterfly in a cavity-induced dynamic synthetic magnetic field. Physical Review B, 100(22), 224306.
- Colella, E., Mivehvar, F., and Ritsch, H. (2021). Open Quantum-System Simulation of Faraday's Induction Law via Dynamical Instabilities. arXiv preprint arXiv:2103.01979.